ABSTRACT

Title of dissertation: MODELING BUOYANCY-DRIVEN INSTABILITY AND TRANSPORT IN POROUS MEDIA WITH APPLICATION TO GEOLOGICAL CARBON DIOXIDE STORAGE

Zohreh Ghorbani, Doctor of Philosophy, 2017

Dissertation directed by: Dr. Amir Riaz
Department of Mechanical Engineering

Buoyancy-driven convection in porous media plays a central role in a wide range of industrial and environmental settings [72] and has received renewed attention recently because of the role of convection in geologic carbon dioxide (CO_2) sequestration– a viable solution to mitigate climate change by reducing the concentration of atmospheric CO_2. The idea is to inject CO_2 into brine saturated formations, whereby a gradual dissolution of CO_2 into the underlying brine forms a mixture that is denser than either fluids. The unstable stratified flow eventually results in a Rayleigh–Bénard type flow, in which the formation of sinking plumes acts to mix the CO_2 more thoroughly into the aquifer and increases the security of storage. Consequently, accurate prediction and characterization of the mixing process is crucial in estimating and managing storage security against leakage risks. Computational modeling of CO_2 storage in subsurface formations, however, is a complex multiscale transport process because of several competing flow paths, regimes, and

displacement patterns accompanied by a series of geochemical reactions, across a hierarchy of length and time scales associated with multiphase flow in porous formations. This has motivated studies of simplified system where although various features of real formations are neglected, it provides a valuable framework to investigate the underlying key processes in detail. To this end, the present work aims to improve the understanding of buoyancy-driven convection in an idealized 2D porous layer by addressing two fundamental issues that have not been investigated in the past using multiple theoretical and high resolution numerical simulation: (i) convective mixing in a vertically-layered porous media; and (ii) convective mixing in a continuously perturbed porous media. We uncover new physics, both in the dynamics of convective flow in a layered porous media as well as natural convection in a system subjected to continuous forcing. These contributions can be used as a stepping stone for modeling geological scale systems.

Among the main contributions of this study is the finding that, when the porous medium is vertically-layered, thick permeability layers enhance instability compared to thin layers when heterogeneity is increased. In contrast, for thin layers the instability is weakened progressively with increasing heterogeneity to the extent that the corresponding homogeneous case, with the same density contrast, is more unstable. A resonant amplification of instability is observed within the linear regime when the dominant perturbation mode is equal to half the wavenumber of permeability variation. A weaker resonance also occurs when the dominant perturbation mode of the heterogeneous system coincides with the corresponding homogeneous system. On the other hand, substantial damping occurs when the

perturbation mode is equal to the harmonic and sub-harmonic components of the permeability wavenumber. The phenomenon of such harmonic interactions influences both the onset of instability as well as the onset of convection. Of particular physical importance is a multimodal horizontal perturbation structures, in contrast to the situation for vertical permeability variation. As a consequence, the standard eigenvalue analysis can not be used.

In the case of a continuously perturbed porous system, perturbations that are required to induce convection are introduced in the form a spatial variation of porosity in the system, a feature reflecting realistic geological settings. This form of perturbation results in an unconditionally unstable system for which the prescription of initial perturbation time and shape function are not needed. This is in contrast to a system which is perturbed in the conventional manner by introducing disturbances in the initial concentration. Using a reduced nonlinear method, the effect of harmonic variations of porosity in the transverse and streamwise direction on the onset time of convection and late time behavior is examined. It was found that the choice of perturbation method has a noticeable effect on the onset of convection and the subsequent nonlinear regime, in that the onset time of convection is reached more quickly in an impulsively perturbed system. Subsequently, an optimization procedure based on a Lagrange multiplier technique are utilized to find the optimal porosity structure that leads to the earliest onset time of convection. Scaling relationships for the optimal onset of convection and wavenumber are developed in terms of aquifer properties and initial perturbation magnitude.

MODELING BUOYANCY-DRIVEN INSTABILITY AND TRANSPORT IN POROUS MEDIA WITH APPLICATION TO GEOLOGICAL CARBON DIOXIDE STORAGE

by

Zohreh Ghorbani

Dissertation submitted to the Faculty of the Graduate School of the
University of Maryland, College Park in partial fulfillment
of the requirements for the degree of
Doctor of Philosophy
2017

Advisory Committee:
Associate Professor Amir Riaz, Chair
Professor James Duncan
Professor Kenneth Kiger
Professor Jelena Srebric
Professor Bao Yang
Professor James Baeder, Dean's Representative

Dedication

To my niece, Hana, you will always be in my heart, even if you are just a memory of what should have been.

Acknowledgments

This work is the fruit of many sleepless nights, accompanied by sweat and tears of both joy and frustration in the past 3 years. First and for most, I would like to thank those close to my heart who have cheered and willed me along this journey: my parents for always putting my needs and happiness before their own and for their unwavering support throughout all these years (this time apart has not been in vain); my sisters, Azadeh and Roya, for their endless love and the joy that they bring into my life; my late grandmother, Sareh, who by lifelong example taught me perseverance, integrity and truthfulness– I wish you were here to see that I finally accomplished this goal and embarked in the next steps of my life; Bill and Bonnie Berry for being generous, kind and loving, for opening their home and hearts treating me as one of their own and being a source of stability and comfort during turbulent times; Ben for being by my side through highs and lows during all these years, for reminding me to keep things in perspective, for his continuous encouragement and relentless belief in me when this felt like a sisyphean job, and for helping me with my defense presentation practice. I am so fortunate to have you in my life and I could not have done it without you.

I would like to thank my adviser, Dr. Amir Riaz, for giving me a platform to work independently in the past 3 years. I would also like to thank the other members of my dissertation committee, Dr. James Baeder, Dr. James Duncan, Dr. Kenneth Kiger, Dr. Jelena Srebric and Dr. Bao Yang for accepting to serve on my doctoral committee and providing useful feedback. I am also thankful to Professor Hugh

Bruck for his continuous support of offering me a teaching assistant position during my tenure in Mechanical engineering department. I would also like to extend my gratitude to all friends and colleagues for making this Ph.D. more than an academic experience.

Table of Contents

List of Tables

List of Figures

Nomenclature

Greek Symbols

α_L longitudinal dispersivity

α_T transverse dispersivity

δ boundary layer depth

ϵ perturbation amplitude

μ viscosity

ϕ porosity

Φ amplification

Φ^* dominant amplification

ρ solution density

$\Delta\rho$ density difference

ρ_0 brine density

ρ_1 density of CO_2 saturated brine

σ growth rate

σ^* dominant growth rate obtained by IVP

$\sigma_{\max}$ dominant growth rate in physical space obtained by EVP

σ_ξ dominant growth rate in self-similar space

ξ similarity variable

$\tilde{\psi}$ perturbation streamfunction

$\hat{\psi}$ streamfunction eigenfunction

ψ streamfunction

Ω, Ω_c, Ω_p vorticity with its two component sources

Roman Symbols

$\mathcal{A}$, $\mathcal{B}$ spatial derivative matrix of EVP

$\mathscr{A}$, $\mathscr{B}$ Linear flow operator in physical and self-similar space

a_p permeability amplitude

c dissolved CO_2 concentration in brine

$\tilde{c}$ concentration perturbation

c_e concentration eigenfunction

c_p initial condition profile

D molecular diffusion

$\mathcal{D}$ dispersivity

E_l perturbation magnitude of the horizontal Fourier mode

$\mathcal{F}$, $\mathcal{G}$ horizontal and vertical shape function

g gravitational acceleration

H domain depth

$\mathcal{J}$ dissolution flux

$\bar{\mathcal{K}}$ average permeability

$\mathcal{K}$ dimensionless permeability

k_ϕ^* dominant mode based on amplification

k_σ^* dominant mode based on growth rate

k_c perturbation wavenumber

k_p permeability wavenumber

k_{res} resonance wavenumber

L domain width

l horizontal Fourier mode

m_l, n_l Fourier cosine and sine coefficients

p pressure

$\widetilde{p}$ perturbation pressure

Pe Peclet number

Ra Rayleigh number

t time

t_c critical time for onset of instability

t_f final time

t_p perturbation time

t_{cv} onset time of convection

t^*_{cv} critical onset time of convection

U buoyancy velocity

u velocity component in the transverse direction

$\mathbf{u}(u, w)$ Darcy velocity

$\tilde{u}$ perturbation velocity in the streamline direction

$\widetilde{\mathbf{u}}$ perturbation velocity

w velocity component in the streamline direction

x horizontal coordinate

$\mathbf{x}$ position vector

z vertical coordinate

$\hat{\mathbf{z}}$ unit normal in the vertical direction

Subscript

b base-state

$p = [\Omega_c, \Omega_p, \Omega, \mathcal{E}]$ field variable used for measuring the perturbation magnitude

Chapter 1: Introduction

Buoyancy-driven convection plays a central role in a wide range of industrial and environmental settings, from oceanic and atmospheric circulations to chemical systems, to name a few. In general, the natural convection induced by the fluid density difference triggers instability where the disturbances grow and eventually lead to a complex behavior. This process in turn leads to a significant increase in transport of mass, heat, and energy. During the past few decades, extensive studies have been performed to understand the fundamental aspects of instability of buoyancy-driven flows using theoretical, numerical and experimental techniques. The present thesis focuses on density-driven convection in porous media.

1.1 Motivation

Convection in porous media is a well-established process encountered in numerous engineering applications, such as solute transport in groundwater flows [79, 90, 94], oil and gas extraction [14, 64, 102], and geothermal energy extraction [72, 78]. Convection in porous medium has been the subject of numerous studies since the pioneering work of Horton & Rogers [49] and have received renewed attention because of the role of convection in geologic carbon dioxide (CO_2) sequestration.

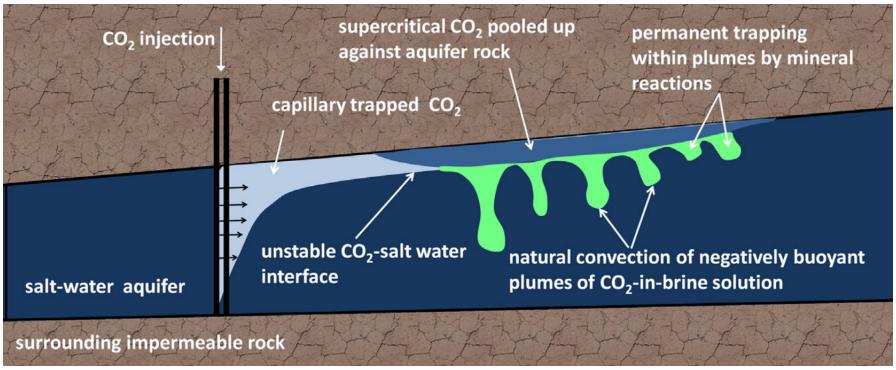

Figure 1.1: Schematic illustration of a typical sequestration process [85].

Emissions of carbon dioxide (CO_2), produced by industrial process, is a major contributor to climate change, a phenomenon that is widely considered one of the greatest global threats to the economic and political stability of the world community [58]. It is widely recognized, however, that the implementation of a low-carbon energy infrastructure will take tens to hundreds of years at global scales [12]. Geologic CO_2 storage, which entails injection of supercritical CO_2 into brine-saturated formations at depths between 800 and 3000 m, has emerges as a promising short-term solution to mitigate climate change by reducing atmospheric CO_2 emission into the atmosphere [3, 10, 57, 67, 74, 75]. This process is known as carbon capture and storage (CCS) which involves the safe and effective capture, transport, injection, and ultimate storage of CO_2 in geological formations [2, 67, 104]. There is, however, uncertainty about the long-term fate of CO_2 [4, 36, 62].

The sequestration of CO_2 is a gradual process that is controlled by a number of different trapping mechanisms: structural trapping, residual trapping, solubility trapping, and mineral trapping, as shown in Fig. 1.1. These mechanisms occur over a wide range of time scales ranging from days to hundreds of years depending on the

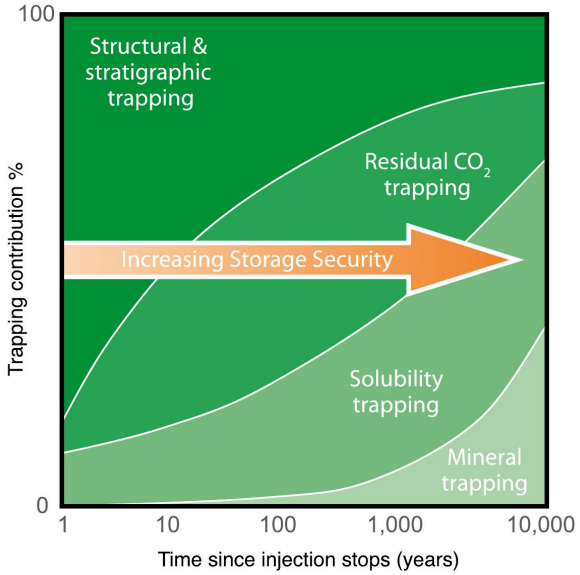

Figure 1.2: Schematic representation of the change of trapping mechanisms and increasing CO_2 storage security over time [67].

quality of the aquifer, i.e. absent of fractures and fissures, and the immobilization rate of CO_2 [85]. The contribution of each trapping mechanism also changes over time [104]. While the storage security increases from structural and residual trapping to mineral trapping, the relative time of the trapping mechanisms within which each process occurs increases by a few order of magnitude in years as shown in in Fig. 1.2 [67, 104].

When supercritical [1] CO_2 is injected into a brine-saturated aquifer, the lighter CO_2 rises upward due to buoyancy until reaching the impermeable cap rock, beneath which it spreads horizontally above the heavier brine, as shown in Fig. 1.3(a). This is referred to as physical trapping, where eventually a significant fraction of injected CO_2 will be confined under the cap rock over several decades following the injection period [35] as a result of upward migration. Over time, the supercritical

[1] Supercritical refers to the state of CO_2 at temperature and pressure above the critical point in a phase diagram. At this point, CO_2 behaves with gas-like viscosity and liquid-like density.

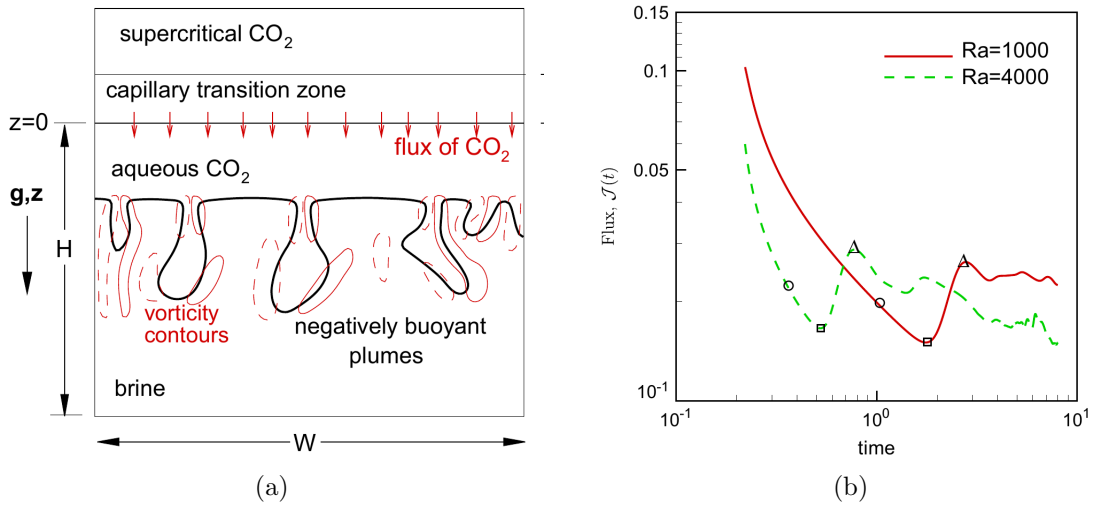

Figure 1.3: (a) Schematic of a typical 2D system used for modelling of convective mixing, (b) Evolution of the dissolution flux of CO_2 in an idealized system for low and high Rayleigh number of 1000 and 4000. Critical time, t_c, is indicated on the curves by circles, the onset of convection by square symbols and the nonlinear saturation onset time by triangles [85].

CO_2 gradually dissolves into the brine across the two-phase interface, at rates that are controlled by molecular diffusion, forming a mixture that is denser than the underlying brine [35]. The resulting stratification naturally triggers a Rayleigh-Bénard type gravitationally instability, often referred as convective mixing, that further develops into formation of finger-like sinking plume [27, 62, 86, 110]. While the objective of CO_2 sequestration is to obtain maximum trapping rate in a short amount of time, the longer time scales associated with the trapping mechanism create a risk of CO_2 leakage to fresh water and the atmosphere [4, 36, 85]. The process of convective mixing enhances the rate of CO_2 dissolution and subsequently reduces the long-term risk of CO_2 leakage [63, 70, 98].

The dynamic of the convective mixing can be characterized by analyzing the dissolution flux. The flux is an indication of how much CO_2 dissolves into the

system through the buoyant plume and it is defined as the time rate of change of CO_2 across the interface. The time history of flux shows various stages of plume migration: the onset of instability, the onset of convection, the nonlinear saturation, and the late-time behavior of the dissolution flux.

The evolution of flux for a general isotropic homogeneous system is shown in figure 1.3(b). Initially, CO_2 diffuses into brine and forms a diffusive boundary layer that grows in proportion to the diffusive time scale where all perturbations are damped by the stabilizing effect of diffusion. At a critical time, which is called the onset of instability t_c, the disturbances start to grow and the perturbation growth rate becomes positive. The continuous growth of disturbances eventually results in a positive growth rate of flux; this time corresponds to the onset of convection or onset of nonlinear instability. At this time, the finger-like structures become noticeable. The convective fingers begin to transport the CO_2-rich brine away from the interface leading to a sudden increase in the dissolution flux. The dissolution flux quickly increases and attains a maximum value. This time corresponds to the onset of nonlinear saturation. After this point, the merging of convective fingers begins and the nonlinear interactions between the fingers and their neighbouring fingers give rise to large-scale structures over which a second onset of bifurcation occurs. Eventually the buoyant plume interacts with the bottom boundary leading to saturation of the entire domain. Therefore, exploring the time scales associated with the safe storage of CO_2 in brine-saturated aquifers is a necessary step to improve fundamental understanding of the associated physical mechanism. This work focuses on solubility trapping because it plays a key role in enhancing dissolution of CO_2

into the aquifer brine and hence increases the overall storage security.

1.2 Challenges and Review

Convection in porous media, which dates back to the pioneering work of Horton & Rogers [49] and Lapwood [59], has been studied extensively to characterize the underlying dynamics of this process in various contexts [24, 52, 72, 85]. Numerous studies have focused on predicting the onset of instability and convection, and the related unstable wavelength [11, 27, 43, 53, 81, 83, 86, 95, 96, 112], nonlinear two-dimensional simulations [39, 44, 45, 86, 109] and three-dimensional simulations [34, 46, 76], and bench scale experimental systems [5, 56, 70, 96, 108]. Most of these studies considered an idealized system where, depending on the focus of their study, numerous features of natural formations were neglected. These system typically assume a single phase porous layer below the CO_2-brine interface with a fixed concentration at the top layer, as shown in Fig. 1.3(a). That is, the two phase boundary between the supercritical CO_2 and brine is typically considered to be rigid, impermeable, stationary and saturated. The assumption of rigidity is motivated by the consideration that the supercritical CO_2 is lighter then brine. The density variation across the interface is much more stably stratified in the CO_2 phase than the unstable stratification within the underlying mixture of dissolved CO_2 and brine. As a result, interface deformations due to convection in the mixture are substantially damped. While, these considerations are theoretically appealing, they have yet to be verified experimentally. The assumption of impermeability, is

due to thermodynamic considerations which state that the dissolution across the interface is mostly in one direction, i.e., from the supercritical phase to the aqueous phase. The assumption of constant CO_2 concentration is justified by that the pressure is constant and diffusion is the rate limiting factor. Because dissolution occurs at constant temperature, the interface is assumed to remain stationary.

The diffusive boundary layer in a porous medium, as shown in figure 1.3(b), is characterized by two main regimes: linear regime where the nonlinear effects are negligible; and the nonlinear regime where the nonlinear mechanisms become important. Direct numerical simulations suggest that for a small perturbation amplitude, the nonlinear effects increase slowly and the linear regime extends for considerable time beyond the critical time of instability, t_c [86]. The linear stability analysis of diffusive boundary layers in porous media provides the details of early growth rate of convective mixing, for instance, the critical time of instability, and initial wavelength of instability.

For this type of flow, the stability analysis dates back to the early work of Lapwood [59] where he investigates the breakdown of stability in porous media analog of Rayleigh-Benard convection, assuming a steady porous layer of unbounded horizontal extent. The stability analysis of Rayleigh-Benard convection, where the fluid system is heated from below and cooled from above, is well established, owing to linear and steady base-flow [22]. In this case, the linear stability problem can be formulated as an eigenvalue value problem where the most unstable mode indicates the stability of the system in time. In comparison to classical Rayleigh-Benard convection, the base-flow of the diffusive boundary layer is time-dependent. This, in

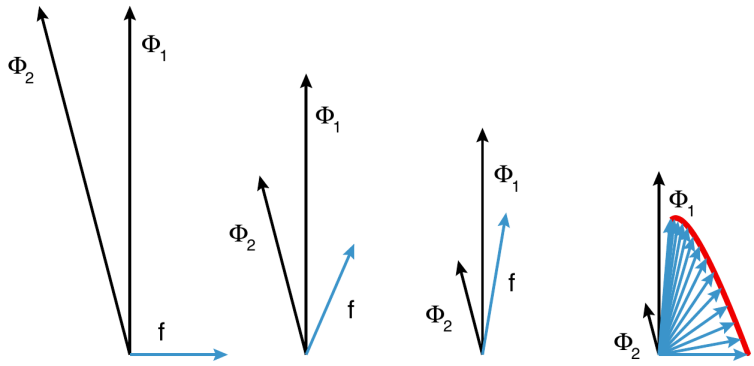

Figure 1.4: Vector example of transient growth [91]: Consider the evolution of an initial condition f composed of the difference between two eigenmodes ϕ_1 and $\phi 2$ where both eigenmodes decay in time from left to right, at different rates. As a result, f increases during a transient growth before eventually decaying while becoming parallel to the mode with slowest decay.

turn, results in a non-autonomous flow operator $\mathcal{A}$, where $\mathcal{A}$ represents the linearized governing equation. Consequently, the classical stability analysis procedure suitable for fluid system with a steady base-flow are not suitable. In addition, the flow operator is non-normal, i.e. $\mathcal{A}\mathcal{A}^+ \neq \mathcal{A}^+\mathcal{A}$, where $\mathcal{A}^+$ is the associated adjoint operator of $\mathcal{A}$ [21, 81, 106]. This indicates the superposition of non-orthogonal eigenmodes of the flow operator has the potential for a transient growth rate, while the most unstable mode, that is a measure of instability of the system, decays in time [91].

The techniques used for stability analysis of diffusive boundary layers fall into two general categories: (i) quasi-steady-state approximation (QSSA); and (ii) initial value problem (IVP). In QSSA, the linearized flow operator is reduced to an autonomous operator, assuming a steady base-flow at some specific time, followed by a modal analysis of the new set of governing equations [40, 61, 88]. At early time $t \leq t_c$, the boundary layer experience a rapid growth rate that is larger than the

growth rate of the perturbation, hence violating QSSA assumption.

The second technique solves the full non-autonomous linearized problem subjected to a prescribed initial condition by converting the linearized governing equation into a set of coupled ordinary differential equations. The main difficulty with IVP technique is the selection of an initial condition which is required to solve the differential equations. Considerable variation in the stability characteristics have been reported due to use of various initial conditions considered [13, 25, 33, 42, 54]. Consequently, two methods have emerged to provide a physically realistic initial conditions for the IVP method. The first approach, motivated by experimental observation, involves the transformation of linearized flow operator to a self-similar coordinate system [9, 55, 86]. This allows the eigenvectors of the newly transformed operator to be localized within the diffusive boundary layer, hence resolving the details of early growth rate of perturbation, namely the critical wavelength and time of instability. The dynamic of perturbations, obtained from this technique as well as the QSSA methods, are based on modal analysis, where the stability characteristic is governed by the most unstable eigenmode. In modal analysis, the exponential growth (or decay) of infinitesimal perturbations, imposed on the based flow, are determined by examining the growth rate of the dominant eigenvalue of a linear flow operator which posses normal-modes (eigenvectors). However, the eigenmodes obtained from both transformed IVP and QSSA are non-orthogonal [81], due to non-normal flow operator $\mathcal{A}$, hence an estimation of transient energy growth associated with the eigenvectors is required. Therefore, the most unstable eigenmode may not be an indicator of the dynamics of the perturbations, consequently the maximum

growth rate may be associated with some linear combination of the eigenvectors of the flow operator.

The second approach employs a non-modal stability analysis to determine a realistic initial condition with the largest perturbation amplification. In contrast with the previous techniques, non-modal stability theory provides the framework to address the transient growth of the linearized flow operator. The non-modal stability theory determines the maximum energy growth of disturbances in a finite time interval by considering all possible initial disturbances [29, 30, 92]. The initial disturbance yielding the maximum energy growth is called an optimal initial condition. The following two approaches are common to determine the optimum initial profile: (i) singular value decomposition technique; and (ii) an adjoint-based optimization technique. In the first approach, the optimal growth is obtained by performing a singular value decomposition (SVD) technique to the operator. The largest singular value and the corresponding singular vector provide the optimal growth and the optimal initial conditions, respectively. Rapaka et al. [81, 82] used this approach to obtain the optimal perturbation growth rate in homogeneous as well as heterogeneous porous media. The second approach relies on using a classical optimization technique to maximize the disturbance growth rate, also called the objective or cost function in optimization terminology, with a suitable initial condition. The optimization scheme is based on the Lagrangian formulation and Lagrangian multipliers, which is best suited for constrained optimization problems. This technique was used to study the non-modal optimal growth in Rayleigh-Benard-Marangoni convection [21] and transient diffusive porous boundary layer [17]. A detailed dis-

cussion of non-modal stability theory is provided in [91].

1.3 Outline of Thesis

Within the current literature, several important questions are still open that are in need of further research and have not been investigated in the past. Examples of such questions are: the effects of vertical heterogeneous permeability on evolutionary stages of convective mixing; and the behavior of a continuously perturbed porous medium in terms of relevant time scales of convection onset and the corresponding nonlinear mechanism. The main objective of this thesis is to explore these two fundamental issues using multiple theoretical and high resolution numerical simulation. The expected outcome of this work is the development of a coherent framework for understanding natural convection that provides the essential groundwork for modeling geological scale systems. Two main topics are addressed in the subsequent chapter. In chapter 2, the linear regime and onset of convection in a vertically-layered porous medium is examined using a combination of linear stability analysis and direct numerical simulations. Permeability is assumed to vary periodically in horizontal plane normal to the direction of gravity. Numerical results suggests a variety of resonance are possible and a unified picture of the flow conditions necessary for the occurrence of this phenomena is explored. Comparisons are also made with homogenous systems. In Chapter 3, the effect of continuous periodic forcing on the convection mixing in a porous medium is characterized. The role of the vorticity production and the competing effects of destabilizing convective and

transverse damping on the stability behavior and dominance of convective mechanism terms is explored. Scaling relationships for the optimal onset of convection and wavenumber in terms of aquifer properties and initial perturbation magnitude as well as optimum porosity structure are also reported.

Chapter 2: Convective Mixing in Vertically-layered Porous Media: The Linear Regime and the Onset of Convection

This chapter [1] examines the effect of permeability heterogeneity on the stability of gravitationally unstable, transient, diffusive boundary layers in porous media. Permeability is taken to vary periodically in the horizontal plane normal to the direction of gravity. In contrast to the situation for vertical permeability variation, the horizontal perturbation structures are multimodal. We therefore use a two-dimensional quasi-steady eigenvalue analysis as well as a complementary initial value problem to investigate the stability behavior in the linear regime, until the onset of convection. We find that thick permeability layers enhance instability compared to thin layers when heterogeneity is increased. On the contrary, for thin layers the instability is weakened progressively with increasing heterogeneity to the extent that the corresponding homogeneous case is more unstable.

For high levels of heterogeneity, we find that a small change in permeability field results in large variations in the onset time of convection, similar to the instability event in the linear regime. However, this trend does not persist unconditionally because of the reorientation of vorticity pairs due to the interaction of

[1] This chapter has been published in Physics of Fluid as 'Convective mixing in vertically-layered porous media: The linear regime and the onset of convection' (Physics of Fluids 29, 084101 (2017)).

evolving perturbation structures with heterogeneity. Consequently, an earlier onset of instability does not necessarily imply an earlier onset of convection.

A resonant amplification of instability is observed within the linear regime when the dominant perturbation mode is equal to half the wavenumber of permeability variation. A weaker resonance also occurs when the dominant perturbation mode of the heterogeneous system coincides with the corresponding homogeneous system. On the other hand, substantial damping occurs when the perturbation mode is equal to the harmonic and sub-harmonic components of the permeability wavenumber. The phenomenon of such harmonic interactions influences both the onset of instability as well as the onset of convection.

2.1 Overview

Density-driven instability in porous media associated with carbon dioxide sequestration in brine-saturated aquifers has received significant attention in the past few decades [75]. Following the injection of the supercritical CO_2 into a brine-saturated aquifer, the lighter CO_2 forms a layer between the impermeable cap rock and the heavier brine as shown in Fig. 3.1. Over time, CO_2 dissolves into the underlying brine across the two-phase interface and forms a transient diffusive boundary layer. Since CO_2-rich brine is denser than the underlying brine, the layer becomes gravitationally unstable. This, in turn, results in the formation of finger-like structures that convect CO_2 downward, leading to an increase in the rate of CO_2 dissolution. Given the rapid rate of CO_2 dissolution, the two-phase region at the top

boundary is often modeled as a single phase system with a constant concentration value at the top boundary, as shown in Fig. 3.1. Understanding the convection process in terms of predicting the onset of instability and convection, as well as characterizing the corresponding instability mechanisms provides a rigorous measure to quantify the details of the physical processes governing convective mixing.

Flow and transport in heterogeneous media are governed by specific permeability patterns, which determine the dominant flow paths and influence the behavior of convective mixing, especially when the length scales of convection and permeability are similar [100]. A number of previous investigations into convective mixing in porous media assumed uniform permeability [26, 45, 81, 86, 95], i.e., a homogeneous medium. Actual geologic formations, however, contain inhomogeneity in permeability across a wide range of length scales as a result of various depositional and tectonic processes [72, 101] involved in the formation of geologic strata. Typical formations are composed of distinct layers, blocks, and sedimentary rocks with grain sizes varying from coarser sand to finer clay that creates spatial variations of permeability [8].

In contrast to homogeneous porous media, theoretical estimates of flow instability are not as well characterized for heterogeneous media. Within the current literature, various studies have examined the effect of heterogeneity on convective mixing in the classical Rayleigh-Bénard problem [66, 73], subsurface contaminant transport [79, 90, 94], and convective dissolution [15, 16, 28, 80, 82, 112]. These studies focused on either horizontal layering or random permeability variations. Using different degrees of permeability variations and spatial correlation lengths, quan-

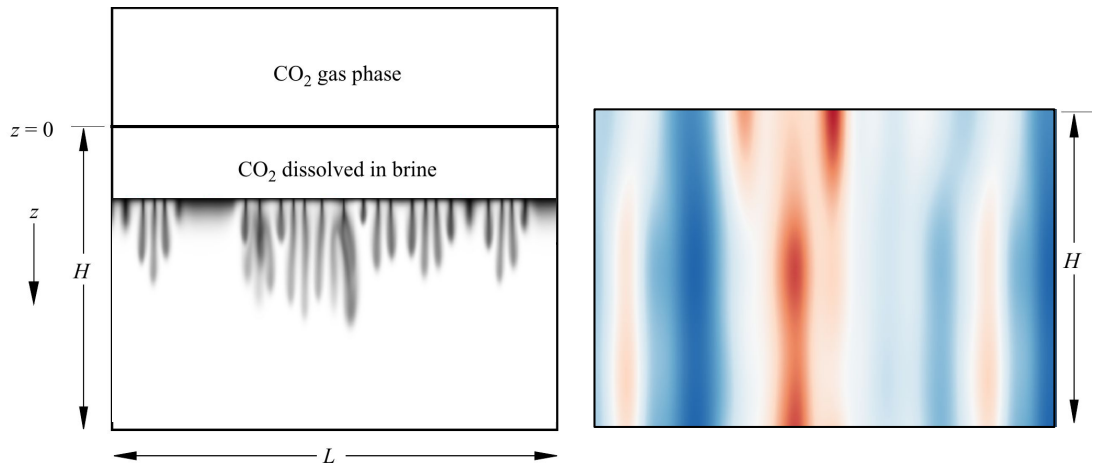

(a) (b)

Figure 2.1: (a) Schematic of the 2-D system considered in the current study. CO_2 gas forms a layer along the impermeable top boundary. At time $t = 0$, CO_2 begins dissolving into the underlying brine. Unstable density stratification leads to the formation of convective fingers, indicated by concentration contour, (b) The corresponding correlated random permeability field.

titatively different instability characteristics were reported depending on weak or strong permeability variation assumptions.

In geologic media, permeability variation often occurs primarily in a direction normal to the bedding plane. The bedding plane itself, however, can be oriented at various angles with respect to the direction of gravitational acceleration as a result of tectonic processes, for example in subduction zones [1]. The relevant permeability field thus contains elements of both "vertical" and "horizontal" permeability variation with respect to buoyancy driven flow. In addition, various other factors lead to the creation of cross bedding structures which may give rise to axial permeability variation, parallel to the bedding plane. One such process is boudinage [32] that creates breaks in the formation layering parallel to the bedding plane to produce ge-

ologic features known as boudins. In this process, layers are extended into separate pieces through plastic and brittle extensional deformation mechanisms. In the case of mostly plastic extensions, pitch-and-swell structures are formed by the process known as necking. Other cross plane features such as syntectonic veins are known to occur in metamorphic rocks [48]. Permeability is also known to vary horizontally in so-called composite reservoirs where vertical layering often occurs due to drilling, completion practices, water flooding or gas injection [101,105]. The composite reservoir may then be represented as an assembly of vertical regions each with a different value of average permeability.

In the present work, we study the effect of horizontal variation of permeability on the stability of the convective mixing process. The permeability heterogeneity is taken to occur in the form of vertical layers, i.e. a series of vertical blocks arranged in series. This approach allows a systematic investigation of instability mechanisms governing the interaction of perturbations with horizontal heterogeneity. This assumption, although limiting, provides a basic framework for the analysis of more complex variations of permeability.

The effect of horizontal heterogeneity for the classical Darcy-Bénard problem, where a porous layer is heated uniformly from below, have been examined in the past [41,65,71,84]. McKibbin [65] investigated the convection pattern and heat flux distribution in vertically-layered media with varying contrasts of permeability and thermal conductivity, in addition to studying a fault zone with permeable lateral walls. A useful literature survey on the effect of vertical and horizontal variation of heterogeneity on thermal convection for the classical Darcy-Bénard problem is

provided by Nield and Bejan [72]. Natural convection for the transient boundary layer problem with horizontal heterogeneity, however, has been relatively less studied. An experimental investigation of transient natural convection for a reactive solute in a Hele-Shaw cell with non-uniform permeability was reported earlier by Horváth *et al.* [50]. In that case, horizontal heterogeneity was created using periodic modulation of the gap width in the horizontal direction.

The stability analysis of diffusive boundary layers involves the study of non-autonomous and non-normal linear operators [81]. We use two complementary methods of linear stability analysis that are common for such problems [86, 111]; the quasi-steady eigenvalue problem (EVP) in self-similar space and the initial value problem (IVP). In contrast to both homogeneous [27, 86, 93, 106] and vertically heterogeneous [16] media, the spanwise eigenmodes of linearized disturbances in our case are composed of multiple Fourier modes. Consequently, the standard eigenvalue analysis can not be used for tracking the evolution of individual small amplitude perturbation modes. We therefore perform a 2-D quasi-steady eigenvalue analysis (2D-EVP) [103] that has not been used previously for such problems. The 2-D eigenvalue analysis provides a robust framework to investigate instability characteristics associated with multiple interacting horizontal modes. The eigenvalue analysis is carried out in the self-similar space of the diffusive base-state to filter out unphysical perturbations that are not confined to the diffusive boundary layer at all times [106]. In order to study the behavior of discrete modes imposed at an initial time, we use a complementary, two-dimensional initial value analysis. We also carry out direct numerical simulation of the fully nonlinear problem to investigate

the effect of horizontal heterogeneity on the onset time of nonlinear convection and examine the extent to which heterogeneity enhances convective mixing.

This study is organized in the following manner. We present the governing equations in Sec. 3.2.1, followed by a description of the methods used in this work. In Sec. 2.3, we investigate the effect of permeability structure on the dominant growth and resonance in the linear regime using the EVP method. In Sec. 2.4, we discuss the effect of perturbation structures in the linear regime using the IVP technique. In Sec. 2.5, we perform direct numerical simulations to characterize the onset of convection in porous media with horizontal permeability variation, followed by a summary of our finding in Sec. 3.4.

2.2 Governing equations and methodology

We consider a two-dimensional canonical configuration where an isotropic single-phase brine-saturated porous layer of infinite width and depth of H, is bounded by a layer of CO_2 at $z = 0$ and impermeable rock at $z = H$, as illustrated in Fig. 3.1. The porous layer is characterized by porosity ϕ, average permeability $\bar{\mathcal{K}}$, and dispersion coefficient $\mathcal{D}$. Initially, the porous layer is at rest with a constant density, ρ_0, and zero CO_2 concentration, $c = 0$. We assume the CO_2–brine mixture, with a constant density of ρ_1 and concentration of c_1, is provided at the top layer, $z = 0$. This assumption is justified by the fact that the dissolution process is fast compared with the time of fluid motion such that the two-phase region at the top boundary can be simplified to a single phase system with a constant concentration value at

$z = 0$ [24, 26, 62].

We model the density driven flow of a single-phase miscible fluid in porous media using the volume averaged form of the continuity equation, the Darcy's law, and the volume averaged advection-diffusion equation. Because the density variation between the fully saturated CO_2–brine mixture and pure brine in typical aquifer is around 2%, [26, 35, 97], we assume that density, ρ, varies linearly with the concentration: $\rho = \rho_0 + \Delta\rho c$ where $\Delta\rho$ is the density difference between the saturated CO_2–brine mixture and pure brine. This justifies the use of Boussinesq approximation in the governing equations. Furthermore, the fluid viscosity, μ, is assumed to be constant because under typical aquifer conditions, the viscosity difference between brine and aqueous CO_2–brine is negligible [26]. Because the spatial variation of porosity is reported to be small, we assume a constant porosity value. Following the standard procedure [86], the domain depth, H, buoyancy velocity $U = \bar{\mathcal{K}}\Delta\rho g/\mu$, $t = \phi H/U$, and pressure $p = \Delta\rho g H$ are taken as the characteristic scaling parameters for non-dimensionalization of the governing equations. A dimensionless form of governing equations and boundary conditions may be expressed as,

$$\nabla \cdot \mathbf{u} = 0, \qquad \mathbf{u} = -\mathcal{K}\left(\nabla p - c\hat{\mathbf{z}}\right), \qquad \frac{\partial c}{\partial t} + \mathbf{u} \cdot \nabla c = \frac{1}{Ra}\nabla^2 c \tag{2.1}$$

$$c\Big|_{x,z=0} = 1, \qquad \frac{\partial c}{\partial z}\Big|_{x,z=1} = 0, \qquad w\Big|_{x,z=0} = w\Big|_{x,z=1} = 0 \tag{2.2}$$

where $\mathbf{u} = (u, w)$ is the Darcy velocity, c is the concentration of dissolved CO_2, p is the pressure, $\hat{\mathbf{z}}$ is the unit normal in the direction of gravity, and the Rayleigh

number is defined as $Ra = UH/(\phi D)$, where D is molecular diffusion. Convective mixing in porous media may, however, involve both diffusion and dispersion as a result of various correlation length scales associated with permeability. The general dispersion tensor, $\mathcal{D}$, can be defined as [8, 85],

$$\mathcal{D} = \left(\frac{1}{Ra} + \frac{1}{Pe}\mathbf{u}\right)\mathbf{I} + \frac{1}{Pe}\left(1 + \frac{\alpha_T}{\alpha_L}\right)\frac{1}{|\mathbf{u}|}\mathbf{uu} \tag{2.3}$$

where α_L and α_T are the longitudinal and transverse dispersivities, respectively, and the Peclet number is defined as $Pe = H/\phi\alpha_L$. In order to determine the conditions under which molecular diffusion dominates, we consider the ratio, Ra/Pe, for typical values [26] of $\mu = 5 \times 10^{-4}$ Pa s, $D = 10^{-9}$ m^{2}s^{-1}, $\bar{\mathcal{K}}$= 10^{-12} m^2, $g = 9.81$ m s^{-2}, $\Delta\rho = 30$ kg m^{-3} and $\alpha_L = 10^{-5}$ ms^{-1},

$$Ra/Pe = \bar{\mathcal{K}}\Delta\rho g\alpha_L/\mu D \sim \mathcal{O}\left(10^{-3}\right) \tag{2.4}$$

Under such conditions, it would be feasible to neglect the velocity related contribution of dispersion such that $\mathcal{D} \sim 1/Re\,\mathbf{I}$. Dispersivity, α_L, varies over a wide range as a function of Ra and increases with an increase in the Rayleigh number. According to the data reported by Delgado [20], the effect of dispersion is significant for $Ra > 10^4$. The value of $\alpha_L = 10^{-5}$ used in the calculation of Ra/Pe in Eq. 2.4 corresponds to $Ra = 5 \times 10^3$. In the present work, we can therefore neglect velocity induced dispersion if we limit the applicability of our results to smaller Ra values.

The spatial variation of permeability in real geologic media is quite complex.

Across any sample of geologic scale, permeability is likely to vary typically at different rates in different directions at multiple scales. In practice, the principle directions of the permeability tensor are also expected to vary from point to point in space, making it difficult to use a coordinate system that can effectively diagonalize the permeability tensor and reduce the permeability variation to its principle components [8]. In the present study, we assume a simple spatially periodic permeability variation and an isotropic permeability tensor to examine natural convection in a vertically-layered porous medium. These variations could be natural to the subsurface rocks or caused by drilling operations. The dimensionless permeability field takes the following form,

$$\mathcal{K}(x) = \exp\left(a_p \cos(k_p x)\right) \tag{2.5}$$

where k_p is the permeability wavenumber, x is the horizontal direction normal to the direction of gravity, and a_p is the permeability amplitude which indicates the strength of permeability contrast. Equation 2.5 allows a smooth spatial variation of permeability, with a constant correlation length of $2\pi/k_p$, to study the effect of permeability heterogeneity from a fundamental perspective. The permeability field is normalized such that $\int_0^1 \mathcal{K}(x)dx = 1$, which is then used to define the average permeability, $\bar{\mathcal{K}}$, used as the characteristic permeability value.

We use stability analysis to quantify the perturbation growth rate, as well as providing sufficient conditions for triggering instability. The stability analysis is based on linearization of Eq. 3.1, obtained by imposing infinitesimal perturbations on the base-flow. In general, the linearized governing equations can then be rewritten

as an eigenvalue problem where the most unstable mode indicates the stability of the system in time. However, the linear operator corresponding to diffusive boundary layer in porous layer is non-autonomous and non-self-adjoint [81], hence, the classical stability analysis approach is not strictly valid. In the present study, we follow Tilton *et al.* [106] in carrying the stability analysis in the self-similar space of the diffusion operator to accurately capture the linear growth dynamics. We next evaluate the effectiveness of the EVP analysis by comparing the results obtained with IVP.

We carry out the stability analysis by defining the flow variables as the sum of the base-state and small perturbations,

$$c = c_b(z,t) + \widetilde{c}(\mathbf{x},t), \quad \mathbf{u} = \widetilde{\mathbf{u}}(\mathbf{x},t) \quad p = p_b + \widetilde{p}(\mathbf{x},t) \tag{2.6}$$

where $\widetilde{c}(\mathbf{x},t)$, $\widetilde{\mathbf{u}}(\mathbf{x},t)$, $\widetilde{p}(\mathbf{x},t)$ are time-dependent perturbation profiles, and c_b is the concentration base-state. The quiescent transient base-state is obtained by setting $\mathbf{u} = 0$ in equation (3.1) coupled with equation (2.2) which leads to,

$$c_b(z,t) = 1 - \frac{4}{\pi}\sum_{n=1}^{\infty}\frac{1}{2n-1}\sin\left[\left(n-\frac{1}{2}\right)\pi z\right]\exp\left[-\left(n-\frac{1}{2}\right)^2\frac{\pi^2 t}{Ra}\right] \tag{2.7}$$

Substituting (2.6) into the governing equations (3.1), and removing the pressure term by imposing the divergence free condition, followed by linearizing about the base-state, c_b, we obtain the following system of linear equations in terms of the concentration field $\widetilde{c}(\mathbf{x},t)$ and streamfunction $\widetilde{\psi}(\mathbf{x},t)$, along with the corresponding

boundary conditions,

$$\frac{\partial \widetilde{c}}{\partial t} + \frac{\partial \widetilde{\psi}}{\partial x}\frac{\partial c_b}{\partial z} - \frac{1}{Ra}\mathscr{D}\widetilde{c} = 0, \qquad \mathscr{D}\widetilde{\psi} - \frac{1}{\mathcal{K}}\frac{\partial \mathcal{K}}{\partial x}\frac{\partial \widetilde{\psi}}{\partial x} - \mathcal{K}\frac{\partial \widetilde{c}}{\partial x} = 0 \tag{2.8}$$

$$\widetilde{c}\Big|_{z=0} = \frac{\partial \widetilde{c}}{\partial z}\Big|_{z=1} = \widetilde{\psi}\Big|_{z=0} = \widetilde{\psi}\Big|_{z=1} = 0, \qquad \widetilde{c}|_{x=0} = \widetilde{c}|_{x=L}, \qquad \widetilde{\psi}|_{x=0} = \widetilde{\psi}|_{x=L} \tag{2.9}$$

where $\mathscr{D} = \partial^2/\partial z^2 + \partial^2/\partial x^2$. This set of coupled partial differential equations is an initial value problem (IVP) associated with time varying concentration and streamfunction perturbations, $\widetilde{c}$, $\widetilde{\psi}$. The compact form of IVP may be expressed as,

$$\frac{\partial \widetilde{c}}{\partial t} = \mathscr{A}(t, \mathbf{x})\widetilde{c}, \qquad \widetilde{c}(z, t_p) = c_p(z) \tag{2.10}$$

where t_p is the time at which the flow is perturbed, and $\mathscr{A}$ is the two-dimensional linear flow operator. The operator $\mathscr{A}$ is non-autonomous due to the transient concentration base-state, which in turn results in the sensitivity of stability analysis to the initial perturbation time, t_p. An initial condition, $c_p(z)$, which is not known a priori, is required to solve the IVP problem. We use the dominant mode of the diffusion operator, which is the leading-order term of a Hermite polynomial expansion in self-similar space [9, 86], as an initial condition for the IVP problem, Eq. (2.10). The "dominant mode" of Ben *et al.* [9] and Riaz *et al.* [86] is concentrated within boundary layer and it is consistent with experimental observations. Based on the transformation $\xi = \alpha z$ where $\alpha = \sqrt{Ra/4t}$, we rewrite equation (2.10) in the time-dependent self-similar coordinates of (x, ξ, t) where the compact form of IVP

may be expressed as,

$$\frac{\partial \widetilde{c}}{\partial t} = \mathscr{B}(t, x, \xi)\widetilde{c}, \qquad \widetilde{c}(\xi, t_p) = \xi \mathrm{e}^{-\xi^2} \tag{2.11}$$

The IVP problem is solved with spectral-like spatial accuracy using a 6^{th} order compact scheme for spatial derivative discretization of $\mathscr{B}$, and a 4^{th} order Runge-Kutta scheme for time integration. The time evolution of perturbation growth rate is calculated based on the L_2 norm of the concentration perturbation field, which is reported to be a good predictor of the dominant perturbation path [106], according to the following relation,

$$\sigma = \frac{1}{\|\widetilde{c}\|_2} \frac{\partial \|\widetilde{c}\|_2}{\partial t} \tag{2.12}$$

where σ represents the instantaneous growth rate.

An alternative approach for studying the linear behavior is the quasi-steady eigenvalue analysis which is essentially a modal analysis with time as a parameter. In the case of horizontal variation of permeability, perturbations are composed of multiple Fourier modes. Hence, a two dimensional quasi-steady eigenvalue analysis is used.

We split the concentration and streamfunction perturbations into spatial and temporal components, assuming an identical exponent time independence of the form,

$$\widetilde{c} = c_e(\mathbf{x}) e^{\sigma(t_f)t}, \qquad \widetilde{\psi} = \psi_e(\mathbf{x}) e^{\sigma(t_f)t} \tag{2.13}$$

where t_f is the prescribed final time, σ the perturbation growth rate at $t = t_f$, and

c_e and ψ_e are eigenfunctions. By substituting equation (2.13) into equation (2.8), followed by a transformation to self-similar coordinates of (x, ξ, t), we obtain the following eigenvalue problem,

$$\sigma c_e - \frac{\xi}{2t}\frac{\partial c_e}{\partial \xi} + \alpha \frac{\partial \psi_e}{\partial x}\frac{\partial c_b}{\partial \xi} - \frac{1}{Ra}\left(\alpha^2 \frac{\partial^2}{\partial \xi^2} + \frac{\partial}{\partial x^2}\right) c_e = 0 \tag{2.14}$$

$$\left(\alpha^2 \frac{\partial^2}{\partial \xi^2} + \frac{\partial}{\partial x^2}\right) \psi_e - \frac{1}{\mathcal{K}}\frac{\partial \mathcal{K}}{\partial x}\frac{\partial \psi_e}{\partial x} - \mathcal{K}\frac{\partial c_e}{\partial x} = 0 \tag{2.15}$$

$$c_e\big|_{\xi=0} = c_e\big|_{\xi=\xi_c} = 0, \qquad \psi_e\big|_{\xi=0} = \psi_e\big|_{\xi=\xi_c} = 0 \tag{2.16}$$

$$c_e\big|_{x=0} = c_e\big|_{x=L}, \qquad \psi_e\big|_{x=0} = \psi_e\big|_{x=L} \tag{2.17}$$

where $\xi_c = 8$ is the cutoff length chosen such that the perturbations decay to zero at $\xi = \xi_c$ and the horizontal length is set to $L = 2\pi$ to resolve the integer wavenumbers in the x direction. The 2-D EVP, represented by Eqs. 2.14–2.17, can be expressed in compact form as $\mathcal{A}v = \sigma\mathcal{B}v$ where σ is the eigenvalue, $v = [c_e, \psi_e]$ is the eigenmodes, and $\mathcal{A}$ and $\mathcal{B}$ are the spatial derivative matrix obtained by using a 6^{th} order finite difference scheme. We obtain the largest eigenvalue along with the associated eigenmodes using the ARnoldi PACKage (ARPACK) at a specific time. The eigenmode with the largest eigenvalue represents the dominant perturbation structure and the corresponding eigenvalue, σ_{max}, represents the dominant growth rate of the disturbances. The growth rate obtained in the self-similar (x, ξ, t) coordinate is then transformed back to the physical space (x, z, t) according to,

$$\sigma = \sigma_\xi - \left[\int_0^L \int_0^{\xi_c} \widetilde{c}^2 \mathrm{d}\xi dx\right]^{-1} \int_0^L \int_0^{\xi_c} \frac{\xi}{2t}\widetilde{c}\frac{\partial \widetilde{c}}{\partial \xi} d\xi dx \tag{2.18}$$

where σ_ξ is the growth rate produced by EVP method in the self-similar coordinate.

As discussed above, the EVP method relies on assuming that the growth rate of the boundary layer is small compared to perturbation growth rate. This assumption is not valid at early times during which the diffusive boundary grows rapidly [106]. Additionally, the dynamic of perturbations obtained from this technique as well as the IVP method are based on modal analysis. Consequently, the transient growth associated with the eigenmodes of the flow operator is not taken into account.

2.3 Dominant growth and resonance in the linear regime

We start by examining the effect of permeability heterogeneity on the dominant growth and the critical time for the onset of instability. This will be followed by a discussion on resonant amplification using the EVP technique described in Sec. 3.2.1. We associate the onset of instability with the time at which the growth rate first becomes positive, $\sigma > 0$. The dominant mode is defined as the mode with the highest instantaneous growth rate among all the perturbed modes. The critical value of the most dangerous mode occurs at the critical time for the onset of instability, t_c. Because the growth rate obtained by the 2D-EVP technique corresponds to the most dangerous mode, the associated onset of instability represents the critical time for the onset of instability. In this analysis, the parameters of interest are; a_p, the permeability amplitude and k_p, the horizontal permeability wavenumber. Throughout the analysis, we use a fixed value of $Ra = 500$, which is typical of CO_2 sequestration [27]. Behavior at other values of Ra within the linear regime can be

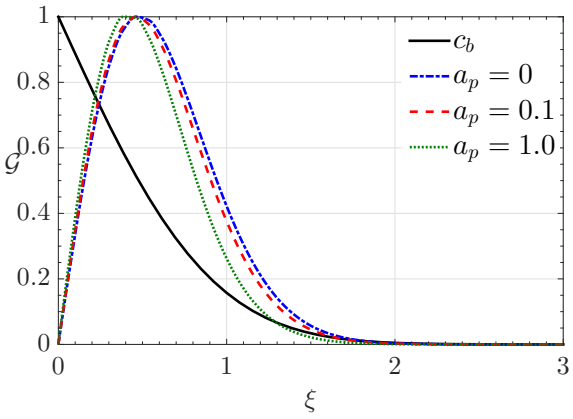

Figure 2.2: The transient diffusive boundary layer, c_b, see Eq. (2.7) along with the vertical shape function, $\mathcal{G}(\xi)$, determined by EVP for homogeneous medium and heterogeneous medium at two levels of a_p with $k_p = 10$ at $t = 2$ when $Ra = 500$. $\mathcal{G}(\xi)$ is confined within the diffusive boundary layer in all cases.

found by a simple rescaling, as discussed in Appendix 2.C.

2.3.1 Dominant growth rate

Using the EVP analysis, we examine the behavior of the instantaneous, dominant growth rate, σ_{max}, and the corresponding 2-D concentration eigenmode, $c_e(x, \xi)$, with respect to the heterogeneity amplitude, a_p, and the heterogeneity mode, k_p. The concentration eigenmode may be expressed in terms of two spatial shape functions,

$$c_e(x, \xi) = \mathcal{F}(x)\mathcal{G}(\xi) \tag{2.19}$$

where $\mathcal{F}(x)$ varies periodically in the x-direction while $\mathcal{G}(\xi)$ is concentrated within the diffusive boundary layer.

Figure 2.2 compares the vertical shape function, $\mathcal{G}(\xi)$, for a homogeneous medium (dash-dotted line) with that of a heterogeneous medium with $k_p = 10$,

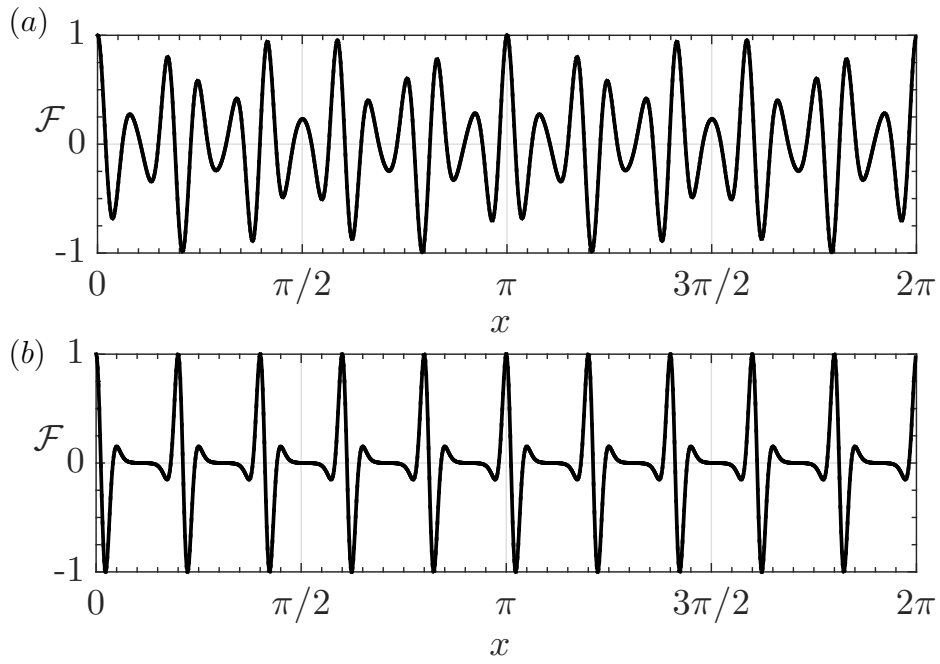

Figure 2.3: Variation of concentration eigenmode, c_e, obtained by EVP at $z = 0$ in the spanwise direction when $Ra = 500$, $k_p = 10$, and $t = 2$. (a) $a_p = 0.1$, (b) $a_p = 1.0$. The shape of $\mathcal{F}(x)$ indicates that the concentration eigenmodes are multimodal.

$a_p = 0.1$ (dashed line) and $a_p = 1$ (dotted line), when $t = 2$. $\mathcal{G}(\xi)$ is observed to be confined within the diffusive boundary layer in all cases. For small a_p, $\mathcal{G}(\xi)$ is similar to its homogeneous counterpart but is relatively more localized within the boundary layer, when $a_p = 1$.

Figure 2.3 shows the horizontal shape function, $\mathcal{F}(x)$, for the heterogeneous medium with $a_p = 0.1$ (top panel) and $a_p = 1$ (bottom panel), when $k_p = 10$, $Ra = 500$, and $t = 2$. In contrast to the homogeneous system, the concentration eigenmodes, c_e , are more complex in shape indicating that they can no longer be characterized by a single mode.

We apply Fourier transform to the concentration eigenmode to obtain the constituent Fourier modes. Figure 2.4 compares the Fourier cosine coefficients, m_l, and

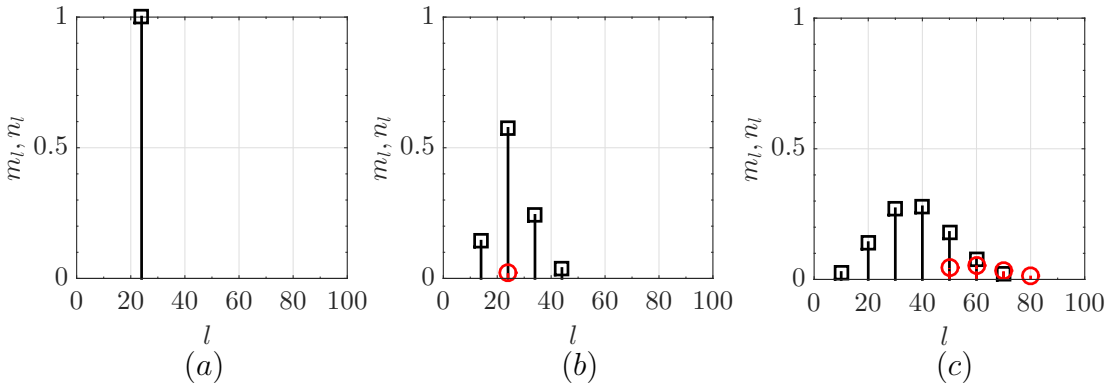

Figure 2.4: Fourier cosine coefficients, m_l (square symbols), and sine coefficients, n_l (circle symbols) of the concentration eigenmode obtained by EVP, when $t = 2$ and $Ra = 500$. (a) homogeneous system, and heterogeneous system with $k_p = 10$ when (b) $a_p = 0.1$, and (c) $a_p = 1$.

sine coefficients, n_l, for $\mathcal{F}(x)$ shown in Fig. 2.3. The homogeneous case in Fig. 2.4(a) yields $l = 24$ in agreement with 1-D results for homogeneous media [106]. For heterogeneous media, Fig. 2.4(b–c) shows that $\mathcal{F}(x)$ consists of multiple horizontal modes. Hence, for horizontal heterogeneity, multiple unstable modes simultaneously contribute to instability. For $a_p = 0.1$, $\mathcal{F}(x)$ consists of $l = 4, 14, 24, 34, 44, 54$, among which the homogeneous mode, $l = 24$, is dominant. A higher level of heterogeneity, $a_p = 1$, gives rise to more modes, as shown in Fig. 2.4(c), along with a wider spectrum with a relatively smoother distribution of the modal amplitude which now does not contain the homogeneous mode.

Figure 2.5 shows the effect of permeability wavenumber on the temporal evolution of the dominant growth rate, σ_{max}, for $a_p = 0.1$ and 1 when $Ra = 500$ and $k_p = 0, 1, 10, 60$, and 120. Initially, the perturbation growth rates are negative due to the stabilizing effect of diffusion. Figure 2.5(a) shows that the homogeneous medium, $k_p = 0$, has the smallest growth rate while the largest value of σ_{max} is observed for $k_p = 1$. As indicated in Fig. 2.5(a), σ_{max} decreases with an increase

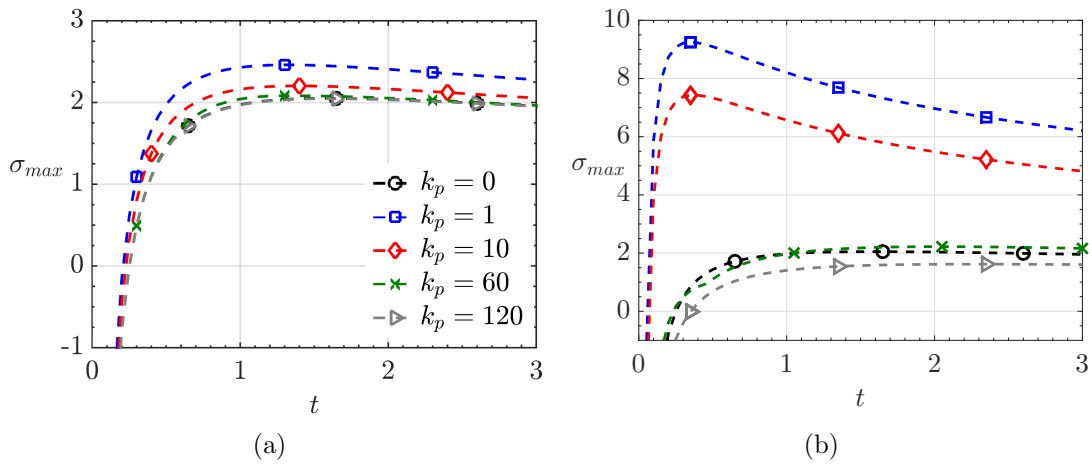

Figure 2.5: (color online) Effect of permeability wavenumber on the temporal evolution of σ_{max} obtained by EVP for $Ra = 500$. (a) $a_p = 0.1$, (b) $a_p = 1.0$. $k_p = 0$ corresponds to the homogeneous medium. Heterogeneity amplifies instability beyond the homogeneous case more effectively for larger a_p and smaller k_p.

in the permeability wavenumber. This shows that when heterogeneity is low, the growth rate in thin layers is similar to that in homogeneous media. In the case of higher heterogeneity, small values of k_p result in substantial enhancement of σ_{max}, as shown in Fig. 2.5(b). The dominant growth rate decays for larger k_p, similar to the case of $a_p = 0.1$ shown in plot 2.5(a), but in this case σ_{max} sinks below the corresponding homogeneous value for a large enough k_p of 120, indicating a weakened instability.

The effect of permeability wavelength, k_p, and the heterogeneity magnitude, a_p, on the critical time of the onset of instability, t_c, is summarized in Fig. 2.6 for $0 \leq k_p \leq 120$ and $0.1 \leq a_p \leq 2$. The behavior of t_c, shown in Fig. 2.6, can be divided into two distinct regimes; one for $k_p \leq 60$, where t_c decreases with an increase in heterogeneity and the other for higher values of k_p where t_c increases with an increase in heterogeneity. We would also like to note the non-monotonic

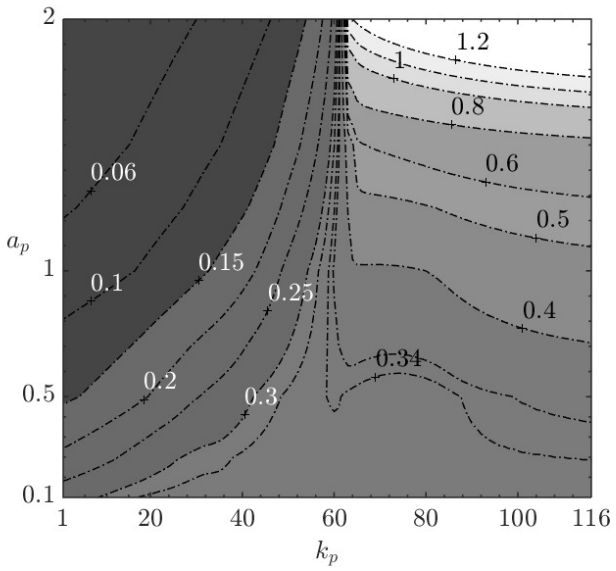

Figure 2.6: Effect of permeability amplitude and wavenumber on the critical time for the onset of instability, t_c, determined by EVP. Contour labels show the value of t_c. With an increase in heterogeneity, t_c is delayed for thin permeability layers but occurs earlier for thick layers.

behavior of a_p as a function of k_p around $a_p = 0.5$ and $k_p = 60$, which is related to the phenomenon of resonant amplification that will be discussed in more detail in the next section.

Overall, Fig. 6 indicates that instability decreases with an increase in heterogeneity for thin layers of vertical permeability but increases with an increase in heterogeneity for thick layers. For thin layers, the prolongation of the onset time of instability beyond $t_c = 0.25$ for homogeneous media is substantial for higher values of heterogeneity.

2.3.2 Resonant amplification

Previous studies of miscible flow in heterogeneous porous media suggest that a resonant amplification of the perturbation growth rate may occur when pertur-

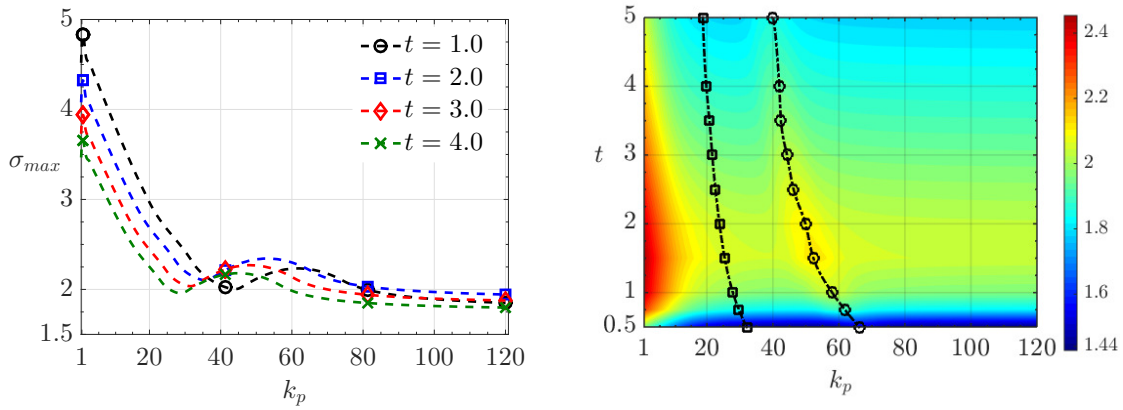

Figure 2.7: (a) Variation of σ_{max} vs permeability wavenumber when $a_p = 0.5$ obtained by EVP, (b) Contours of σ_{max} vs k_p when $a_p = 0.1$ obtained by EVP. The symbols mark the location of resonant wavenumber. The perturbation growth experiences a resonant amplification.

bations interact with the permeability field in some optimal manner [19, 87]. We examine whether a similar phenomenon occurs in vertically-layered porous media. Figure 2.7(a) compares the dominant growth rate, σ_{max} at different times and various permeability wavenumbers in the range of $0 \leq k_p \leq 120$ when $a_p = 0.5$. The most unstable case is $k_p = 1$. The growth rate decays for larger values of k_p. However, $\sigma_{\max}$ does not decay monotonically but attains a local maximum, σ_{res}, due to resonant amplification at certain wavenumbers. The affected wavenumbers are observed to shift progressively to lower values with increasing time. For a small a_p of 0.1, the dominant growth rate experiences two resonant amplifications that are marked with symbols in Fig. 2.7(b). The bandwidth of the second resonant (circles) amplification grows to its maximum around $t = 1$ and it is significantly larger than the first resonant amplification. The first resonant effect (squares), as shown in Fig. 2.7(b), vanishes for large value of permeability amplitude.

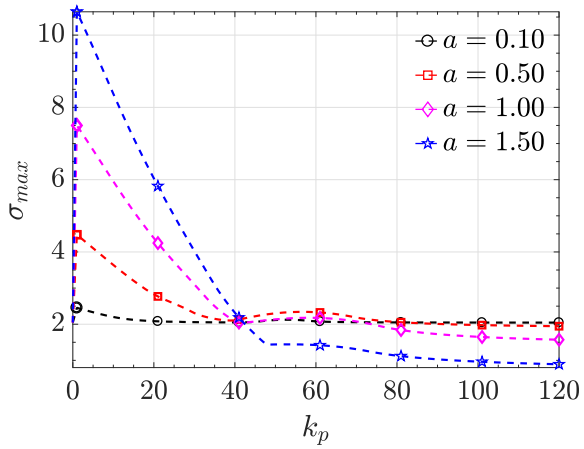

Figure 2.8: Effect of a_p on the dominant growth rate vs permeability wavenumber when $t = 1.5$ obtained by EVP.

Figure 2.8 shows the effect of permeability contrast on the dominant growth rate, σ_{max} for various permeability wavenumbers when $t = 1.5$. σ_{max} increases systematically with an increase in permeability contrast, a_p, when the permeability wavelength is large. On the other hand, for small permeability wavelength, the decay of σ_{max} becomes significant at higher values of the a_p. σ_{max}, as indicated in the figure, undergoes a resonant amplification for four levels of permeability amplitude considered in Fig.2.8. With an increase in heterogeneity, a_p, the location of the resonant amplification shifts to larger permeability wavenumbers k_p while the resonance bandwidth becomes slightly wider. The behavior of the growth rate is consistent with regimes observed in Fig. 2.6.

Figure 2.9 shows the time history of σ_{res} and the corresponding resonant wavenumber, k_{res}, for different levels of heterogeneity, a_p. The resonant wavenumber, k_{res}, decays monotonically in time. This is expected because of the increase in the thickness of the diffusive boundary layer with time. The behavior of σ_{res}, as

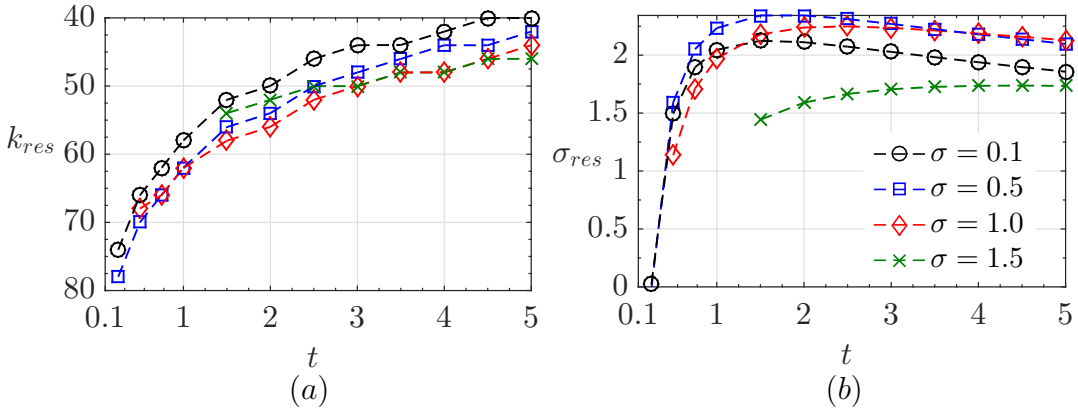

Figure 2.9: The EVP results for various values of a_p. (a) Time history of the resonant wavenumber, (b) The evolution of σ_{max} at resonant location. The resonant wavenumber shifts to a lower value due to the growth of diffusive boundary layer.

illustrated in Fig. 2.9(b), changes non-monotonically with a_p at small times when $a_p = 0.5$ has the highest resonant growth rate. At late times, $a_p = 1$ leads to the maximum value of σ_{res}. In the case of $a_p = 1.5$, σ_{res} is the smallest because thin layers with high heterogeneity are less unstable, as noted in Fig. 2.6.

In order to develop a physical understanding of the conditions under which resonant amplification occurs, we analyze the interaction of horizontal permeability with perturbation structures by considering the vorticity equation. The vorticity equation, obtained by taking curl of the Darcy equations, may be expressed as,

$$\Omega = \underbrace{\mathcal{K}\nabla c \times \nabla z}_{\Omega c} + \underbrace{\nabla(\ln\mathcal{K}) \times \mathbf{u}}_{\Omega p} \tag{2.20}$$

Equation 3.29 indicates two sources of vorticity production; Ω_c is related to the horizontal gradient of concentration field and Ω_p is associated with the gradient of permeability. With permeability variation, the direction of vorticity production associated with each term determines the strength of instability mechanism. In-

stability is enhanced when Ω_c and Ω_p coincide spatially and are of the same sign. In order to quantify the resonant amplification, we define the following norm to measure the perturbation magnitude,

$$E_l^p = \left[\frac{1}{\lambda_l}\int_0^{\lambda_l}\int_0^1 \tilde{\mathbf{q}}^p \cdot \tilde{\mathbf{q}}^p \, dz\, dx\right]^{\frac{1}{2}} \quad \text{where} \quad p = [\Omega_c, \Omega_p, \Omega, \mathcal{E}] \tag{2.21}$$

where E_l^p is the magnitude of the horizontal Fourier mode of the perturbation field, $\tilde{\mathbf{q}}^p$, integrated in the vertical direction and p refers to the perturbation field based on the vorticity components, Ω_c, Ω_p, Ω, defined in Eq. 3.29, and the combined effect of concentration and velocity perturbations is represented by $\mathbf{q}^{\mathcal{E}} = [\tilde{u}, \tilde{w}, \tilde{c}]$. The Fourier components of the perturbation concentration, velocity, and vorticity fields are obtained with the standard FFT routines. The use of $\mathbf{q}^{\mathcal{E}}$ is motivated by the fact that nonlinearity arises from the convective term, $\mathbf{u} \cdot \nabla c$, in the advection-diffusion equation, hence both velocity and concentration perturbations may be important. This definition is identical to the norms used by Doumenc *et al.* [21] and Tilton *et al.* [107].

Figure 2.10 compares the modal contribution of the perturbation magnitude, $E_l^{\mathcal{E}}$ and E_l^{Ω}, for various values of k_p when $a_p = 0.1$ at $t = 1$. Figure 2.10 shows that perturbations consist of harmonics in the form of $nk_p \pm k_d$, where n takes integer values and k_d represents the dominant mode of perturbations which is defined as the mode with the maximum value of E_l^p. For $k_p = 1$, the excited modes occur close to k_d. On the other hand, for higher values of k_p, harmonics are located farther away from k_d. Such modes are unable to draw upon the dominant mode for their

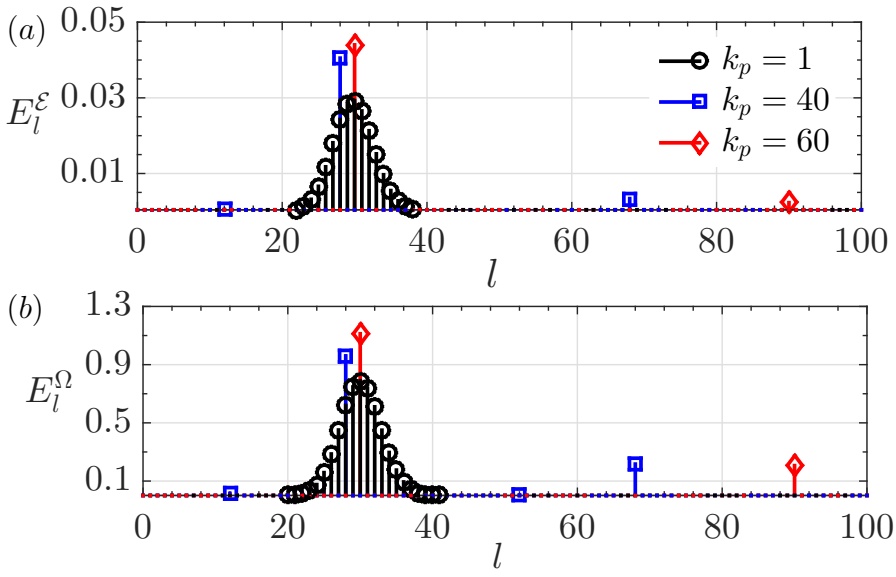

Figure 2.10: The magnitude of horizontal Fourier modes obtained by EVP for $k_p = 1, 40$ and 60 when $a_p = 0.1$ at $t = 1$. (a) $E_l^{\mathcal{E}}$, (b) E_l^{Ω}. The spectrum of perturbed modes is distributed according to $nk_p \pm k_d$.

sustenance and are thereby substantially diminished. The instantaneous dominant growth rate, σ_{max}, is proportional to the sum of all modal energies. Therefore, the maximum value of σ_{max}, occurs at $k_p = 1$ and diminishes for larger values of k_p, as shown in Figs. 2.5 and 2.7.

For the case of $a_p = 0.1$ and $t = 1$ considered in Fig. 2.10, $k_{res} = 60$ (see Fig. 2.7(b)), which is related to the dominant mode according to, $k_{res} = 2k_d$. Examining this relationship for various levels of permeability contrast and time reveals that one sufficient condition for resonant amplification is that the permeability wavenumber coincides with the second harmonic of the dominant mode of perturbation. Further, Fig. 2.10 shows that the maximum modal energy corresponding to the dominant mode occurs when $k_p = 60$. With an increase in heterogeneity, the maximum modal energy is significantly larger for $k_p = 1$ because thick layer with high heterogeneity

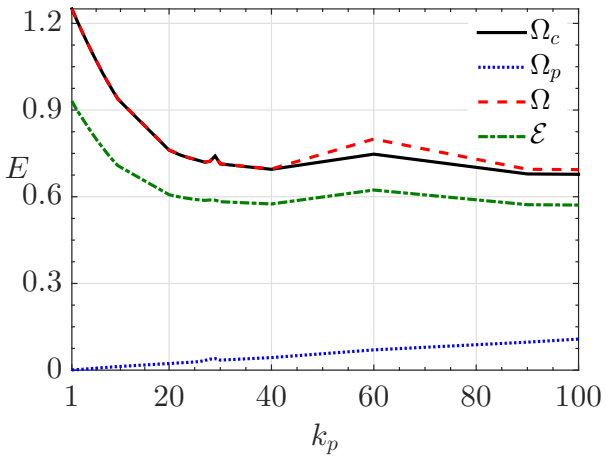

Figure 2.11: (color online) The total magnitude of energy content for E^{Ω_c} , E^{Ω_p}, E^{Ω}, and $E^{\mathcal{E}}$ obtained by EVP when $a_p = 0.1$ at $t = 1$. The corresponding total energy content of E^{Ω_c} and $E^{\mathcal{E}}$ are nearly identical.

are more unstable, as shown in Fig. 2.6. Moreover, the spectrum of permeability induced modes containing 99% of the perturbation energy expands with increasing permeability contrast, a_p.

Figure 2.11 illustrates the total energy content of net vorticity perturbation, E^{Ω}, along with the individual contributions Ω_c, Ω_p and $E^{\mathcal{E}}$ as defined in Eq. 3.29. Figure 2.11 shows that E^{Ω_p} increases with an increase in k_p, but is significantly smaller than E^{Ω_c}. Hence the production of vorticity in the linear regime is primarily due to the misalignment of the concentration gradient with the gravity vector rather than the misalignment of the permeability gradient with the velocity vector. The value of E^{Ω_c}, as indicated in Fig. 2.11, initially decays with increasing permeability wavenumber, followed by a local maximum at $k_p = 29$ and 60, which are the resonant wavenumbers as shown in Fig. 2.7(b). As illustrated in Fig. 2.11, E^{Ω_c} decays with further increase in k_p. A similar trend is observed for E^{Ω}, and $E^{\mathcal{E}}$.

The characterization of instability in this section has been carried out using a 2-D eigenvalue problem. Although this approach provides an efficient means for characterizing the dominant mode, it can not associate the unstable state at any given time with a specific initial condition whose evolution can be traced in time until the onset of nonlinear convection. Therefore, in the following section the initial value problem will be employed as a complementary approach for studying the evolution of imposed modes.

2.4 Perturbation evolution in the linear regime

The stability behavior within the linear period preceding the onset of natural convection is governed by small, but finite amplitude, perturbation structures. We examine the evolution of such perturbations using the IVP method. The IVP approach allows a more clear identification of the factors that influence the evolution of imposed modes at some initial time. This information provides an effective framework for characterizing the transition of linearized perturbations to the nonlinear regime.

The IVP method, as discussed in Sec. 3.2.1, requires an initial condition to solve the perturbed equations. The effect of initial condition on the instability characteristics of a vertically-layered system is presented in Appendix 2.A. In the current study, as demonstrated in detail in Appendix 2.A, we use the "dominant mode" of Ben *et al.* and Riaz *et al.* [86] as the appropriate initial condition. In Appendix 2.B we examine how closely the EVP results match those obtained with

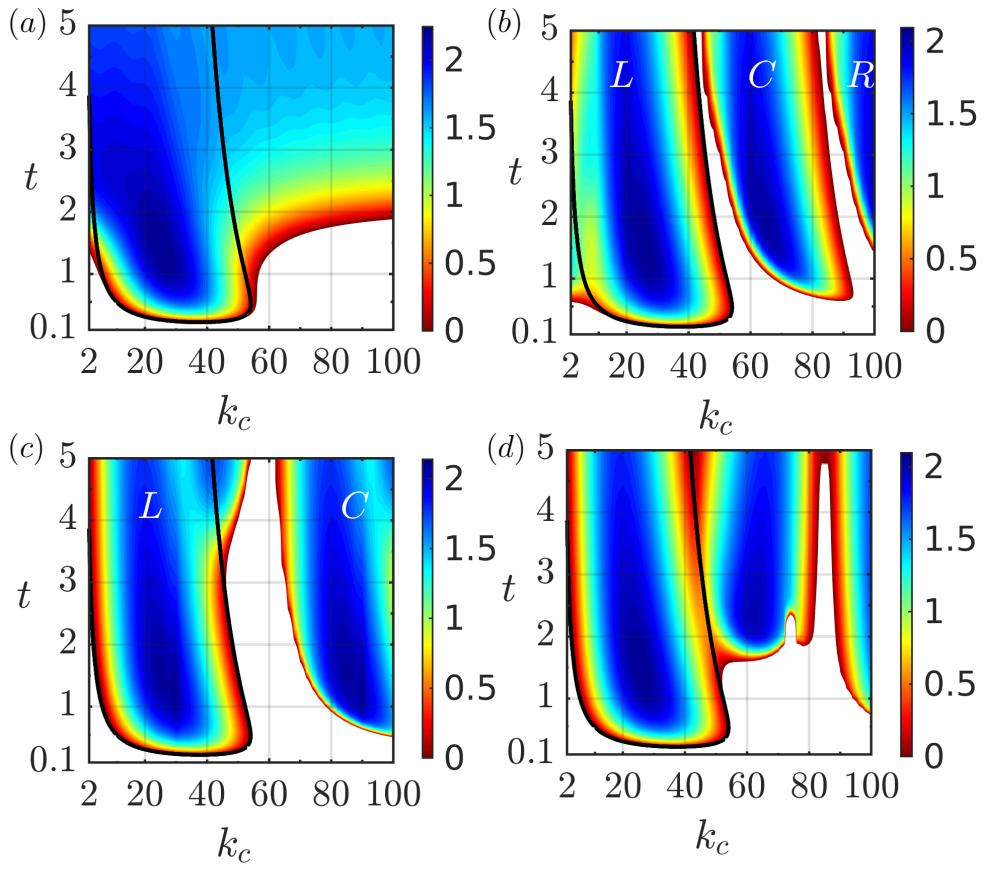

Figure 2.12: The neutral stability curve in (k_c, t) plane obtained by IVP when $a_p = 0.1$, $Ra = 500$, and $t_p = 0.05$. (a) $k_p = 10$, (b) $k_p = 40$, (c) $k_p = 60$, and (d) $k_p = 85$. The solid line represents the neutral stability curve of the homogeneous system. The neutral stability curve splits into multiple unstable zones with an increase in k_p.

the IVP method.

2.4.1 Effect of correlation length and permeability amplitude

Figure 2.12 shows the effect of k_p on the neutral stability curve, which depicts the stable and unstable regions in $k_c - t$ space, when $a_p = 0.1$. The black line indicates the homogeneous case. A small value of $k_p = 10$ extends the zone of unstable modes beyond the homogeneous case to larger values of k_c, as shown in

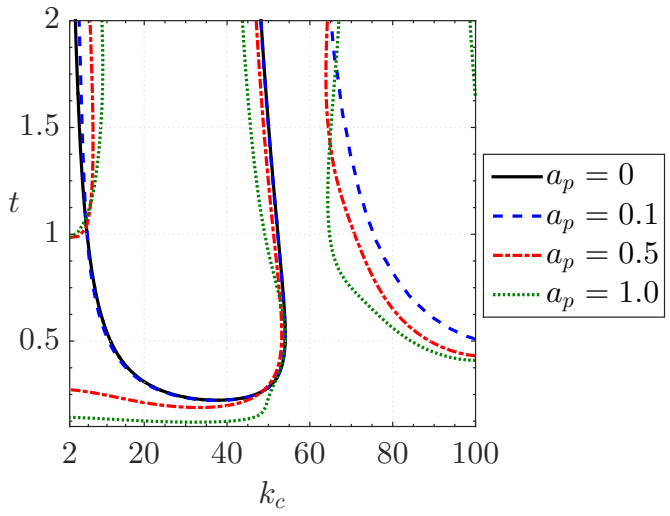

Figure 2.13: The neutral stability curve in (k_c, t) plane obtained with IVP for various values of permeability contrast when $k_p = 55$, $Ra = 500$, and $t_p = 0.05$. The onset time of instability occurs more readily with increasing permeability contrast for thick layers.

Fig. 2.12(a). For a larger value of $k_p = 40$, the neutral stability curve splits into three unstable horizontal regions, as shown in Fig. 2.12(b). These three unstable regions are indicated as the left branch, L, the middle branch, M, and the right branch, R, in Fig. 2.12(b). The right and middle branches develops their own local minima for the critical time of instability. While the bandwidth of the unstable modes shrinks substantially from left to right, the onset time of instability decreases for $k_c > 60$, compared to $k_p = 10$. With a further increase in the permeability wavenumber to $k_p = 60$, the region R vanishes and the gap between regions L and C increases, as shown in Fig. 2.12(c). The region L becomes wider at later times, compared to $k_p = 40$, shown in Fig. 2.12 (b). Another restructuring of the unstable regions is observed at $k_p = 85$ as shown in Fig. 2.12(d).

Figure 2.13*(a)* shows the effect of permeability contrast on the neutral sta-

bility curve when $k_p = 55$. The onset time of instability occurs more readily with increasing a_p. The neutral stability curve splits into two horizontal regions, similar to Fig. 2.12. For a lower value of a_p, the left branch of the neutral stability curve overlaps with the homogeneous case, while the zone of unstable modes expands with increasing permeability contrast, a_p. Similarly, the right branch of the neutral stability curve becomes wider as shown in Fig. 2.13. It should be noted that for larger k_p, the onset time of instability is delayed with increasing permeability amplitude because thin layer with high heterogeneity are less unstable. In the case of $k_p = 40$, shown in 2.13*(b)*, the onset of instability is delayed when k_c commensurates with subharmonic and harmonic modes of k_p. For example, when $a_p = 1$ and $k_p = 40$, the onset of instability is delayed for $k_c = 20, 40, 60$, and 80. This mode interaction becomes more pronounced with increasing permeability contrast. This behavior is due to combined effect of the spectrum of permeability induced modes and their corresponding perturbation energy, as described next.

The splitting of the neutral stability curve into multiple regions, as shown in Figs. 2.12 and 2.13, implies that the growth rate must vary in an oscillatory manner as a function of the imposed perturbation mode, k_c. To explore this behavior, Fig. 2.14(a) compares σ versus k_c at two levels of permeability contrast for $k_p = 30$ and 60 when $t = 1$. As illustrated in Fig. 2.14(a), σ exhibits an oscillatory behavior when permeability heterogeneity is introduced. While this is the common theme among the computed values of σ for the parameters considered here, there is a distinct difference between the decay rate of oscillation, the value of σ at $k_c = 30$ and its higher harmonic, as well as the bandwidth of unstable modes. In the case

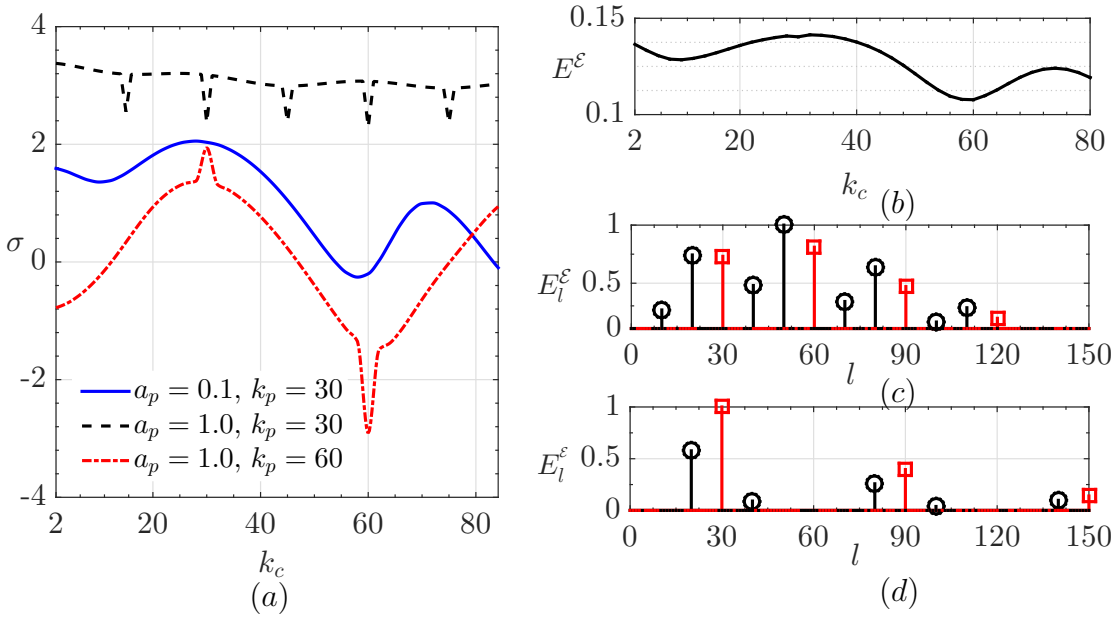

Figure 2.14: The IVP result at $t = 1$ when $Ra = 500$ and $t_p = 0.05$. (a) Comparison of σ vs k_c for $k_p = 30$ with $a_p = 0.1$ and $a_p = 1$, and $k_p = 60$ with $a_p = 1$, (b) The total magnitude of energy content for $a_p = 0.1$ with $k_p = 30$, (c-d) The magnitude of horizontal Fourier modes, defined in Eq. 3.22, for $k_p = 30$ and 60 respectively when $a_p = 1$. Symbols represent: $k_c = 20$ (circles) and $k_c = 30$ (squares). σ versus k_c displays an oscillatory behavior. Sudden changes occur when k_c coincides with k_p or its harmonics.

of $k_p = 30$ and $a_p = 0.1$, the maximum value of σ occurs at $k_c = 30$ and the lowest at $k_c = 60$. The corresponding value of $E_l^{\mathcal{E}}$ shown in Fig. 2.14(b) shows a similar trend, indicating σ to be correlated with the spectral content of the horizontal perturbation. That is the reduced instability due to a lower modal energy manifests itself to smaller growth rate.

Figure 2.14(a) shows that when a_p is increased to 1 while holding k_p fixed at 30, σ jumps, as expected, to higher values that are relatively uniform across k_c expect for the dips when k_c coincides with the harmonic and subharmonic components of the permeability wavenumber, i.e. $k_c = 15, 30, 45, 60$ and 75. For $k_p = 30$, Fig. 2.14(a) shows that compared to $a_p = 0.1$, σ decays at a much smaller rate when

$a_p = 1$. The lowest values of σ occur when k_p is increased to 60 while holding a_p constant at 1. The oscillations are of greater magnitude compared to those for $k_p = 30$. There is also a dip again at $k_c = 60$ but a spike instead at $k_c = 30$. The spikes and dips thus occur when k_c coincides with either the harmonic or the subharmonic of the permeability wavenumber. This behavior can be understood by considering the energy associated with the spectrum of permeability induced modes.

Figure 2.14(c) compares the perturbation energy, defined in Eq. 3.22, contained in the first 150 horizontal Fourier modes for $k_c = 20$ and 30 when $a_p = 1$ and $k_p = 30$. It can be observed that the spectrum for $k_c = 20$ contains more energy (a higher number of modes with larger magnitude) compared to $k_c = 30$, leading to a higher growth rate. The question as to why fewer modes are induced when $k_c = 30$, can be answered by considering the corresponding vorticity contours in Fig. 2.15(a) which shows that for $k_c = 30$ vorticity pairs are less symmetric than those for $k_c = 20$ in plot 2.15(a), hence less favorable for growth. At $k_c = 40$ (not shown), the spectrum and the vorticity contours revert to $k_c = 20$ format and the dip disappears.

In order to now understand the spike at k_c when $k_p = 60$ and $a_p = 1$, as shown in Fig. 2.14(a), we again consider the corresponding modal energy in Fig. 2.14(d). In this case however, $k_c = 30$, with maximum $E_l^{\mathcal{E}}$ among other permeability induced modes, is the dominant mode that undergoes a resonant amplification . As discussed in Sec. 2.3.2, a resonant amplification occurs when the permeability wavenumber coincides with the second harmonic of the dominant mode of perturbation. This condition provides a mechanism for an optimal interaction of perturbations with

the permeability heterogeneity, hence result in a jump in the perturbation growth. The corresponding vorticity contours in Fig. 2.15(b) show that symmetrical vorticity pairs are now associated with $k_c = 30$. Additionally, Fig. 2.14(c-d) show the Fourier component of the permeability induced modes consists of harmonics in the form of $k_c \pm nk_p$ which is also consistent with the results obtained from 2D-EVP approach.

2.4.2 Evolution of the dominant mode

We now investigate the path of the dominant mode to examine the instability characteristics that might trigger the onset of convection. The dominant mode is defined as the wavenumber of disturbances corresponding to the maximum instantaneous growth rate, k^*_σ, or the maximum amplification, k^*_ϕ, in the following form,

$$\sigma^*(t) = \max_{0 \le k_c \le \infty} \left\{ \sigma(t; k_c) \right\} \qquad \text{and} \qquad \Phi^*(t) = \max_{0 \le k_c \le \infty} \left\{ \Phi(t; k_c) \right\} \tag{2.22}$$

The dominant mode based on amplification, k^*_ϕ, is not necessarily the same as the one based on the growth rate because k^*_ϕ represents the cumulative effect of the instantaneous growth rates that change in time. The path of the dominant mode helps shed more light on the resonance phenomenon described in Sec. 2.3.2.

Figure 2.16(a) shows the time evolution of k^*_σ for various values of k_p when $a_p = 0.1$ and $Ra = 500$. After an initial period of smooth decay, k_p drops suddenly to $k^*_\sigma = 30$ around $t = 0.5$ when $k_p = 60$. Subsequently, k^*_σ remains locked over a period of time at the wavenumber of resonance, $k_p = 2k^*_\sigma = 60$. This resonance

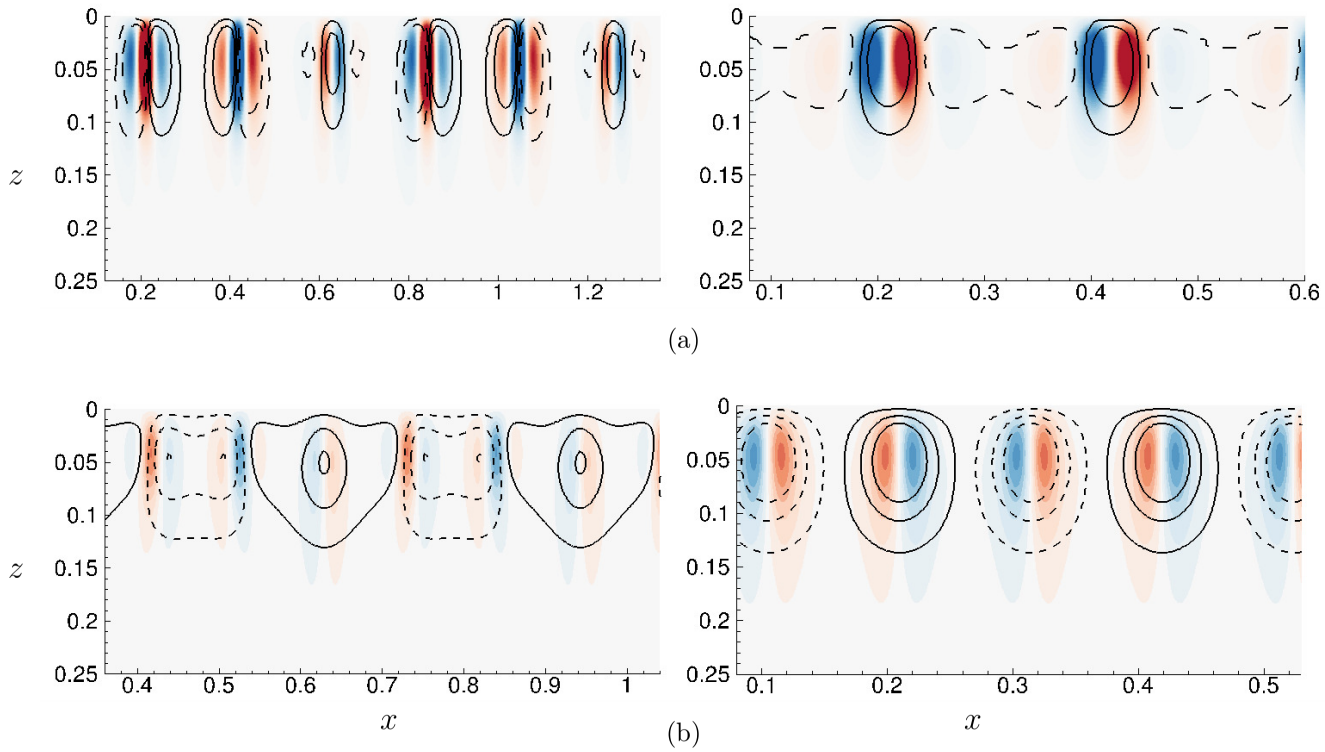

Figure 2.15: Comparison of vorticity contour overlaid with concentration perturbation, $\tilde{c}$ (see Eq. 2.6), obtained by IVP for $k_c = 20$ (left panel) and $k_c = 30$ (right panel) at $t = 1$ when $a_p = 1$, $Ra = 500$, and $t_p = 0.05$. (a) $k_p = 30$, (b) $k_p = 60$. Red and blue indicate positive and negative vorticity pairs.

condition, $k_p = 2k_\sigma^*$, was described in Sec. 2.3.2. A similar behavior occurs when $k_p = 2k_\sigma^* = 40$ over the time period, $2.25 < t < 5$, as shown in Fig. 2.16(a), when mode locking occurs over a longer period of time. Figure 2.16(b) shows that such mode locking phenomena are associated with resonant amplification, e.g., at $t = 1.0$ for $k_p = 2k_\sigma^* = 60$ and at $t = 2.5$ and 3.5 when $k_p = 2k_\sigma^* = 40$. That is the dominant growth rate undergoes a resonant amplification over the a time period during which the permeability wavenumber is equivalent to the second harmonic of the dominant mode. This is consistent with the EVP results discussed in Sec. 2.3.2. In addition to the resonant amplification associated with $k_p = 2k_\sigma^*$, Fig. 2.16(b) indicates the occurrence of another, milder form of amplification around $k_p = 55$ and 50 at $t = 2.5$ and 3.0, respectively. This form of amplification is associated with $k_\sigma^* = k_p - k_c$, such that any imposed mode, k_c, that satisfies this condition will lead to a local excitation in the growth rate. Interestingly, k_σ^* of the milder resonance coincides with that of the homogeneous system. A similar behavior was reported for viscous fingering in heterogeneous media by De Wit and Homsy [18]. Figure 2.16(a)-(b) suggests the existence of two regimes for the resonance amplification that can be summarized as follow:

$$k_{res} = k_p \quad \text{when} \quad k_p = 2k_\sigma^* \quad \text{or} \quad k_\sigma^* = k_h^* \tag{2.23}$$

where k_h^* represent the dominant wavenumber of the homogeneous system.

Figure 2.16(c) shows how resonance influences the dominant mode based on amplification, k_ϕ^*, when $k_p = 60$. Initially, the difference between the value of k_ϕ^*

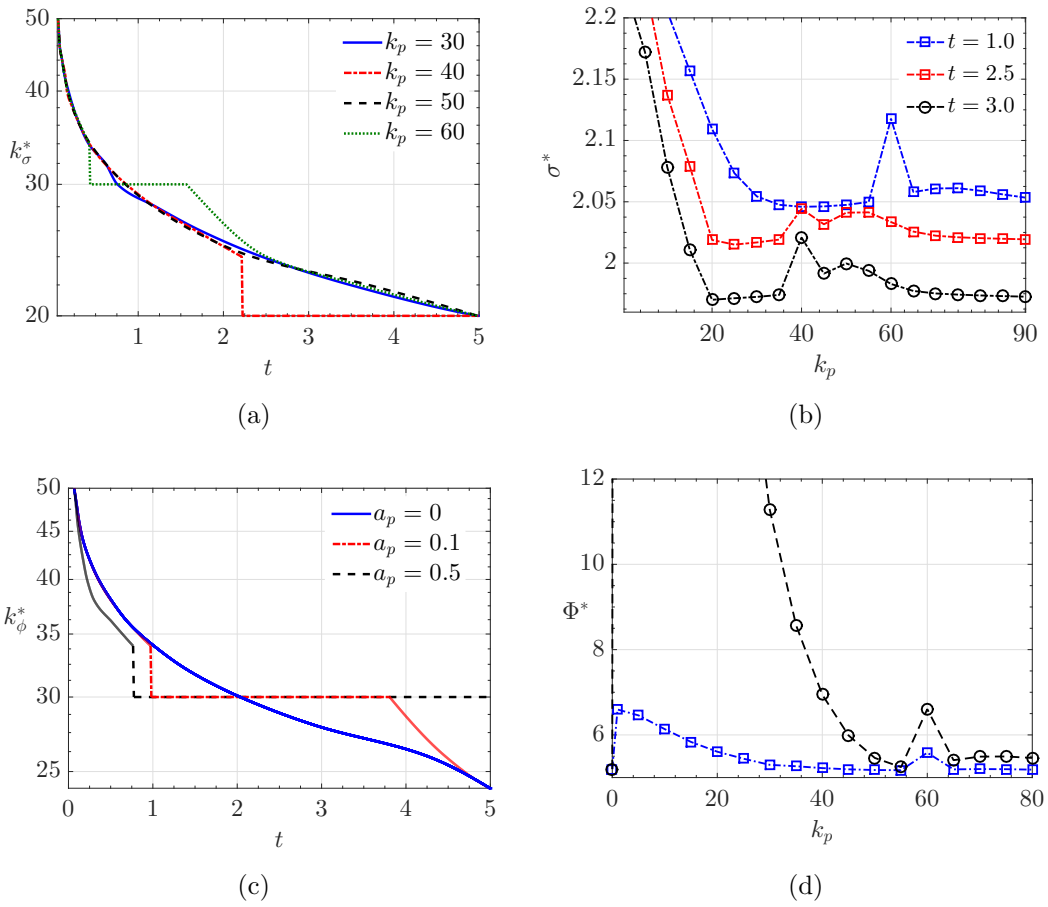

Figure 2.16: (a) Time evolution of k_σ^* for various values of k_p when $a_p = 0.1$, (b) Comparison of the dominant growth rate for $a_p = 0.1$ at various times. A resonant amplification occurs when $k_p = 2k_\sigma^*$. A milder amplification occurs when k_σ^* of the heterogeneous system coincides with that of the homogeneous system, (c) Time evolution of k_ϕ^* for various values of a_p when $k_p = 60$, (d) Comparison of the dominant amplification for $a_p = 0.1$ (squares) and $a_p = 0.5$ (circles) at $t = 1.5$. k_ϕ^* remains locked at the resonant mode, $k_p/2$, over a longer period of time.

corresponding to the homogeneous and heterogeneous system is negligible. After an initial time period, an increase in permeability amplitude results in smaller values of k_ϕ^* compared to their homogeneous counterpart, followed by the mode locking phenomenon according to $k_p = 2k_\phi^* = 60$ for both $a_p = 0.1$ and $a_p = 0.5$. Comparison of k_ϕ^* with k_σ^* in Fig. 2.16(a) for $k_p = 60$ indicates that mode locking occurs for k_ϕ^* over a much longer period of time. The duration of locking, as shown in Fig.

2.16(c), is longer in the case of greater heterogeneity. In the case of $a_p = 0.1$, k^*_ϕ decays at about the same rate as the homogeneous system at late times, while k^*_ϕ remains unchanged for $a_p = 0.5$

The phenomenon of resonant amplification at certain modes and over certain periods of time, as indicated by Figure 2.16, is expected to influence the onset time of nonlinear convection. Moreover, the fact that the values of k^*_σ and k^*_ϕ associated with resonance do not always coincide, can also play a role. These considerations will be discussed next in Sec. 2.5.

2.5 Onset of natural convection

Natural convection of CO_2 in porous media is generally associated with a rapid dissolution flux of CO_2, induced by gravitationally unstable plumes. The dissolution flux is governed by the concentration gradient at the interface and may be expressed as,

$$\mathcal{J}(t) = \frac{1}{L}\int_0^L \frac{1}{Ra}\frac{\partial c}{\partial z}\Big|_{z=0} dx \tag{2.24}$$

where L is the domain width and the definition of Ra is provided in Sec. 3.2.1. The onset time of convection initiates a period of accelerated dissolution of CO_2 as a result of the continuous growth of disturbances. We define the onset time of convection as the time when the dissolution flux switches from negative to positive growth rate, i.e. $d\mathcal{J}/dt = 0$. In the following, we examine the critical conditions for the onset time of convection in heterogeneous media and its connection to the linear regime via the path of the dominant mode. We also explore the effect of resonant

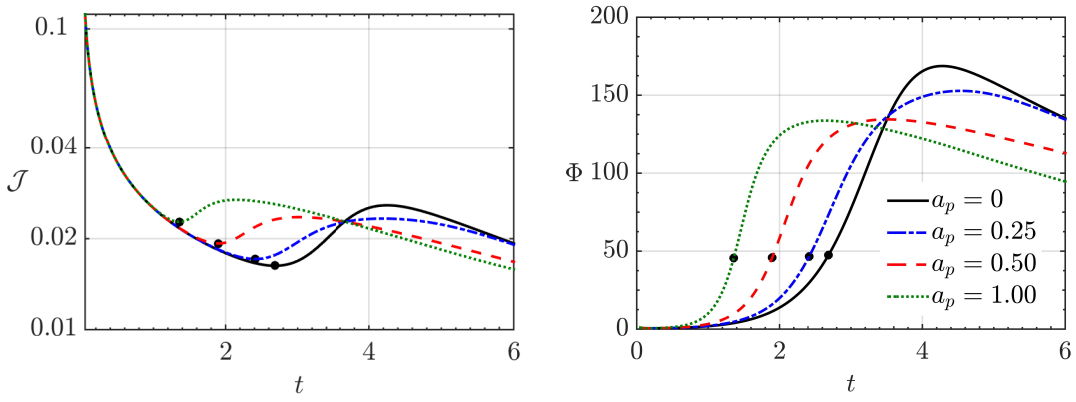

Figure 2.17: DNS result when $\epsilon = 0.01$, $k_p = 1$, $k_c = 30$, and $Ra = 500$ for various values of permeability contrast, a_p. (a) Time evolution of dissolution flux, (b) Corresponding time evolution of amplification. The solid dot marks the onset time of convection. The onset time of convection shifts to an earlier time with increasing permeability contrast, a_p.

amplification on the onset time of convection.

We perform two-dimensional direct numerical simulation (DNS) of the non-linear governing equations, Eq. 3.1–2.2, using high-order pseudospectral method [86, 106]. Perturbations are introduced in the form of small amplitude disturbances on the initial concentration field at $t = t_p$ as,

$$c(x, z) = c_b(z) + \epsilon c_p(z) cos(k_c x), \tag{2.25}$$

where c_p is the vertical shape function that we take to be $\mathcal{G}(\xi)$, as defined in Appendix A, ϵ is the perturbation amplitude, and k_c is the perturbation wavenumber. The initial time of perturbation is set to $t_p = 0.05$ which is an order of magnitude smaller than the critical onset time of instability, discussed in Sec. 2.3.

Figure 2.17(a) shows the time evolution of the dissolution flux for various val-

ues of permeability amplitude, when $\epsilon = 0.01$, $k_p = 1$, $k_c = 30$, and $Ra = 500$. The flux, as shown in Fig. 2.17(a), initially experiences a decay due to dominance of diffusion, followed by a linear growth regime at the onset of convection, t_{cv}. The onset time of convection, marked as solid dots in Fig. 2.17(a), occurs at an earlier time with increasing permeability amplitude for low permeability wavenumber considered in this figure. The corresponding time evolution of amplification is shown in Fig. 2.17(b). Interestingly, the threshold value of amplification required to induce convection, indicated with dots, is similar for the range of permeability contrasts shown in this figure, including the one for the homogeneous media. This suggests that amplification is an appropriate indicator of the onset time of convection.

2.5.1 Effect of permeability structure

The onset time of convection, t_{cv}, computed with DNS for various values of a_p when $k_p = 30$, $\epsilon = 10^{-2}$, and $Ra = 500$ is shown in Fig. 2.18 as a function of k_c. Figure 2.18(a) shows that all perturbation wavenumbers lead to onset in the case of heterogeneous media. In contrast, convection does not occur for larger wavenumbers in a homogeneous medium because the amplification required for transitioning to nonlinear growth is not achieved by the larger imposed modes. Consequently, these large wavenumbers are quickly damped. The corresponding values of the amplification, Φ^*, needed to trigger convection, as noted in the figure, are independent of k_c. As expected, t_{cv} decreases with an increase in a_p and also experiences a jump when k_c is equal to the harmonic and sub-harmonic components of k_p. Such delays

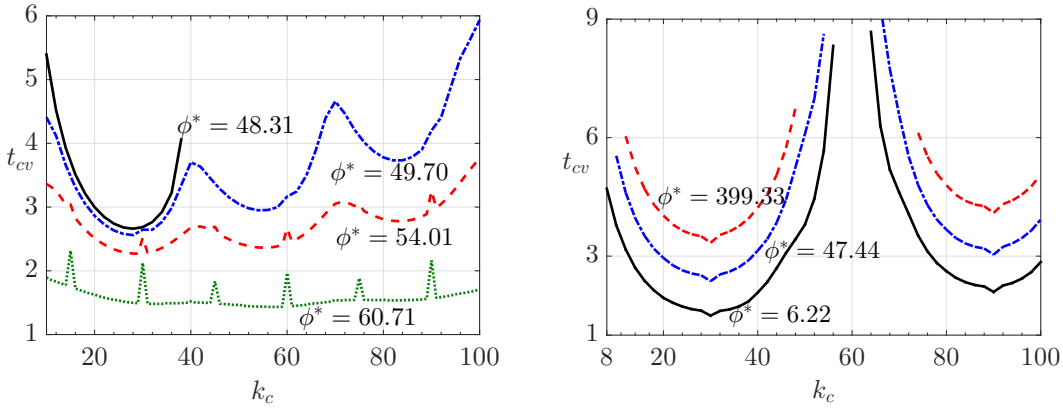

Figure 2.18: (a) The onset time of convection vs k_c for $a_p = 0$ (solid line), $a_p = 0.25$ (dash-dotted line), $a_p = 0.5$ (dashed line), and $a_p = 1$ (dotted line) when $\epsilon = 0.01$, $k_p = 30$, and $Ra = 500$, (b) The onset time of convection vs k_c for $\epsilon = 0.001$ (dashed line), $\epsilon = 0.01$ (dash-dotted line), and $\epsilon = 0.1$ (solid line) when $k_p = 60$, $a_p = 0.5$, and $Ra = 500$. The onset of convection is influenced substantially by different permeability fields.

in the onset time are associated with the damping associated with these value of k_c, as shown in Fig. 2.14. The influence of ϵ on t_{cv} is plotted in Fig. 2.18(b) for a larger value of permeability wavenumber $k_p = 60$ when $a_p = 0.5$ and $Ra = 500$. As expected, t_{cv} drops with an increase in ϵ. Moreover, because perturbations with larger ϵ require less amplification to trigger onset, Φ^* also decreases with increasing ϵ. The influence of resonant amplification on t_{cv} when $k_c = k_p/2$ is observed as a relatively small dip at $k_c = 30$ in the onset time in all cases. Figure 2.18(b) further shows that the onset curve splits into two branches as a consequence of a similar branching of the neutral stability curve shown in Fig. 2.12. The bandwidth of wavenumbers that undergo convection expands for larger values of ϵ in both branches because more imposed modes now can achieve the lowered threshold for convection associated with larger values of ϵ.

The onset time of instability and convection as suggested in Figs. 2.12 and 2.18, respectively, depend on the permeability structure as well as perturbation parameters. The comparison of these two onset events indicates that while the overall trends in instability behavior with varying perturbation wavenumber are similar, an early onset time of instability may not always translate to an early onset time of convection. A comparison of the onset time of instability and convection for $a_p = 1$ and $k_p = 30$ in Fig. 2.19(a) indicates that while the onset time of instability is slightly smaller for $k_c = 60$ compared with $k_c = 40$, the dotted green curve in Fig. 2.18(a) shows that t_{cv} exhibits an opposite trend. In order to examine this behavior, we plot the time history of amplification for both values of k_c in Fig. 2.19(b), which indicates that initially the amplification is larger for $k_c = 60$, but beyond a crossover point Φ becomes greater when $k_c = 40$. Thus, the threshold amplification required to trigger the convection onset is attained earlier when $k_c = 40$.

In order to better understand the difference between the rates of amplification in these two cases at various times, we calculate the magnitude of the perturbation energy contained in each horizontal Fourier mode according to Eq. 3.22. Figure 2.19(c) shows that the modal energy content of the dominant mode for both $k_c = 40$ and 60 is approximately equal prior to the onset time of instability, i.e. $t = 0.12$. On the other hand, at $t = 1.5$ the perturbation spectrum of $k_c = 40$ contains more permeability induced modes with higher magnitude compared with $k_c = 60$. The introduction of the new set of excited modes is associated with the twisting and elongation of vorticity pairs as shown in Fig. 2.20(c), which leads to accelerated finger growth and an earlier convection onset. The spectrum and the magnitude

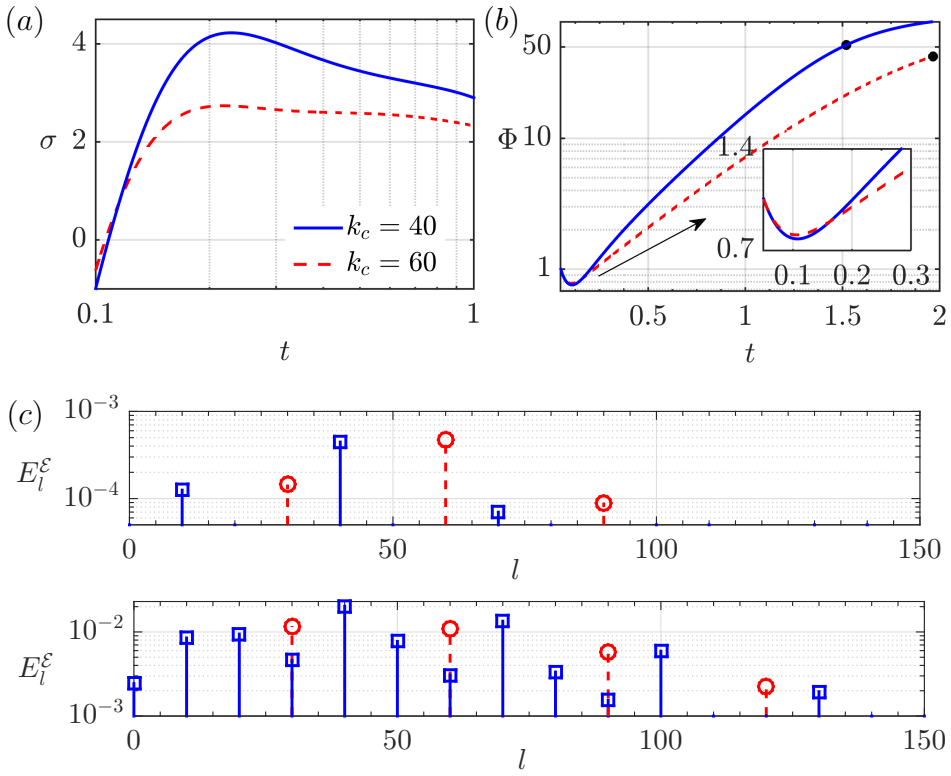

Figure 2.19: DNS results when $\epsilon = 0.01$, $a_p = 1$, $k_p = 30$, and $Ra = 500$. (a-b) Time history of growth rate and amplification, respectively for $k_c = 40$ and 60. The solid dot marks the onset time of convection, and (c) The magnitude of horizontal Fourier components integrated in the direction of gravity at $t = 0.12$ (top panel) and $t = 1.5$ (bottom panel). The symbols represent $k_c = 40$ (squares) and $k_c = 60$ (circles). An earlier onset of instability does not necessarily imply an earlier onset of convection.

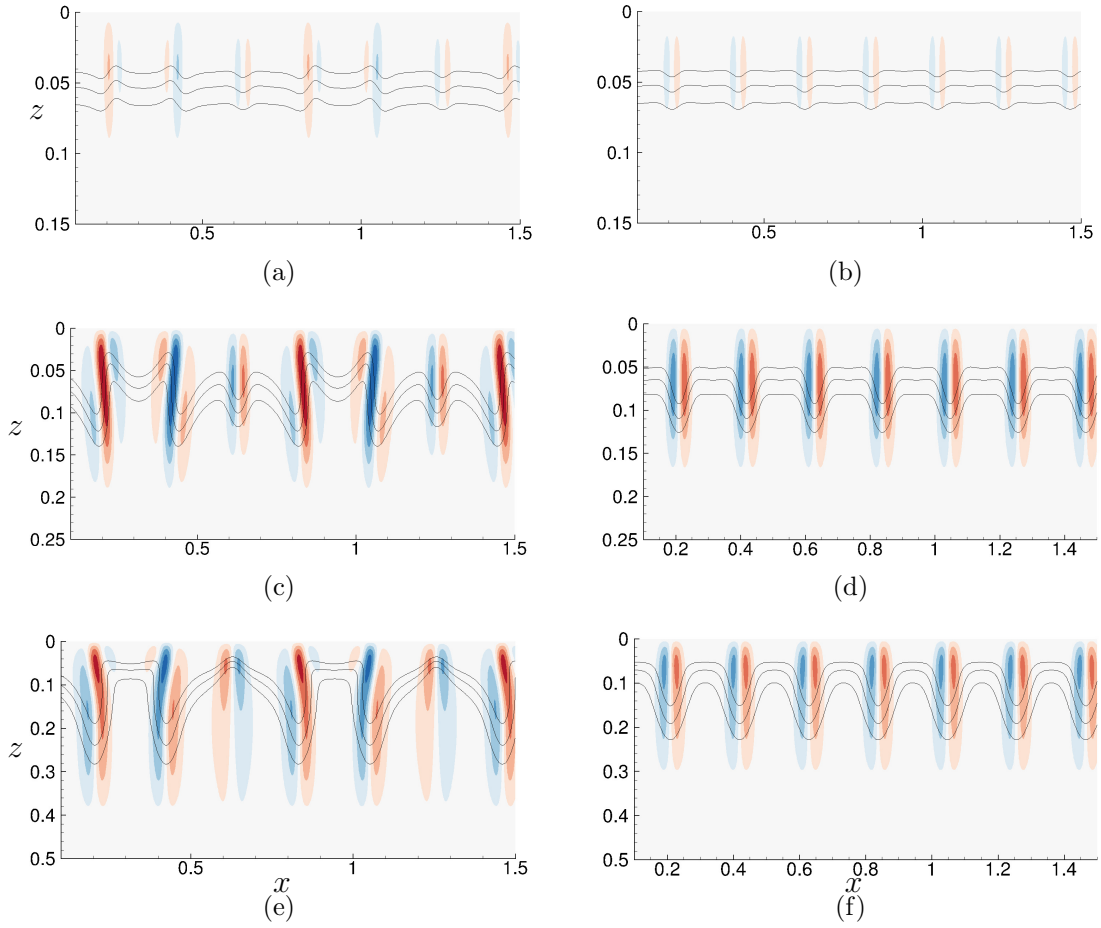

Figure 2.20: Comparison of DNS results for vorticity contour overlaid with concentration field when $\epsilon = 0.01$, $a_p = 1$, $k_p = 30$, and $Ra = 500$. Left and right columns are for $k_c = 40$ and $k_c = 60$, respectively. Rows indicates $t = 0.1, 1.5$ and 3.5, from top to bottom, respectively. Red and blue indicate positive and negative vorticity pairs.

of permeability induced modes are thus both important for generation of faster growing fingers. Figure 2.19(c) shows that the modal component of permeability induced modes prior to the onset time of convection consists of harmonics in the form of $k_c \pm n(k_p - k_c)$, where n takes integer values, which is qualitatively different from the linear regime where modes appear in the form of $k_c \pm nk_p$.

In order to further characterize the interaction between permeability and perturbation modes, we compare the vorticity contours at three time intervals for the

same parameters used for Fig. 2.19. The corresponding concentration field is superimposed on the vorticity field. The vorticity fields, as shown in Fig. 2.20, consist of multiple dipolar structures of positive (red) and negative (blue) vorticity pairs. Initially, while the alignment of the vorticity pairs in Fig. 2.20(a-b) is different, the vorticity strength is quite similar. The difference in vorticity alignment between $k_c = 40$ and 60 stems of course from the variation in the permeability induced modes caused by differences in perturbation wavenumber. After the onset of convection, the vorticity contours of $k_c = 40$ differ substantially from those for $k_c = 60$. Prior to the onset of convection, specific structure of vorticity pairs that is manifested as the channelled distribution of concentration profiles suggests a stronger growth of fingers in the case of $k_c = 40$ which results in an earlier onset time of convection. On the other hand, in the case of $k_c = 60$ while the vorticity pairs gain strength due to the perturbation growth, as shown in Fig. 2.20(d), the concentration profile propagates downward symmetrically, as opposed to the lateral pinch off observed in Fig. 2.20(c) when $k_c = 40$. Additionally, comparison of the rate of frontal deformation of the concentration profile at $t = 1.5$ for both perturbation wavenumber shows a smaller advancement in the case of $k_c = 60$. At later time $t = 3.5$ when the flow is fully nonlinear, Fig. 2.20(e) shows the finger tips to coincide with the dominant vorticity pair, creating a stretched profile at the root. As a result, the fingers tip advances faster compared to $k_c = 60$, shown in Fig. 2.20(f), resulting in more amount of CO_2 being drawn from top boundary. In the case of $k_c = 60$, the wavelength of the convective fingers remain unchanged and have a simpler structure.

2.5.2 Critical onset time of convection

An early onset time of convection is favorable because it initiates a period of accelerated convective mixing. We define the critical onset time of convection as the minimum onset time of convection among all the perturbation wavenumbers for a set of predefined t_p, Ra, and heterogeneity parameters, in the following form,

$$t^*_{cv} = \min_{0 \leq k_c \leq \infty} \left\{ t_{cv}(k_c) \right\} \tag{2.26}$$

Figure 2.21 shows the effect of permeability contrast, a_p, on the critical onset time of convection, t^*_{cv} for $\epsilon = 0.01$ and $Ra = 500$. Three distinct regimes can be observed. Initially, t^*_{cv} shifts to higher values with an increase in permeability wavenumber, followed by a decrease in t^*_{cv} where it attains a local minimum at the resonant wavenumber, $k_p = 60$. Following which, the value of t^*_{cv} increases with increasing permeability wavenumber where it asymptotes to the corresponding homogeneous value for low levels of permeability amplitude. For sufficiently low values of k_p, the permeability amplitude has a strong influence on t^*_{cv}, whereas at higher values of k_p, the variation of t^*_{cv} appears to be relatively small for low levels of permeability contrast. On the other hand, in the case of large a_p the value of t^*_{cv} is significantly larger than the corresponding homogeneous system when the permeability wavenumber is large. As discussed in Sec. 2.3.1, the critical onset time of instability displays a qualitatively similar trend.

In order to examine the effect of heterogeneity on t^*_{cv}, we consider the time

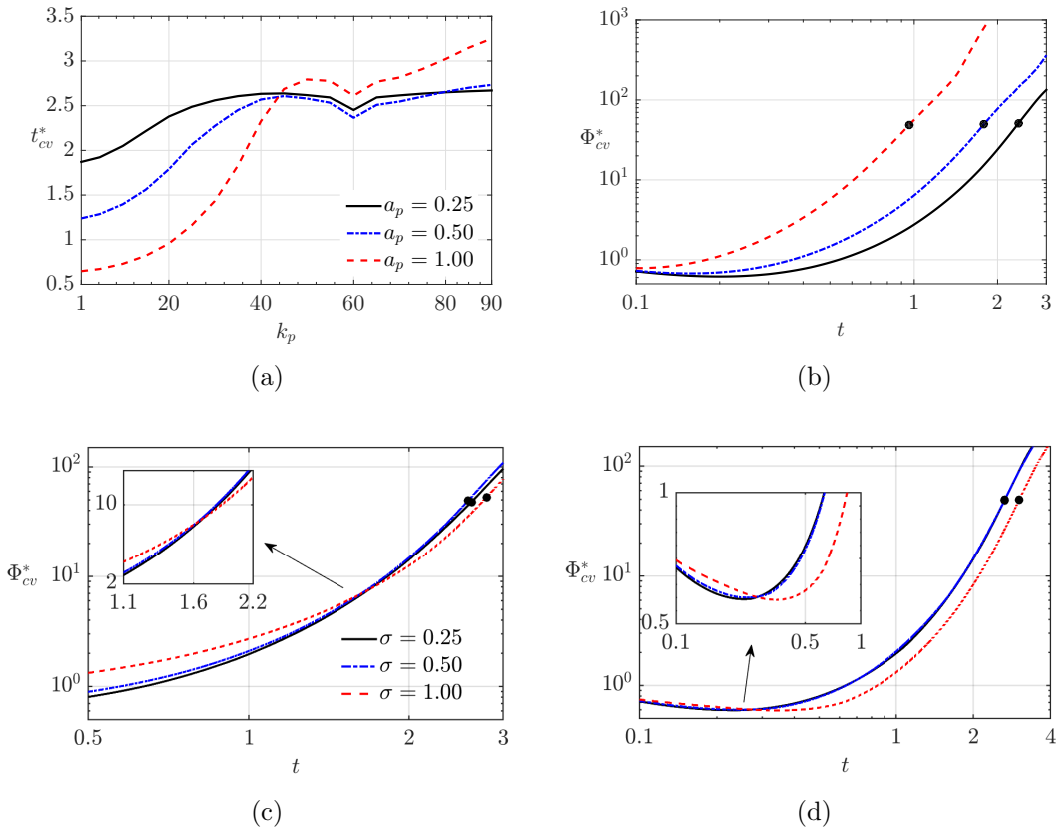

Figure 2.21: (a) The effect of permeability contrast on the critical onset time of convection vs k_p when $\epsilon = 0.01$, and $Ra = 500$. The critical onset time of convection for the homogeneous system is $t^*_{cv} = 2.66$. (b-d) Time evolution of Φ^* for $k_p = 20$, 50, 80, respectively. The critical onset time, t^*_{cv}, experience an abrupt change depending on the permeability length scale and the level of permeability contrast.

evolution of the dominant amplification, Φ^*, shown in Fig. 2.21(b-d). Figure 2.21(b) compares the time evolution of Φ^* for three levels of permeability amplitude, $a_p = 0.25, 0.5$, and 1 when $k_p = 20$, $\epsilon = 0.01$, and $Ra = 500$. The corresponding onset time of convection is marked with dot symbols. This figure reveals that amplification increases systematically with an increase in permeability amplitude. Consequently, the critical value of amplification required to trigger the onset time of convection is attained sooner for higher levels of permeability contrast. Therefore, the onset time of convection occurs earlier with increasing a_p at low permeability wavenumber, as

shown in Fig. 2.21(a). The comparison of temporal evolution of Φ^* for $k_p = 50$ is shown in Fig. 2.21(c). The behavior of Φ^* is quantitatively different from those with low k_p value. Initially, the value of Φ^* is larger for higher a_p, however at $t = 1.65$ the amplification associated with $a_p = 0.1$, as well as $a_p = 0.5$ surpasses Φ^* corresponding to $a_p = 1$. This results in a delayed onset time of convection for intermediate value of k_p when $a_p = 1$, as illustrated in Fig. 2.21(a). A similar situation is observed in the case of larger permeability wavenumber, shown in Fig. 2.21(d) where the point of cross over in $\Phi^*(t)$ occurs at a much earlier time, thus t^*_{cv} is delayed further with increasing permeability contrast for large value of k_p.

2.6 Conclusions

We studied buoyancy driven instability associated with diffusive boundary layers in heterogeneous porous media. In order to develop a basic understanding of the nature of instability in such systems, we used a periodic variation of permeability in the horizontal direction. This setup allows for a systematic assessment of the fundamental physical mechanisms that can help evaluate instability behaviors for more complicated heterogeneity structures.

Two complementary methods of linear stability analysis were used; a 2-D eigenvalue formulation and an initial value problem. The eigenvalue analysis was used to describe the evolution of the preferred mode independently of the mode of initial perturbation. The initial value problem was used to track the evolution of initial modes through the linear regime, up until the onset of convection. Compar-

ison of IVP and 2D-EVP reveals the dominant perturbation growth as well as the critical onset time of instability have similar behavior.

Our study indicates that in contrast to the vertical variation of permeability, linear perturbations associated with horizontal permeability variation are multimodal and more closely coupled with heterogeneity. We found that the most unstable flow occurs for the smallest permeability wavenumber of $k_p = 1$. While larger permeability wavenumbers are generally less unstable, the variation in growth rate as a function of permeability wavenumber is not monotonic. The growth rate attains a local maximum over a certain range of wavenumbers. This is due to a resonant excitation of the perturbed mode when the permeability mode coincides with the second harmonic of the dominant perturbation mode. A milder resonance also occurs when the dominant perturbation mode of the heterogeneous media coincides with the corresponding homogeneous system. On the other hand, when the perturbed mode is not dominant, harmonic interactions instead produce the opposite effect of significant damping. A similar behavior was reported for unstable displacement type flows in heterogeneous porous media. Due to the transient nature of the base state, the resonant wavenumber based on dominant growth rate shift systematically towards smaller permeability wavenumber. On the other hand, the resonant wavenumber based on the maximum instantaneous amplification is independent of time. This behavior is due to the cumulative effect of instantaneous growth integrated over a time period.

In this analysis we used a single value of Rayleigh number. Linear stability behavior at other values of Rayleigh number can be obtained by a simple rescaling

using an appropriate characteristic length scale. Prior to the interaction of the boundary layer with the bottom boundary, this type of rescaling is also appropriate for obtaining the convection onset. Additionally, this work is beneficial to other physical systems, e.g. heat transfer devices and various geophysical flows, where natural convection is important and convective mixing is governed by the same conservation laws.

Other than the resonant amplification, the influence of heterogeneity magnitude was found to be generally similar to that of the purely vertical permeability variation. That is, instability was observed to increase with an increase in the magnitude of heterogeneity for thick layers and to decrease with an increase in heterogeneity in the case of thin layers. Moreover, for a large enough heterogeneity magnitude, the corresponding homogeneous case was found to be more unstable than thin layers.

We found that the onset times for both the instability and convection to be particularly sensitive to small changes in heterogeneity. Similar to the critical onset of instability, the critical onset of convection experiences an abrupt change depending on the permeability length scale and the amount of heterogeneity. However, an earlier onset of instability for a given initial mode does not always translate to an early onset time of convection for high levels of heterogeneity. This behavior results from a reorientation of vorticity pairs due to the interaction of time evolving perturbation structures with heterogeneity, favoring growth of perturbation modes that were less amplified at earlier times. The instantaneous contribution of vorticity in such cases depends on both the spectrum and the magnitude of permeability

induced modes. By comparing vorticity and concentration fields, we illustrated how different features of permeability heterogeneity impact different fingering structures.

Linear stability behavior at other values of Rayleigh number can be obtained by a simple rescaling using an appropriate characteristic length scale. Prior to the interaction of the boundary layer with the bottom boundary, this type of rescaling is also appropriate for obtaining the convection onset. Additionally, this work is beneficial to other physical systems, e.g. heat transfer devices and various geophysical flows, where natural convection is important and convective mixing is governed by the same conservation laws.

Appendix 2.A Effect of Initial Condition

The IVP method, as discussed in Sec. 3.2.1, requires an initial condition to solve the perturbed equations. To determine an appropriate initial condition for the IVP analysis (see Eq. 2.10), we consider four initial condition profiles: the "dominant mode" of Riaz *et al.* [86] (c_p^d) shown in Eq. 2.11, a filtered top hat profile (c_p^h), and two Gaussian profiles (c_p^G). As suggested by experimental evidence [11], the perturbation profiles are assumed to be concentrated within the boundary layer and decay to zero beyond the boundary layer thickness. The Gaussian shape function may be expressed as,

$$G_i(z) = \exp\left(-\frac{1}{2}\left(\frac{z-\mu_i}{\sigma_i}\right)^2\right) \qquad \text{for } z \in (0,\delta) \tag{2.27}$$

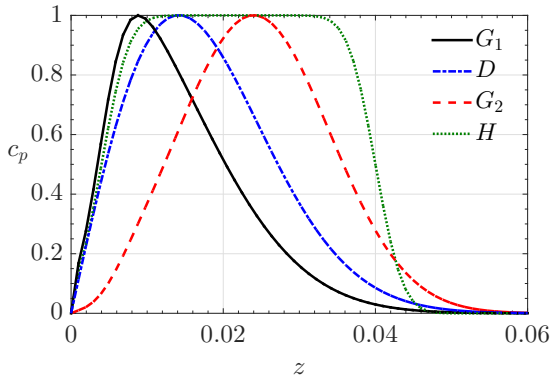

Figure 2.22: The normalized initial perturbation profiles.

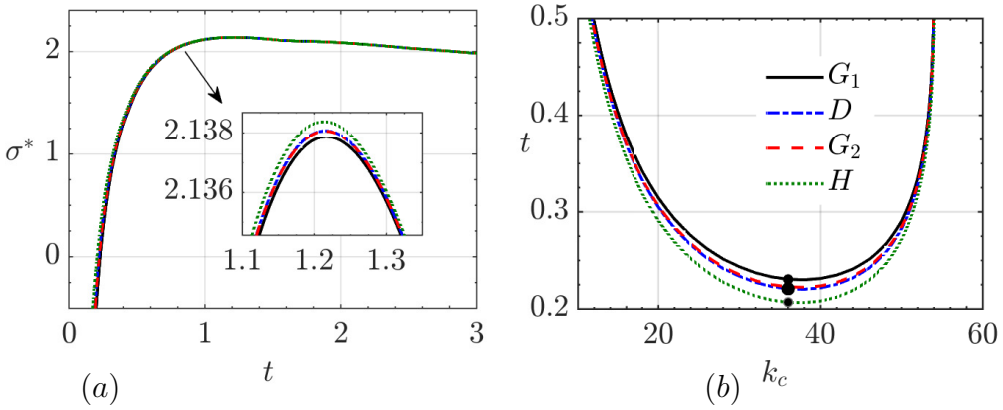

Figure 2.23: IVP results when $a_p = 0.1$, $k_p = 60$, $Ra = 500$, and $t_p = 0.05$ for the prescribed initial perturbation profiles of Fig. 2.22. (a) Comparison of the time evolution of σ^*, (b) The neutral stability curve. The solid dot marks the critical time for the onset of instability.

where δ is the boundary layer depth defined as $c_b(\delta, t_p) = 0.005$, G_i is a Gaussian distribution with the mean and standard deviation of μ_i and σ_i, respectively. We vary the peak location of the Gaussian distribution $\mu_i = (0.05, 0.6)$ and the width $\sigma_i = (0.35, 0.25)$ to create two initial distribution profiles. The value of μ_i are selected such that each one of the Gaussian profiles be concentrated on the left or the right side of the "dominant mode" profile, as shown in Fig. 2.22.

We compute the growth rate for the integer wavenumbers of $8 \leq k_c \leq 60$ when

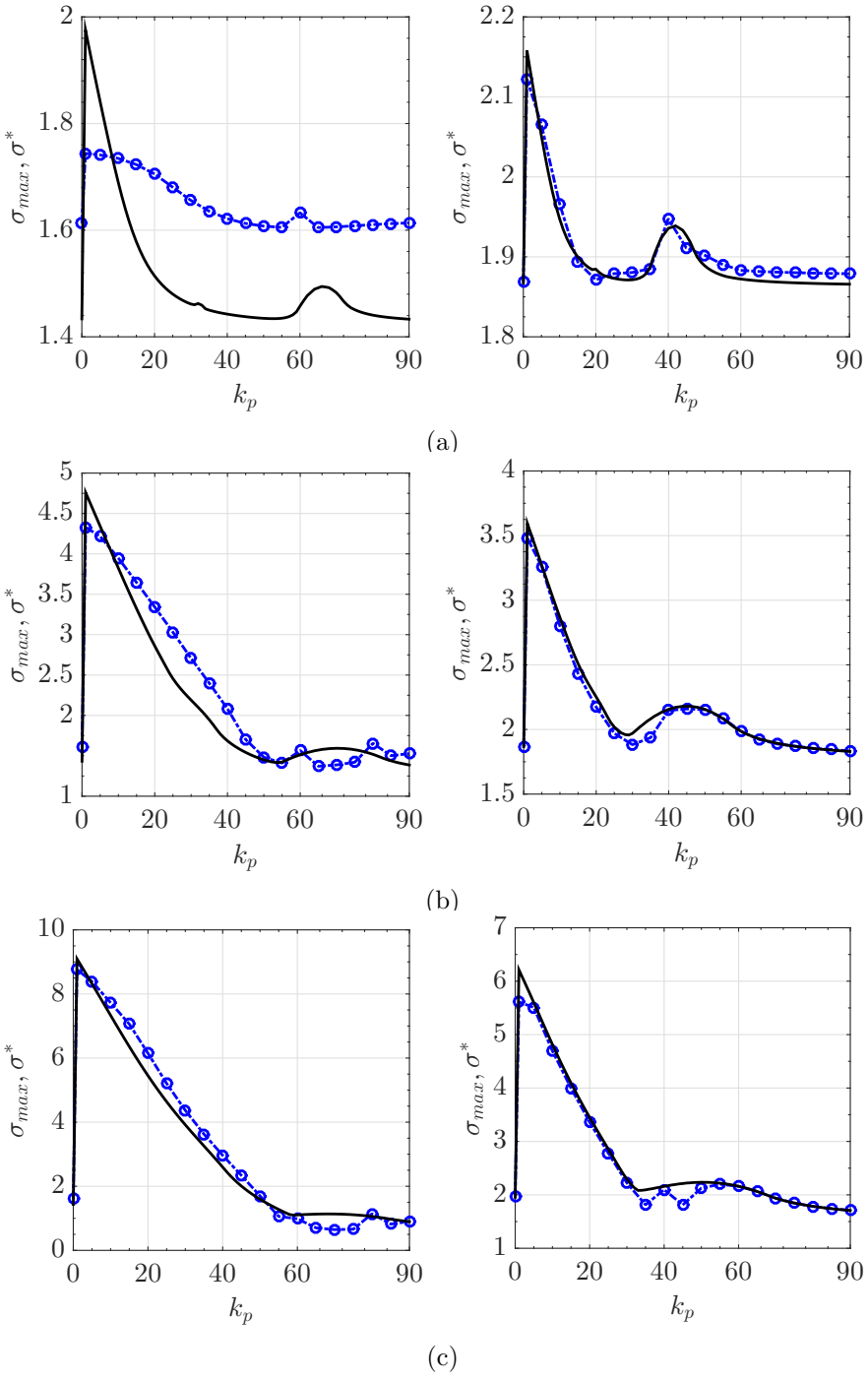

Figure 2.24: Comparison of the IVP dominant growth rate, σ^*, (symbols) with the EVP (solid line) at $t = 0.5$ (left panel), and $t = 3$ (right panel) when $Ra = 500$ and $t_p = 0.05$. (a) $a_p = 0.1$, (b) $a_p = 0.5$, and (c) $a_p = 1$.

$a_p = 0.1$, $k_p = 60$, and $Ra = 500$. The time evolution of the dominant perturbation growth, as shown in Fig. 2.23(a), indicates that while the local extrema of σ^* is slightly different for different initial profiles, the overall features of σ^* remains essentially unchanged. Figure 2.23(b) shows the neutral stability curve, for which $\sigma = 0$, in the (k_c, t) plane for the prescribed initial profiles. The solid dots marks the critical points of the onset of instability,(k_c, t_c). Figure 2.23(b) indicates the qualitative behavior of the neutral stability curve is similar for all initial profiles, and c_p^h corresponds to the earliest onset. However, in the weakly non-linear regime, c_p^h gives rises to non-physical concentration fields when the perturbation amplitude, ϵ, is not small. Thus, we use the "dominant mode" profile, c_p^d, as the initial condition in this work because it handles larger values of ϵ and results in the earliest onset time, compared to the Gaussian profiles.

Appendix 2.B Effectiveness of EVP

In order to compare IVP and EVP analyses, we compute the growth rate for the integer perturbation wavenumber, $2 \leq k_c \leq 100$, and permeability wavenumber, $0 \leq k_p \leq 90$, at three levels of permeability amplitude in the range of $0.1 \leq a_p \leq 1.5$ when $Ra = 500$ and $t_p = 0.05$. Figure 2.24 compares the variation of dominant growth rate with k_p for several levels of permeability contrast obtained by IVP with EVP method at two different times, $t = 0.5$ and 3. Figure 2.24 shows an arguably good agreement between σ^* computed by IVP with σ_{max} obtained by EVP at late time.

Similarly, the predicted resonance wavenumbers are relatively similar for different levels of permeability contrast. On the other hand, while the qualitative features remain the same at early times, there is a quantitative difference in the value of dominant growth rate produced by IVP and EVP. The disagreement in the prediction of dominant growth rate increases with decreasing permeability contrast. The poor agreement at early times is perhaps because the linear stability operator corresponding to diffusive boundary layer is non-autonomous and nonmodal. The non-orthogonality of EVP eigenmodes combined with non-autonomous nature of the linear operator, especially at early time when the diffusive boundary layer experiences a rapid growth, extends the transient period during which the dominant perturbations are not clearly defined. [106]

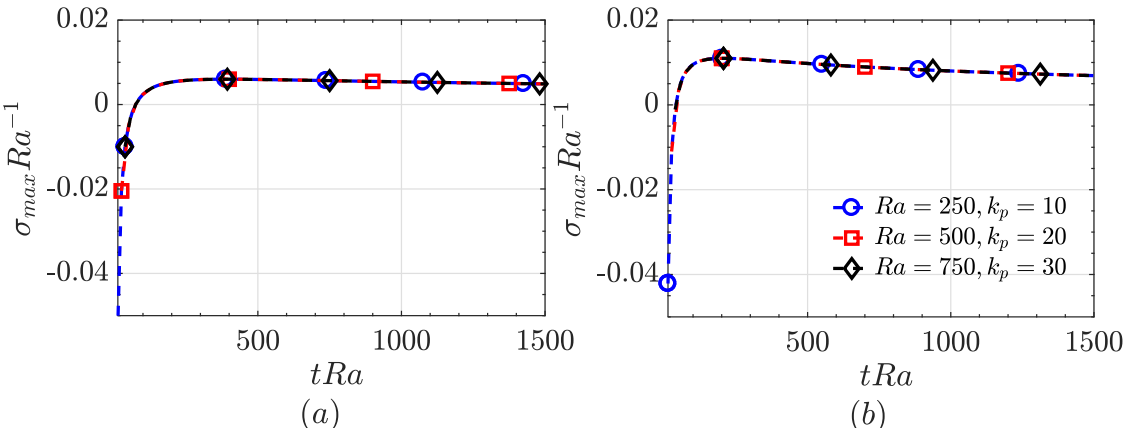

Figure 2.25: $\sigma_{max} Ra^{-1}$ versus tRa for combinations of $Ra = 250$ and $k = 10$ (circles), $Ra = 500$ and $k = 20$ (squares), $Ra = 750$ and $k = 30$ (diamonds) obtained by EVP. (a) $a_p = 0.5$, (b) $a_p = 1.0$.

Appendix 2.C Rayleigh number scaling

To explore the effects of the Rayleigh number, we compute the dominant growth rate, σ_{max}, for various values of permeability wavenumber and heterogeneity contrast when $250 \leq Ra \leq 750$ using 2D-EVP. Figure 2.25 shows $\sigma_{max} Ra^{-1}$ versus tRa for three combinations of $Ra = 250$ and $k_p = 10$, $Ra = 500$ and $k_p = 20$, and $Ra = 750$ and $k_p = 30$ at two levels of permeability amplitude of $a_p = 0.5$ and 1. The results obtained using different combinations of Ra and k_p collapse to a single curve because effect of the bottom boundary is negligible, hence validating the scaling in the linear regime. Similarly, Fig. 2.26 plots $\sigma_{max} Ra^{-1}$ as a function of k_p/Ra for three Ra values when $a_p = 0.1$. Figure 2.26 demonstrates that the three curves collapse to a single curve for various values of the Rayleigh number. Consequently, when the porous layer is approximated as semi-infinite, $H \to \infty$,

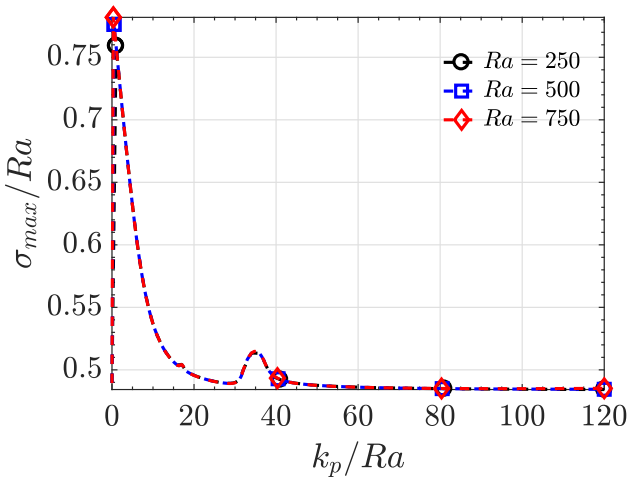

Figure 2.26: $\sigma_{max} Ra^{-1}$ as a function of k_p/Ra for three Ra values when $a_p = 0.1$.

the Rayleigh number can be be scaled out of the governing equations (3.1)–(2.2) by nondimensionalizing the problem with respect to the characteristic length $L =$

$\phi\mathcal{D}/U$ and time $T = \phi L/U$. As a result, when (σ, t, k_p) is known for a given Ra, then for a new Ra^*, the corresponding values are $(\sigma Ra^*/Ra, tRa/Ra^*, k_p Ra^*/Ra)$. Prior to the interaction of the boundary layer with the bottom boundary, this type of rescaling is also appropriate for obtaining the onset of convection, as shown in Fig. 2.18(a). Note that the effect of the bottom boundary is negligible as long as $\sqrt{Ra/4t} \gg 1$ [86, 107].

Chapter 3: Convective Mixing in a Continuously Perturbed Porous Media

Motivated by convective mixing of CO_2 in saline formations, this chapter [1] explores the onset of natural convection in a continuously perturbed porous system. In order to induce the convective activity, both in real aquifers and computation, perturbations of small amplitude are necessary to break the horizontal symmetry. Using different forms of perturbation has led to considerable uncertainty in characterization of stability and convective dissolution process. In this work, we consider a canonical 2-D homogeneous system where perturbations are originated from the spatial variation of porosity in the system. In contrast to an impulsively perturbed system, for which convection is induced by a sudden introduction of solute at the top of the domain, this approach results in an unconditionally unstable system where the initial perturbation time and shape function are not needed. Using a reduced nonlinear method, we first study the effect of harmonic variations of porosity in the transverse and streamwise direction on the onset time of convection and late time behavior. We show that the choice of perturbations method has a noticeable effect on the onset of convection and the subsequent nonlinear regime, in that the onset

[1] This chapter will be submitted to Physics of Fluid as 'Convective mixing in a continuously perturbed porous media'.

time of convection is reached more quickly in an impulsively perturbed system. We subsequently employ an optimization procedure, based on a Lagrange multiplier technique, to find the optimal porosity structure that leads to the earliest onset time of convection. We also develop scaling relationships for the optimal onset of convection and wavenumber in terms of aquifer properties and initial perturbation magnitude. Using high-order direct numerical simulations, we explore the long-term dissolution rates of CO_2 in such system and provide a unified picture of the dynamic of convective mixing for large values of Rayleigh number.

3.1 Overview

Natural convection, triggered by gravitational instability, plays an important role in CO_2 sequestration in subsurface saline aquifers as well as a wide range of geophysical flows [52, 72, 75]. When supercritical CO_2 is injected into a brine-saturated aquifer, the lighter CO_2 rises upward due to buoyancy, accumulates beneath an impermeable cap rock, and spreads horizontally above the heavier brine, as shown in Fig. 3.1. The supercritical CO_2 then gradually dissolves into the brine, at rates that are controlled by molecular diffusion, forming a mixture that is denser than the underlying brine [35]. The resulting stratification naturally triggers a Rayleigh-Bénard type gravitationally instability that further develops into formation of finger-like sinking plumes [26, 62, 86, 110]. A consequence of this process is the rapid dissolution of CO_2 into brine.

Convective mixing in porous media has been studied extensively to character-

ize the underlying dynamics of this process in various contexts [24,52,72,85]. Most of these studies considered an idealized system where, depending on the focus of their study, numerous features of natural formations were neglected. In order to induce natural convection, both in real aquifers and computation, perturbations of small amplitude are necessary to break the horizontal symmetry. Natural formations often exhibit complex multiscale inhomogeneity in permeability and porosity [38, 51, 90]. These micro-structural irregularities create a non-uniform flow field as the diffusive solute propagates downwards, which eventually leads to the formation of convective plumes. To trigger instability in theoretical or numerical simulation, on the other hand, perturbations are introduced in the system using various techniques. One method, which represents an impulsively forced system, requires an initial quantity of solute at the top boundary. The initial concentration profile, can be initiated either by using a random white noise [23, 53, 86] or an isolated disturbance with a predefined harmonic mode [39, 107]. Another approach, which represents a continuously perturbed system, entails defining spatially varying porosity [76], while a third method relies on the discretization errors of the numerical solver [44, 47, 68]. In the latter, depending on the specifics of the numerical solver, unphysical plume behavior may arise as a result of accumulated numerical artifacts with larger magnitude for which systematic treatment of uncertainty associated with the plume behavior is difficult, if not impossible. As a consequence, lower-order numerical schemes do not provide a suitable platform for exploring the dynamics of convective flow in porous systems. It should also be noted that in the idealized system the spatial variation of permeability alone does not set off convection as a result of the quiescent flow

assumption, and the porous system remains stable.

While the porosity-based perturbation provides a more realistic representation of natural convection in geologic formations, previous studies of convective mixing almost exclusively assumed a disturbed form of concentration for introducing perturbations. The process of natural convection depends on both the structure and the amplitude of initial conditions [24, 85]. In particular, the choice of a physically appropriate initial profile, as well as the time at which the perturbations are introduced significantly influence the dynamic of convection when the concentration-based perturbation method is used. The consequence of this approach is the introduction of the counter-intuitive notion of an optimal initial perturbation time and optimal initial concentration profile with the fastest growth [17, 81, 107]. That is, the time at which perturbations are added to the system is postponed to an arbitrary time, whereas in real systems perturbations are expected to be triggered immediately. Furthermore, in the absence of an established method for specifying an initial concentration in real settings, the notion of an optimal profile is irrelevant.

The purpose of this study is to investigate the effect of continuously forced systems on the dynamics of convective mixing in a porous layer and to also understand how this compares to a system subjected to impulse forcing. We consider two types of continuous forcing to examine the linear growth, nonlinear saturation, and full nonlinear breakdown of convective-dissolution transport: first, a continuous periodic forcing with sinusoidal variations of porosity in either two-dimension or transverse direction only, such that it represents a rounded well-sorted sediment; second, a continuous random forcing. This type of perturbation method has not

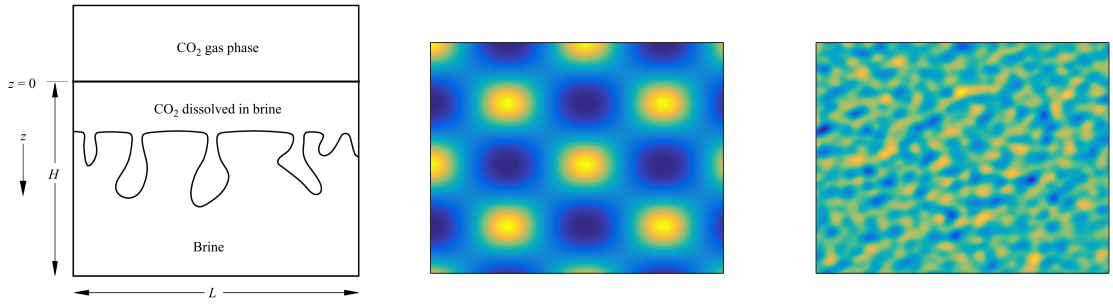

(a) (b) (c)

Figure 3.1: (a) Sketch of the 2-D porous system considered in this study. The dissolution of supercirical CO_2 into the underlying brine induces the convective mixing of the fluids and the formation of convective fingers, and the spatial variation of the porosity field using (b) harmonic distribution and (c) uncorrelated random distribution.

been explored in the context of a gravitationally unstable boundary layer, except for the work of Pau et al. [76], and its instability behavior is not well characterized. We consider an idealized canonical 2D system, in which fundamental processes can be investigated in detail, and employ three complementary methods: a fourth order asymptotic expansion, a nonlinear mean-field approximation built directly on the work of Jhaveri & Homsy [53], and high-order direct numerical simulation to systematically investigate an impulsively perturbed system. We show that this form of perturbation results in an unconditionally unstable system in a manner that mimics realistic geological settings, and hence eliminates the counter-intuitive notion of all parameters related to initial perturbation time. Further, the effect of the porosity variation on the dissolution flux is significant, whereby convection onset is occurred earlier compared to traditional perturbation type.

This chapter is laid out as follows. The governing equations and the description of the methodology and numerical approach are presented in Sec. 3.2. The effect

of continuous periodic forcing of the porosity field on the onset of convection and the subsequent nonlinear regime are discussed in Sec. 3.3. The optimal porosity structure with minimum convection onset as well as an overview of optimization procedure are provided next, followed by concluding remarks in Sec. 3.4.

3.2 Problem formulation

In this section, we present the physical model, the governing equations and numerical scheme used in this work. In §3.2.2-§3.2.3, the details of the two mathematical models based on perturbation analysis that are suitable for the analysis of harmonic porosity distribution are provided. The details of the direct numerical simulations (DNS) procedure, used to investigate the heterogeneous porosity variation, are described in §3.2.4.

3.2.1 Geometry and governing equations

We consider a two-dimensional porous medium of thickness, H, saturated with quiescent brine with a constant density, ρ_0, as schematically shown in Fig. 3.1(a). The porous layer is characterized by average porosity $\bar{\phi}$, permeability $\mathcal{K}$, and effective diffusivity $\mathcal{D}$. The layer is described by Cartesian coordinates (x, z), with x directed horizontally, and the vertical z-coordinate points downwards in the direction of gravity, g. The porous layer is bounded by super-critical CO_2 at $z = 0$, with a constant density of ρ_1 and concentration of c_1, and impermeable boundary at $z = H$. We set the horizontal domain to $L = 2\pi$ and assume periodicity in

the lateral direction. The flow and solute transport are assumed to take place at isothermal condition, and thus the interface between the supercritical CO_2 and brine may be assumed stationary at $z = 0$. The two phase interface is also considered to remain saturated [26, 62]. The density difference between the saturated and unsaturated brine is represented by $\Delta\rho = \rho_1 - \rho_0$. The relative density change, $\Delta\rho/\rho_0$, is typically of order 1% in dissolution convection process, which is sufficient to seed convective activity [26, 97].

We model single-phase density-driven flow in porous media with a constant concentration value at the top boundary using the volume averaged form of the continuity equation, the Darcy's law, and the volume averaged advection-diffusion equation. The top boundary is taken to remain saturated because the pressure is assumed to be constant and diffusion is the rate limiting factor. Under the Boussinesq approximation and assuming a linear density profile $\rho = \rho_0 + \Delta\rho$c with negligible viscosity variation [6, 31], the dimensionless form of governing equations and boundary conditions may be expressed as,

$$\nabla \cdot \mathbf{u} = 0, \qquad \nabla^2 w = \frac{\partial^2 c}{\partial x^2}, \qquad \frac{\partial(\phi c)}{\partial t} + \mathbf{u} \cdot \nabla c = \frac{1}{Ra} \nabla \cdot (\phi \nabla c) \tag{3.1}$$

$$c\Big|_{x,z=0} = 1, \qquad \frac{\partial c}{\partial z}\Big|_{x,z=1} = 0, \qquad w\Big|_{x,z=0} = w\Big|_{x,z=1} = 0 \tag{3.2}$$

where $\mathbf{u} = (u, w)$ is the Darcy velocity, c is the concentration of dissolved CO_2, ϕ is the normalized porosity, and the Rayleigh number is defined as $Ra = UH/(\bar{\phi}\mathcal{D})$. In Eq. (3.1), the domain depth, H, buoyancy velocity $U = \bar{\mathcal{K}}\Delta\rho g/\mu$, t= $\phi H/U$,

and pressure $p = \Delta\rho g H$ are used as the characteristic scaling parameters to obtain the dimensionless form of the governing equations. Equations (3.1-3.2) admits the transient base-state,

$$\boldsymbol{u}_{\mathrm{b}} = \mathbf{0}, \qquad c_b(z,t) = 1 - \frac{4}{\pi}\sum_{\mathrm{n}=1}^{\infty}\frac{1}{2\mathrm{n}-1}\sin\left[\left(\mathrm{n}-\frac{1}{2}\right)\pi z\right]\exp\left[-\left(\mathrm{n}-\frac{1}{2}\right)^2\frac{\pi^2 t}{Ra}\right] \tag{3.3}$$

In geological formation, permeability and porosity often show significant spatial variability due to the complex multi-scale character of these properties as a result of different types of depositional and tectonic processes [7,37]. Although the variation of permeability heterogeneity in natural formation is more pronounced compared to porosity variation [51], in this work permeability is assumed to be constant and the spatially varying porosity is not correlated with permeability. We define the normalized spatially varying porosity according to,

$$\phi(\mathbf{x}) = 1 + \epsilon\tilde{\phi}(\mathbf{x}) \tag{3.4}$$

where $\tilde{\phi}(\mathbf{x})$ is the spatial porosity perturbation and the amplitude of porosity perturbations, ϵ, is measured based of the L^2 norm of $\tilde{\phi}(\mathbf{x})$. The perturbation amplitude is within the range of $0 < \epsilon \ll 1$. The porosity field is normalized according to $\int_0^L \int_0^1 \phi(\mathbf{x}) dx dz = 1$, which is then used to define the average porosity, $\bar{\phi}$, as the scaling parameter in Eq. 3.1. In order to examine the porosity inhomogeneity systematically, we consider two spatial distributions: (i) a sinusoidal porosity variation in the horizontal and vertical directions, and (ii) an uncorrelated and random dis-

tribution obtained by random field theory. The details of each case is outlined in §3.3.

3.2.2 Asymptotic expansion

Following standard perturbation analysis, we assume that flow-field variables have an asymptotic expansion of the form,

$$\begin{bmatrix} c \\ u \\ w \end{bmatrix} \approx \begin{bmatrix} c_b \\ 0 \\ 0 \end{bmatrix} + \sum_{i=1}^{4} \epsilon^i \begin{bmatrix} c_i(\mathbf{x},t) \\ u_i(\mathbf{x},t) \\ w_i(\mathbf{x},t) \end{bmatrix} + \mathcal{O}\left(\epsilon^5\right) \tag{3.5}$$

where ϵ is the perturbation amplitude, defined in Eq. (3.4) and index i denotes the order of expansion. Substituting (3.5) into (3.1)–(3.2) and collecting equal powers of ϵ, we obtain a recursive sequence of partial differential equations in the form of,

$$\frac{\partial c_i}{\partial t} + w_i \frac{\partial c_b}{\partial z} - \frac{1}{Ra}\nabla^2 c_i = F_i, \qquad \nabla^2 w_i = \frac{\partial^2 c_i}{\partial x^2}, \qquad \frac{\partial u_i}{\partial x} = -\frac{\partial w_i}{\partial z} \tag{3.6a}$$

$$c_i\Big|_{z=0} = \frac{\partial c_i}{\partial z}\Big|_{z=1} = w_i\Big|_{z=0} = w_i\Big|_{z=1} = 0 \tag{3.6b}$$

where F_i may be expressed as,

$$F_1 = \frac{1}{Ra}\frac{\partial}{\partial z}(\tilde{\phi}\frac{\partial c_b}{\partial z}) - \tilde{\phi}\frac{\partial c_b}{\partial t} = \frac{1}{Ra}\frac{\partial \tilde{\phi}}{\partial z}\frac{\partial c_b}{\partial z} \tag{3.7a}$$

$$F_2 = \frac{1}{Ra}\nabla\cdot(\tilde{\phi}\nabla c_1) - \mathbf{u_1}\cdot\nabla c_1 - \tilde{\phi}\frac{\partial c_1}{\partial t} \tag{3.7b}$$

$$F_3 = \frac{1}{Ra}\nabla\cdot(\tilde{\phi}\nabla c_2) - \mathbf{u_1}\cdot\nabla c_2 - \mathbf{u_2}\cdot\nabla c_1 - \tilde{\phi}\frac{\partial c_2}{\partial t} \tag{3.7c}$$

$$F_4 = \frac{1}{Ra}\nabla\cdot(\tilde{\phi}\nabla c_3) - \mathbf{u_1}\cdot\nabla c_3 - \mathbf{u_2}\cdot\nabla c_2 - \mathbf{u_2}\cdot\nabla c_2 - \tilde{\phi}\frac{\partial c_3}{\partial t} \tag{3.7d}$$

We assume a simple spatially periodic variation of porosity in the transverse and streamwise direction which will later be instructive for the analysis of convective mixing mechanism in a more complex situation of random porosity variations. The porosity perturbation may be expressed as two spatial shape functions,

$$\tilde{\phi}(x,z) = \mathcal{F}(x)G(z) = G(z)\left[\mathrm{e}^{ikx} + \mathrm{e}^{-ikx}\right] \tag{3.8}$$

where $\mathrm{i} = \sqrt{-1}$, k is the wavenumber of horizontal porosity oscillation, and $G(z)$ is the vertical shape function which will be discussed in §3.3.

Motivated by the porosity perturbation prescribed in Eq. (3.8), we consider the following representation of the flow field $(c_1, \boldsymbol{u_1})$ to obtain the solution of the first-order problem $\mathcal{O}(\epsilon^1)$,

$$\begin{aligned} c_1 &= \widehat{c}_1(z,t)\left(\mathrm{e}^{ik_x x} + \mathrm{e}^{-ikx}\right), \quad u_1 = i\widehat{u}_1(z,t)\left(\mathrm{e}^{ikx} - \mathrm{e}^{-ikx}\right) \\ w_1 &= \widehat{w}_1(z,t)\left(\mathrm{e}^{ikx} + \mathrm{e}^{-ikx}\right) \end{aligned} \tag{3.9}$$

where $\widehat{c}(z,t)$ and $\widehat{\boldsymbol{u}}(z,t)$ are time-dependent perturbation profiles in the z direction. The spatial derivative can be expressed as,

$$\frac{\partial c_1}{\partial x} = (ik)\widehat{c}_1(z,t)\overbrace{\left(\mathrm{e}^{ikx} - \mathrm{e}^{-ikx}\right)}^{\gamma'} = (ik)\gamma'\widehat{c}_1(z,t) \tag{3.10a}$$

$$\frac{\partial^2 c_1}{\partial x^2} = (ik)^2\widehat{c}_1(z,t)\overbrace{\left(\mathrm{e}^{ikx} + \mathrm{e}^{-ikx}\right)}^{\gamma} = -k^2\gamma\widehat{c}_1(z,t) \tag{3.10b}$$

$$\frac{\partial w_1}{\partial x} = (ik)\gamma' \widehat{w}_1(z,t), \qquad \frac{\partial u_1}{\partial x} = -k\gamma \widehat{u}_1(z,t) \tag{3.10c}$$

Substituting (3.9) in (3.6) with the help of (3.10) yields,

$$\frac{\partial \widehat{c}_1}{\partial t} + \widehat{w}_1 \frac{\partial c_b}{\partial z} - \frac{1}{Ra}\left(\frac{\partial^2}{\partial z^2} - k^2\right)\widehat{c}_1 = \frac{1}{Ra}\frac{\partial G}{\partial z}\frac{\partial c_b}{\partial z} \tag{3.11a}$$

$$\left(\frac{\partial^2}{\partial z^2} - k^2\right)\widehat{w}_1 = -k^2 \widehat{c}_1, \qquad \widehat{u}_1 = \frac{1}{k}\left(\frac{\partial \widehat{w}_1}{\partial z}\right) \tag{3.11b}$$

$$\widehat{c}_1\Big|_{z=0} = \frac{\partial \widehat{c}_1}{\partial z}\Big|_{z=1} = \widehat{w}_1\Big|_{z=0} = \widehat{w}_1\Big|_{z=1} = 0, \qquad \widehat{c}_1\Big|_{t=0} = \widehat{w}_1\Big|_{t=0} = 0 \tag{3.11c}$$

At the second-order $\mathcal{O}(\epsilon^2)$, we consider the solution $(c_2, \boldsymbol{u_2})$ to be sum of the zero-wavenumber and second harmonic,

$$\begin{bmatrix} c_2 \\ u_2 \\ w_2 \end{bmatrix} = \begin{bmatrix} \widehat{c}_2^{(0)}(z,t) \\ \widehat{u}_2^{(0)}(z,t) \\ \widehat{w}_2^{(0)}(z,t) \end{bmatrix} + \begin{bmatrix} \widehat{c}_2^{(2)}(z,t) \\ \widehat{u}_2^{(2)}(z,t) \\ \widehat{w}_2^{(2)}(z,t) \end{bmatrix} \left(\mathrm{e}^{2ikx} + \mathrm{e}^{-2ikx}\right) \tag{3.12}$$

where the superscript indicate the harmonic components. The solution thereof is,

$$\frac{\partial \widehat{c}_2^{(0)}}{\partial t} - \frac{1}{Ra}\frac{\partial^2 \widehat{c}_2^{(0)}}{\partial z^2} = 2\left[\frac{\partial}{\partial z}\left(\frac{G}{Ra}\frac{\partial \widehat{c}_1}{\partial z} - \widehat{c}_1 \widehat{w}_1\right) - G\frac{\partial \widehat{c}_1}{\partial t}\right],$$

$$\widehat{u}_2^{(0)} = 0, \qquad \widehat{w}_2^{(0)} = 0 \tag{3.13a}$$

$$\frac{\partial \widehat{c}_2^{(2)}}{\partial t} + \widehat{w}_2^2 \frac{\partial c_b}{\partial z} - \frac{1}{Ra}\left(\frac{\partial^2}{\partial z^2} - 4k^2\right)\widehat{c}_2^{(2)} = \frac{1}{Ra}\left[\frac{\partial}{\partial z}\left(G\frac{\partial \widehat{c}_1}{\partial z}\right) - 2k^2 G\widehat{c}_1\right] - \left(\widehat{w}_1\frac{\partial \widehat{c}_1}{\partial z} - \widehat{c}_1\frac{\partial \widehat{w}_1}{\partial z}\right) - G\frac{\partial \widehat{c}_1}{\partial t} \tag{3.13b}$$

$$\left(\frac{\partial^2}{\partial z^2} - 4k^2\right)\widehat{w}_2^{(2)} = -4k^2 \widehat{c}_2^{(2)}, \qquad \widehat{u}_2^{(2)} = \frac{1}{2k}\left(\frac{\partial \widehat{w}_2^{(2)}}{\partial z}\right) \tag{3.13c}$$

where $\widehat{c}_2^{(0)}$, $\widehat{c}_2^{(2)}$ and $\widehat{w}_2^{(2)}$, satisfy the boundary conditions (3.11c).

At the third-order $\mathcal{O}(\epsilon^3)$, we start by assuming $(c_3, \boldsymbol{u_3})$ is the sum of the fundamental wavenumber and third harmonic,

$$\begin{bmatrix} c_3 \\ u_3 \\ w_3 \end{bmatrix} = \begin{bmatrix} \widehat{c}_3^{(1)}(z,t) \\ \widehat{u}_3^{(1)}(z,t) \\ \widehat{w}_3^{(1)}(z,t) \end{bmatrix} \left(\mathrm{e}^{ikx} + \mathrm{e}^{-ikx}\right) \begin{bmatrix} \widehat{c}_3^{(3)}(z,t) \\ \widehat{u}_3^{(3)}(z,t) \\ \widehat{w}_3^{(3)}(z,t) \end{bmatrix} \left(\mathrm{e}^{3ikx} + \mathrm{e}^{-3ikx}\right) \tag{3.14}$$

The superscript terms denote the order of the harmonic components and the solution can be written as,

$$\begin{aligned} \frac{\partial \widehat{c}_3^{(1)}}{\partial t} + \widehat{w}_3^{(1)}\frac{\partial c_b}{\partial z} - \frac{1}{Ra}\left(\frac{\partial^2}{\partial z^2} - k^2\right)\widehat{c}_3^{(1)} = \frac{1}{Ra}\left[\frac{\partial}{\partial z}G\left(\frac{\partial \widehat{c}_2^{(0)}}{\partial z} + \frac{\partial \widehat{c}_2^{(2)}}{\partial z}\right) - 2k^2 G\widehat{c}_2^{(2)}\right] \\ - G\left(\frac{\partial \widehat{c}_2^{(0)}}{\partial t} + \frac{\partial \widehat{c}_2^{(2)}}{\partial t}\right) - 2\widehat{c}_2^{(2)}\frac{\partial \widehat{w}_1}{\partial z} - \widehat{w}_1\frac{\partial \widehat{c}_2^{(0)}}{\partial z} - \widehat{w}_1\frac{\partial \widehat{c}_2^{(2)}}{\partial z} \\ - \frac{\widehat{c}_1}{2}\frac{\partial \widehat{w}_2^{(2)}}{\partial z} - \widehat{w}_2^{(2)}\frac{\partial \widehat{c}_1}{\partial z} \end{aligned} \tag{3.15a}$$

$$\begin{aligned} \frac{\partial \widehat{c}_3^{(3)}}{\partial t} + \widehat{w}_3^{(3)}\frac{\partial c_b}{\partial z} - \frac{1}{Ra}\left(\frac{\partial^2}{\partial z^2} - 9k^2\right)\widehat{c}_3^{(3)} = \frac{1}{Ra}\left[\frac{\partial}{\partial z}\left(G\frac{\partial \widehat{c}_2^{(2)}}{\partial z}\right) - 6k^2 G\widehat{c}_2^{(2)}\right] \\ - G\frac{\partial \widehat{c}_2^{(2)}}{\partial t} + 2\widehat{c}_2^{2}\frac{\partial \widehat{w}_1}{\partial z} - \widehat{w}_1\frac{\partial \widehat{c}_2^{(2)}}{\partial z} + \frac{\widehat{c}_1}{2}\frac{\partial \widehat{w}_2^{(2)}}{\partial z} - \widehat{w}_2^{(2)}\frac{\partial \widehat{c}_1}{\partial z} \end{aligned} \tag{3.15b}$$

$$\left(\frac{\partial^2}{\partial z^2} - 9k^2\right)\widehat{w}_3^{(3)} = -9k^2\widehat{c}_3^{(3)}, \qquad \widehat{u}_3^{(3)} = \frac{1}{3k}\left(\frac{\partial \widehat{w}_3^{(3)}}{\partial z}\right) \tag{3.15c}$$

where $\widehat{c}_3^{(1)}$, $\widehat{c}_3^{(3)}$, $\widehat{w}_3^{(3)}$ and $\widehat{w}_3^{(3)}$ satisfy the boundary (3.11c) and the functions $\widehat{u}_3^{(1)}$, $\widehat{w}_3^{(1)}$ are the same $\widehat{u}_1$, $\widehat{w}_1$ in Eq. (3.11b).

At the fourth-order $\mathcal{O}(\epsilon^4)$, we seek a solution as sum of three responses to the forcing at the zero-wavenumber, second and fourth harmonic,

$$\begin{bmatrix} c_4 \\ u_4 \\ w_4 \end{bmatrix} = \begin{bmatrix} \widehat{c}_4^{(0)}(z,t) \\ \widehat{u}_4^{(0)}(z,t) \\ \widehat{w}_4^{(0)}(z,t) \end{bmatrix} + \begin{bmatrix} \widehat{c}_4^{(2)}(z,t) \\ \widehat{u}_4^{(2)}(z,t) \\ \widehat{w}_4^{(2)}(z,t) \end{bmatrix} \left(\mathrm{e}^{2ikx} + \mathrm{e}^{-2ikx}\right) + \begin{bmatrix} \widehat{c}_4^{(4)}(z,t) \\ \widehat{u}_4^{(4)}(z,t) \\ \widehat{w}_4^{(4)}(z,t) \end{bmatrix} \left(\mathrm{e}^{4ikx} + \mathrm{e}^{-4ikx}\right) \tag{3.16}$$

We next determine the solution to the $\mathcal{O}(\epsilon^4)$ problem which satisfies the following system of equations,

$$\frac{\partial \widehat{c}_4^{(0)}}{\partial t} - \frac{1}{Ra}\frac{\partial^2 \widehat{c}_4^{(0)}}{\partial z^2} = 2\left\{\frac{\partial}{\partial z}\left(\frac{G}{Ra}\frac{\partial \widehat{c}_3^{(1)}}{\partial z} - \widehat{c}_3^{(1)}\widehat{w}_1 - \widehat{c}_1\widehat{w}_3^{(1)} - \widehat{c}_2^{(2)}\widehat{w}_2^{(2)}\right) - G\frac{\partial \widehat{c}_3^{(1)}}{\partial t}\right\} \tag{3.17a}$$

$$\begin{aligned}\frac{\partial \widehat{c}_4^{(2)}}{\partial t} + \widehat{w}_4^{(2)}\frac{\partial c_b}{\partial z} - \frac{1}{Ra}\left(\frac{\partial^2}{\partial z^2} - 4k^2\right)\widehat{c}_4^{(2)} &= \frac{1}{Ra}\left\{\frac{\partial}{\partial z}G\left(\frac{\partial \widehat{c}_3^{(1)}}{\partial z} + \frac{\partial \widehat{c}_3^{(3)}}{\partial z}\right)\right\} \\ &- G\left(2k^2\widehat{c}_3^{(1)} + 6k^2\widehat{c}_3^{(3)}\right) - G\left(\frac{\partial \widehat{c}_3^{(1)}}{\partial t} + \frac{\partial \widehat{c}_3^{(3)}}{\partial t}\right) + \widehat{c}_3^{(1)}\frac{\partial \widehat{w}_1}{\partial z} \\ &- \widehat{w}_1\frac{\partial \widehat{c}_3^{(1)}}{\partial z} - 3\widehat{c}_3^{(3)}\frac{\partial \widehat{w}_1}{\partial z} - \widehat{w}_1\frac{\partial \widehat{c}_3^{(3)}}{\partial z} - \widehat{w}_2^{(2)}\frac{\partial \widehat{c}_2^{(0)}}{\partial z} \\ &+ \frac{\widehat{c}_1}{3}\left(\frac{\partial \widehat{w}_3^{(1)}}{\partial z} - \frac{\partial \widehat{w}_3^{(3)}}{\partial z}\right) - \frac{\partial \widehat{c}_1}{\partial z}\left(\widehat{w}_3^{(1)} + \widehat{w}_3^{(3)}\right)\end{aligned} \tag{3.17b}$$

$$\begin{aligned}\frac{\partial \widehat{c}_4^{(4)}}{\partial t} + \widehat{w}_4^{(4)}\frac{\partial c_b}{\partial z} - \frac{1}{Ra}\left(\frac{\partial^2}{\partial z^2} - 4k^2\right)\widehat{c}_4^{(4)} &= \frac{1}{Ra}\left\{\frac{\partial}{\partial z}\left(G\frac{\partial \widehat{c}_3^{(3)}}{\partial z}\right) - 12Gk^2\widehat{c}_3^{(3)}\right\} \\ &- G\frac{\partial \widehat{c}_3^{(3)}}{\partial t} + 3\widehat{c}_3^{(3)}\frac{\partial \widehat{w}_1}{\partial z} - \widehat{w}_1\frac{\partial \widehat{c}_3^{(3)}}{\partial z} + \widehat{c}_2^{(2)}\frac{\partial \widehat{w}_2^{(2)}}{\partial z} - \widehat{w}_2\frac{\partial \widehat{c}_2^{(2)}}{\partial z} \\ &+ \frac{\widehat{c}_1}{3}\frac{\partial \widehat{w}_3^{(3)}}{\partial z} - \widehat{w}_3^{(3)}\frac{\partial \widehat{c}_1}{\partial z}\end{aligned} \tag{3.17c}$$

$$\left(\frac{\partial^2}{\partial z^2} - 16k^2\right)\widehat{w}_4^{(4)} = 9k^2\widehat{c}_4^{(4)}, \qquad \widehat{u}_4^{(4)} = \frac{1}{4k}\left(\frac{\partial \widehat{w}_4^{(4)}}{\partial z}\right) \tag{3.17d}$$

where all the harmonic responses satisfy the boundary (3.11c) and the functions

$\widehat{u}_4^{(2)}$, $\widehat{w}_4^{(2)}$ are the same $\widehat{u}_2^{(2)}$, $\widehat{w}_2^{(2)}$ in Eq. (3.13c).

The resulting sequence of partial differential equations (3.11–3.17) can be solved in a successive manner. The system of equations is discretized using a Chebyshev polynomial expansion along Gauss-Lobatto collocation points, and the time integration is performed with a third-order backward scheme [77] using a dynamic time stepping. The temporal discretization of the advection term uses an explicit Adams-Bashforth scheme, while the diffusion terms are treated implicitly.

3.2.3 Mean-field approximation

In this section, we extend the mean-field approximation model of Jhaveri & Homsy [53], used in a study of transient thermal boundary layers in pure fluid media, to include the effect of porosity variation. The nonlinear model assumes a nonlinear interaction between the fundamental wavenumber and zero-wavenumber and neglects the nonlinear interactions of higher-order harmonics. The flow-field variables may be expanded as,

$$\begin{bmatrix} c \\ u \\ w \end{bmatrix} \approx \begin{bmatrix} c_b(z,t) + \widehat{c}_m(z,t) \\ 0 \\ 0 \end{bmatrix} + \begin{bmatrix} \widehat{c}_k(z,t)\left(\mathrm{e}^{ikx} + \mathrm{e}^{-ikx}\right) \\ i\widehat{u}_k(z,t)\left(\mathrm{e}^{ikx} - \mathrm{e}^{-ikx}\right) \\ \widehat{w}_k(z,t)\left(\mathrm{e}^{ikx} + \mathrm{e}^{-ikx}\right) \end{bmatrix} \tag{3.18}$$

The effect of nonlinear interactions in (3.18) is enforced through the modification of the mean concentration, $\widehat{c}_m(z,t)$. The main feature of approximation (3.18) is assuming that the relative magnitudes of $\widehat{c}_m$, $\widehat{c}_k$, $\widehat{u}_k$, and $\widehat{w}_k$ are comparable and the

perturbation magnitude remains sufficiently small.

The nonlinear mean-field equations are obtained by substituting (3.18) into the governing equations (3.1)–(3.2) and neglecting the nonlinear interactions that lead to second-harmonic terms,

$$\frac{\partial \widehat{c}_m}{\partial t} - \frac{1}{Ra}\frac{\partial^2 \widehat{c}_m}{\partial z^2} = 2\left\{\frac{\partial}{\partial z}\left(\frac{\epsilon G}{Ra}\frac{\partial \widehat{c}_k}{\partial z} - \widehat{w}_c\widehat{c}_k\right) - \epsilon G\frac{\partial \widehat{c}_k}{\partial t}\right\} \tag{3.19a}$$

$$\frac{\partial \widehat{c}_k}{\partial t} + \widehat{w}_k\left(\frac{\partial c_b}{\partial z} + \frac{\partial \widehat{c}_m}{\partial z}\right) - \frac{1}{Ra}\left(\frac{\partial^2}{\partial z^2} - k^2\right)\widehat{c}_k \tag{3.19b}$$
$$= \frac{\epsilon}{Ra}\left\{\frac{\partial}{\partial z}\left(G\frac{\partial \widehat{c}_m}{\partial z}\right) + \frac{\partial G}{\partial z}\frac{\partial c_b}{\partial z}\right\} - \epsilon G\frac{\partial \widehat{c}_m}{\partial t}$$

$$\left(\frac{\partial^2}{\partial z^2} - k^2\right)\widehat{w}_k = -k^2\widehat{c}_k \tag{3.19c}$$

$$\widehat{c}_k\Big|_{z=0} = \widehat{c}_m\Big|_{z=0} = \frac{\partial \widehat{c}_k}{\partial z}\Big|_{z=1} = \frac{\partial \widehat{c}_m}{\partial z}\Big|_{z=1} = \widehat{w}_k\Big|_{z=0} = \widehat{w}_k\Big|_{z=1} = 0, \qquad \widehat{c}_k\Big|_{t=0} = \widehat{c}_m\Big|_{t=0} = 0 \tag{3.19d}$$

Equation (3.19a) is similar to the second-order equation (3.13) for $\widehat{c}_2^{(0)}$. The equations (3.19(b-c)) are similar to the asymptotic expansion (3.11) for $\widehat{c}_1$ and $\widehat{w}_1$, except for the additional nonlinear advection term $\widehat{w}_k(\partial c_m/\partial z)$. In contrast to asymptotic expansion (3.5), which only needs to be solved once for a given k, k_z, γ, and Ra, Eq. (3.19) is nonlinear and depends on the initial amplitude, ϵ, and must be solved for every given ϵ, similar to DNS. The numerical solution of the mean-flow approximation Eq. (3.19) is similar to the asymptotic expansion, as explained in previous section.

3.2.4 High-order DNS

The two-dimensional DNS of the governing equations (3.1) are performed by adopting a stream function–vorticity formulation [86, 89, 99] such that $(u, w) = (\partial_z \psi\,, -\partial_x \psi)$. The resulting Poisson equation is then discretized spatially using a Fourier expansion in the horizontal x direction and a sixth-order compact finite differences in the vertical z direction [60]. The advection–diffusion equation is solved numerically with a sixth-order compact finite differences in both horizontal and vertical directions and a third-order Runge-Kutta scheme with dynamic time-stepping is used for time integration. The horizontal domain is set to $x \in [0, 2\pi]$ and periodic boundary conditions are used in the x direction.

3.2.5 Global measures of convective mixing parameters

In this section, we define a number of global parameters to characterize various stage of mixing regimes and the overall behavior of convective dissolution. The most practically important measure is dissolution flux, which quantifies how much CO_2 dissolves into the system through the buoyant plumes that are induced by natural convection. The dissolution flux is defined as the rate of change of the total dissolved CO_2 across the interface ($z = 0$) and may be expressed in the dimensionless form as,

$$\mathcal{J}(t) = \frac{1}{L}\int_0^L \frac{1}{Ra}\frac{\partial c}{\partial z}\Big|_{z=0} dx \tag{3.20}$$

where L is the domain width, and the definition of Ra is provided in §3.2.1. Substituting (3.5) into (3.20), the dissolution flux computed from the asymptotic expansion can be expressed by,

$$\mathcal{J}(t) = -\frac{1}{Ra}\left(\frac{\partial c_b}{\partial z} + \epsilon^2\frac{\partial \widehat{c}_2^{(0)}}{\partial z} + \epsilon^4\frac{\partial \widehat{c}_4^{(0)}}{\partial z}\right)\Big|_{z=0} \tag{3.21}$$

The dissolution flux from the mean-field approximation can be obtained in a similar manner.

The time history of flux, as illustrated in Fig. 3.2, shows three distinct stages of evolution: the linear growth regime, the onset and growth of convection, and the late-time or post saturation period. After an initial decay period due to the stabilizing effect of diffusion, the dissolution flux switches from negative to positive growth rate, i.e $d\mathcal{J}/dt = 0$, at the onset time of convection t_{cv}. The onset time of convection, indicated as solid dots in Fig. 3.2, initiates a period of accelerated flux growth due to the growth of nonlinear mechanisms. The increasing dissolution flux quickly attains a maximum value at the onset of nonlinear saturation, t_s, highlighted as a square symbol in Fig. 3.2. Following this event, the flux begins to decrease as the result of merging and coarsening process of convective plumes which eventually leads to saturation of the entire domain once buoyant plumes interact with the bottom boundary.

The perturbation growth can be quantified by measuring the individual contributions of each horizontal Fourier mode of the perturbation away from pure diffusion

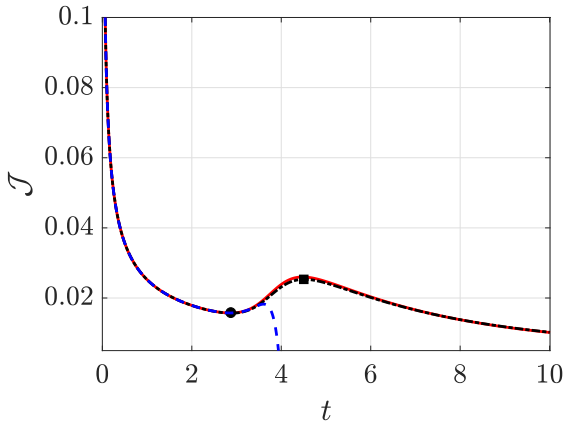

Figure 3.2: Comparison of time evolution of dissolution flux obtained by DNS (dash-dotted line) with asymptotic expansion (dashed line) and mean-field approximation (solid line) when $\epsilon = 0.01$, $k_x = 30, k_z = 1$, and $\gamma = 0$. The solid dot and square symbol mark the onset time of convection and saturation, respectively.

according to the following norm,

$$E_l(t) = \left\{ \frac{1}{\lambda_l} \int_0^{\lambda_l} \int_0^1 \frac{1}{2} \left(\tilde{c}_l^2 + \tilde{u}_l^2 + \tilde{w}_l^2 \right) dz\, dx \right\}^{1/2} \tag{3.22}$$

The term $E_l(t)$ denotes the magnitude of each horizontal Fourier mode of the DNS perturbation field integrated along the direction of gravity and $\lambda = 2\pi/l$ is the mode's wavelength. The concentration and velocity perturbation fields $(\widetilde{c}_l, \widetilde{u}_l, \widetilde{w}_l)$ are computed by subtracting the base-state, (Eq. 3.3), from their corresponding DNS flow field. The Fourier components of perturbation fields are obtained by employing classical FFT routines. In the following, the terms zero-wavenumber, or mean-flow mode, and fundamental mode refers to E_0 and E_k, respectively. The magnitude of zero-wavenumber, or mean-flow mode, and the first four harmonics for the asymptotic expansion are obtained by substituting (3.5) into (3.22) and can be expressed by,

$$E_0 = \left\{ \int_0^1 \left[(\epsilon^2 \widehat{c}_2^{(0)})^2 + (\epsilon^4 \widehat{c}_4^{(0)})^2 \right] dz \right\}^{1/2} \tag{3.23a}$$

$$E_k = \epsilon \left\{ \int_0^1 \left[(\widehat{u}_1)^2 + (\widehat{w}_1)^2 + (\widehat{c}_1)^2 \right] dz \right\}^{1/2} + \epsilon^3 \left\{ \int_0^1 \left[(\widehat{u}_3^{(1)})^2 + (\widehat{w}_3^{(1)})^2 + (\widehat{c}_3^{(1)})^2 \right] dz \right\}^{1/2} \tag{3.23b}$$

$$E_{2k} = \epsilon^2 \left\{ \int_0^1 \left[(\widehat{u}_2^{(2)})^2 + (\widehat{w}_2^{(2)})^2 + (\widehat{c}_2^{(2)})^2 \right] dz \right\}^{1/2} + \epsilon^4 \left\{ \int_0^1 \left[(\widehat{u}_4^{(2)})^2 + (\widehat{w}_4^{(2)})^2 + (\widehat{c}_4^{(2)})^2 \right] dz \right\}^{1/2} \tag{3.23c}$$

$$E_{3k} = \epsilon^3 \left\{ \int_0^1 \left[(\widehat{u}_3^{(3)})^2 + (\widehat{w}_3^{(3)})^2 + (\widehat{c}_3^{(3)})^2 \right] dz \right\}^{1/2} \tag{3.23d}$$

$$E_{4k} = \epsilon^4 \left\{ \int_0^1 \left[(\widehat{u}_4^{(4)})^2 + (\widehat{w}_4^{(4)})^2 + (\widehat{c}_4^{(4)})^2 \right] dz \right\}^{1/2} \tag{3.23e}$$

To examine the evolution of the convective fingers structure and particular feature of mixing dynamic, we compute the horizontally averaged mean concentration $\langle c \rangle$ and the mean square concentration perturbation $\langle \tilde{c}^2 \rangle$ according to,

$$\langle q \rangle (z,t) = \frac{1}{L} \int_0^L q \, dz \, dx, \;\; \text{where } q = (c, \tilde{c}^2) \tag{3.24}$$

The variation of $\langle \tilde{c}^2 \rangle$ can essentially be interpreted as an the strength of downwelling convective fingers. The corresponding averaged profiles associated to their linearized methods counterparts can be obtained in a similar fashion.

Another useful plume characteristic is the averaged wavelength of the convec-

tive fingers which is defined as,

$$\lambda = 2\pi \frac{\int_0^{\tilde{K}} lE(l)\, dl}{\int_0^{\tilde{K}} E(l)\, dl} \tag{3.25}$$

where l is the constituent Fourier modes of the Fourier transform of $\langle c \rangle$ and $E(l)$ is the corresponding amplitude in the Fourier domain.

It is also useful to measure the time evolution of the convective plume penetration front, as well as the rate at which the center of mass of plume propagates downward. We define the location of plume penetration front as a depth from the top of the domain for which $\langle c \rangle = 0.01$.

$$z_{cm}(t) = \frac{\int_0^1 z \langle c \rangle\, dz}{\mathcal{M}} \tag{3.26}$$

3.3 Continuous forcing in a 2-D periodic porosity structure

In this section, we investigate the effect of a simple, yet instructive, porosity distribution to determine the characteristics and contributing factors associated with growth of instabilities and convective mixing pattern. The porosity perturbation in the horizontal direction, $F(x)$, is taken to vary sinusoidally, as described in Eq. (3.8), whereas we consider two models to describe the variation in the vertical direction, $G(z)$. The first model assumes the spatially periodic $G(z)$ takes the form of $G(z) = \cos(k_z z + \gamma)$ where k_z and γ denote the vertical wavenumber and phase shift, respectively. The second model determines the optimal vertical profile, $G(z)$,

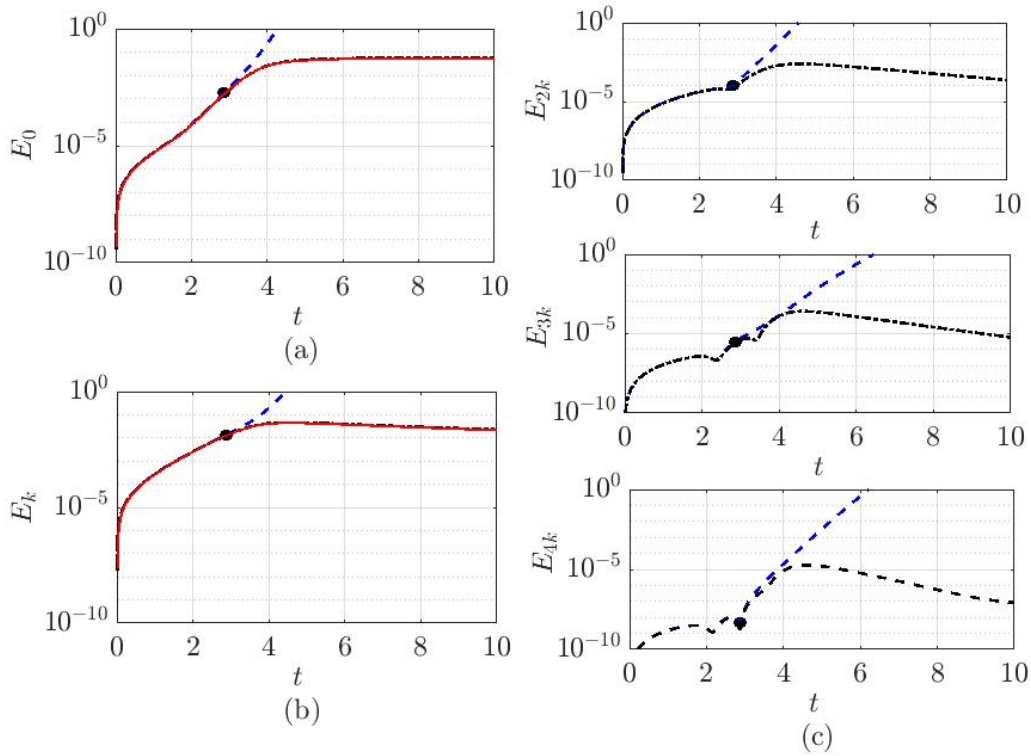

Figure 3.3: Evolution of the perturbation energy for the parameters range of Fig. 3.2 obtained by DNS (dash-dotted line), asymptotic expansion (dashed line) and mean-field approximation (solid line). The onset time of convection is highlighted with a solid dot.

that results in an earliest onset time of convection using an augmented Lagrangian approach.

We begin our analysis by comparing the results obtained by asymptotic expansion and mean-field approximation with DNS. Figure 3.2 compares the time history of flux obtained by DNS with the linearized methods when $k_x = 20$, $k_z = 1$, $\epsilon = 0.01$ and $Ra = 500$. The linear regime and the onset time of convection are accurately predicted by asymptotic expansion as well as the mean-field approximation. The relative error in prediction of t_{cv} is less than 0.4% among three methods. During the flux growth stage, however, the asymptotic expansion over predicts solute flux. This

is due to the unbounded growth of the mean-flow mode which eventually leads to the expansion breakdown at $t = 3.7$. To extend the accuracy of the asymptotic expansion to the post-onset regime, the computation of higher order terms in Eq. (3.5) is necessary. The introduction of higher order terms modifies the growth of mean-flow mode and lower harmonics slowing down their developments and thus regularizing the expansion. On the other hand, there is an excellent agreement between DNS and mean-field approximation result in predicting the nonlinear saturation and late time behavior. The mean-field approximation predicts t_s with a relative error of 1%. The success of mean-field approximation can be explained by noting that no assumption was made about the relative magnitude of $\hat{c}_m$ and $\hat{c}_k$.

For the present range of parameters, Fig. 3.3 compares the evolution of modal perturbation growth computed by DNS and the linearized methods. In contrast to the concentration-based perturbation approach, the perturbation magnitude of $E_l = (E_0, E_k, E_{2k}, E_{3k}, E_{3k})$, experiences an immediate growth which indicated an unconditionally unstable porous system, as a result of the immediate growth set by $F_1 = 1/Ra\,(\partial_z\,\tilde{\phi}\partial_z c_b)$ (see Eq. 3.7a). This questions the relevance of a significant amount of studies in the past decades that has been largely focused on obtaining the critical onset time of instability and determining a series of parameters, such as optimal initial perturbation time, that results in the maximum perturbation growth. Figure 3.3 shows a rapid modal growth of perturbations, which is captured accurately by the linearized methods, is observed preceding the onset time of convection. Following the onset time of convection, E_0 becomes of the same order of E_k and eventually surpasses the fundamental mode at $t = 5$ due to the nonlinear

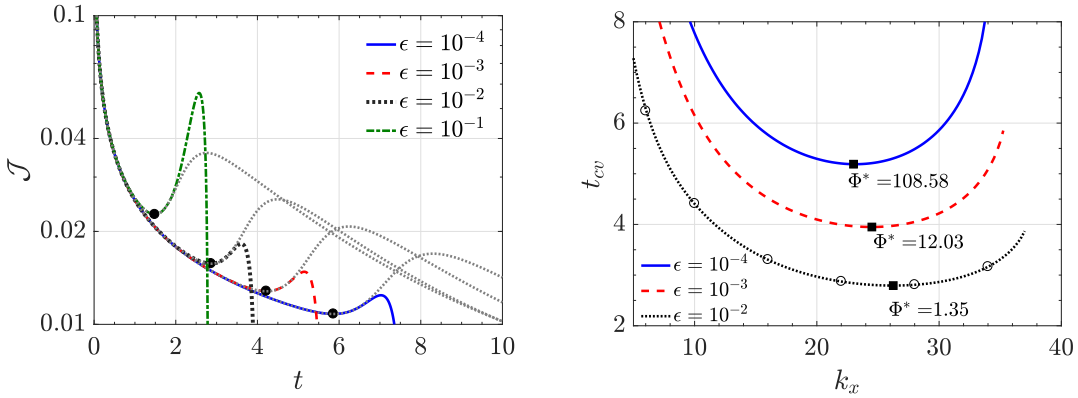

(a) (b)

Figure 3.4: (a) Time evolution of dissolution flux obtained by asymptotic expansion when $k_x = 30, k_z = 1$, and $\gamma = 0$. The dotted lines represent the corresponding DNS results and the onset of nonlinear convection is highlighted with the solid dot. (b) The onset time of convection vs horizontal wavenumber for three different values of ϵ when $k_z = 1$ and $\gamma = 0$. The open symbols shows the corresponding DNS values and the square symbols indicate the critical point (k^*, t^*_{cv}).

interactions while the modal growth of higher harmonics is an other of magnitude smaller compared to E_0 and E_k. This explains the success of the mean-field approximation in predicting the post onset events because it assumes $\hat{c}_m$ and $\hat{c}_k$ are of equal-order. The deviation of the asymptotic expansion results from DNS, in this regime, indicates the unbounded growth of the zero-wavenumber mode, which in turn alters the growth rate of higher harmonics. The accuracy of expansion results can be improved by computing higher order terms in the expansion series where their appearance changes the growth rate of the mean-flow mode and other harmonics slightly which is sufficient to delay the departure of expansion predictions from DNS results.

3.3.1 Influence of perturbation amplitude

Figure 3.4(a) illustrates the time evolution of the dissolution flux for four values of perturbation amplitude, $\epsilon = 10^{-4}$, 10^{-3}, 10^{-2}, and 10^{-1} when $k_z = 1$ and $k_x = 30$. As expected, the onset time of convection, t_{cv}, shifts to an earlier time with increasing ϵ, and the dissolution flux at t_{cv} increases. The asymptotic expansion accurately predicts the weakly nonlinear regime within 0.5% of DNS, however, the accuracy of asymptotic expansion is limited to the small perturbation amplitude, $\epsilon \ll 1$, and a relatively large amplitude ($\epsilon > 0.1$) results in a significant discrepancy between DNS and asymptotic expansion results. Consequently, the asymptotic expansion method is not suitable for systems with large porosity variations. Moreover, the porosity-based perturbation approach allows to prescribe a higher ϵ without producing unphysical negative concentration compared to a concentration-based perturbation approach. Figure 3.4(a) further indicates that the onset time of convection is also attained when $\epsilon = 10^{-4}$. Many studies, however, neglected the effect of porosity and assumed a constant value. It is clear that although the variation of porosity in natural formation is not as pronounced compared to permeability heterogeneity [38,51], it can significantly influence the dynamics of convective mixing.

The onset time of convection, t_{cv}, is plotted as a function of k_x in Fig. 3.4(b) for three values of ϵ when $k_z = 1$ and $\gamma = 0$. In each case, convection does not occur for large k_x because of the substantial damping associated with these values of k_x due to an increase in the stabilizing transverse diffusive terms, $(j\,k^2/Ra)\,\hat{c}_j$ where

the index j denotes the order of asymptotic expansion. Figure 3.4(b) further shows that the computed t_{cv} obtained by DNS and asymptotic expansion are visually indistinguishable. We note that the asymptotic expansion method is numerically simpler and more computationally efficient compared to DNS because it only requires the solution of a hierarchy of systems of linear partial differential equations.

The critical onset time t^*_{cv}, shown as square symbol in Fig. 3.4(b), marks the minimum value of t_{cv} among all horizontal wavenumbers k_x for the present set of parameters. Clearly, t^*_{cv} depends on k_z and γ, which is discussed in more details in §3.3.2. The value of t^*_{cv} transitions to an earlier time with increasing perturbation amplitude, while an increase in the corresponding wavenumber, k^*_x, is observed (see Fig. 3.5).

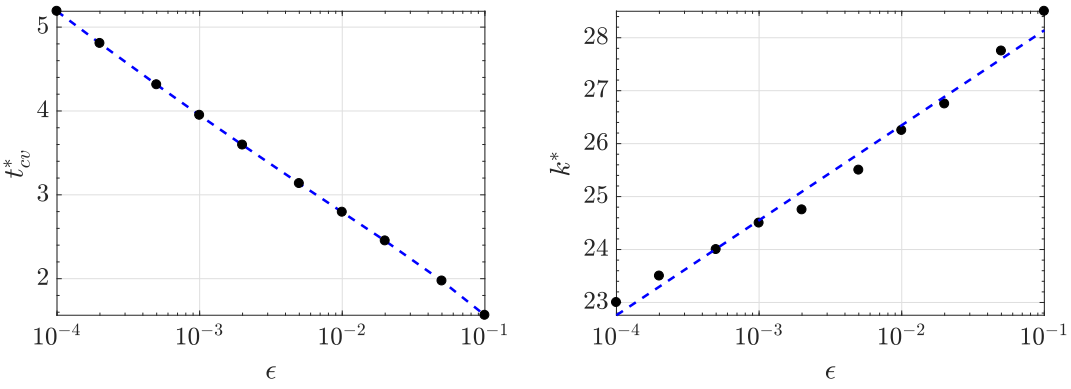

Figure 3.5: The scaling results produced by asymptotic expansion when $k_z = 1$ and $\gamma = 0$. (a) the critical onset time of convection, t^*_{cv} and (b) the critical horizontal wavenumber, k^*. The dashed lines show the corresponding fit (3.27).

We repeat the procedure shown in Fig. 3.4(b) for perturbation amplitude in the range of $10^{-4} \leq \epsilon \leq 10^{-1}$. Figure 3.5 shows the variation of the critical onset time of convection and critical horizontal wavenumber with ϵ when $k_z = 1$ and

$\gamma = 0$. The following relationship, shown as a dashed line in Fig. 3.5, are obtained from the figure,

$$t^*_{cv} = -1.19 \log_{10} \epsilon + 0.401, \qquad k^* = 0.779 \log_{10} \epsilon + 29.935 \tag{3.27}$$

In order to associate t_{cv} to the perturbation growth, we measure the amplification of perturbation for a time interval from $t = 0$ to t as a ratio of their fundamental energy defined as $\Phi(k, t) = E_k(t)/\epsilon$. The corresponding value of amplification at t^*_{cv} is noted as Φ^*_k in Fig. 3.4(b) for different values of ϵ. The critical amplification, Φ^*_k, decreases with increasing initial perturbation amplitude because perturbations with larger ϵ require less amplification to trigger the convection onset. For a given ϵ, Φ^*_k is the threshold value of amplification required to trigger the onset of convection. The critical amplification is independent of k_x and satisfies the following sub-linear scaling relationship, shown in Fig. 3.6 for the parameters range of Fig. 3.4(b),

$$\Phi^* = 0.0158\, \epsilon^{-0.961} \tag{3.28}$$

Note that the scaling relationship (3.27–3.28) changes with the phase and wavenumber of vertical porosity structure.

3.3.2 Influence of wavelength and phase shift

Figure 3.7(a) demonstrates the effect of k_z on the temporal evolution of dissolution flux when $k_x = 30$, $\gamma = 0$, and $\epsilon = 0.01$. For a given k_z, there is an

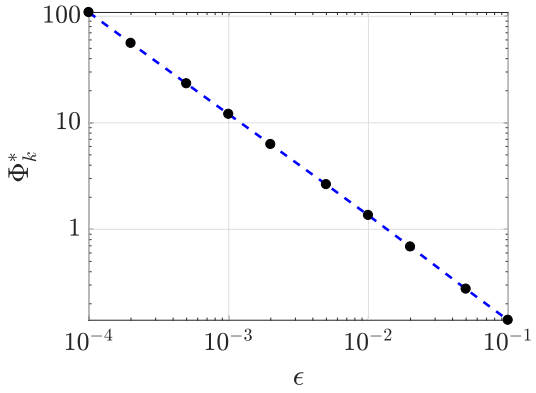

Figure 3.6: The scaling results produced by asymptotic expansion for Φ^* when $k_z = 1$ and $\gamma = 0$. The dashed line shows the corresponding fit (3.28).

excellent agreement between $\mathcal{J}$ computed by DNS and asymptotic expansion prior to the nonlinear regime. The value of t_{cv}, shown as a solid dot in Fig. 3.7(a), changes non-monotonically with increasing k_z. Among the examined range of k_z in Fig. 3.7(a), the earliest onset of convection occurs when $k_z = 10$. In this case, Φ_k, that is displayed in Fig. 3.7(b), is greater compared to $k_z = 1$ and $k_z = 20$ at all times. Consequently, the critical amplification required to trigger the onset of convection is attained sooner for $k_z = 10$, leading to an earlier convection onset. We also note that Φ_k has a maximum occurring at the onset time of saturation, and shortly thereafter decays at the same rate for present range of k_z values.

We now examine whether the non-monotonic behavior noted in Fig. 3.10 can be explained by examining the instantaneous perturbation vorticity field. The vorticity equation, obtained by taking curl of the Darcy equation (3.1), may be expressed as,

$$\Omega = \Omega_c + \Omega_p = \mathcal{K}\nabla c \times \nabla z + \nabla(\ln \mathcal{K}) \times \mathbf{u} \tag{3.29}$$

Equation 3.29 indicates the existence of two vorticity modes, related to mis-

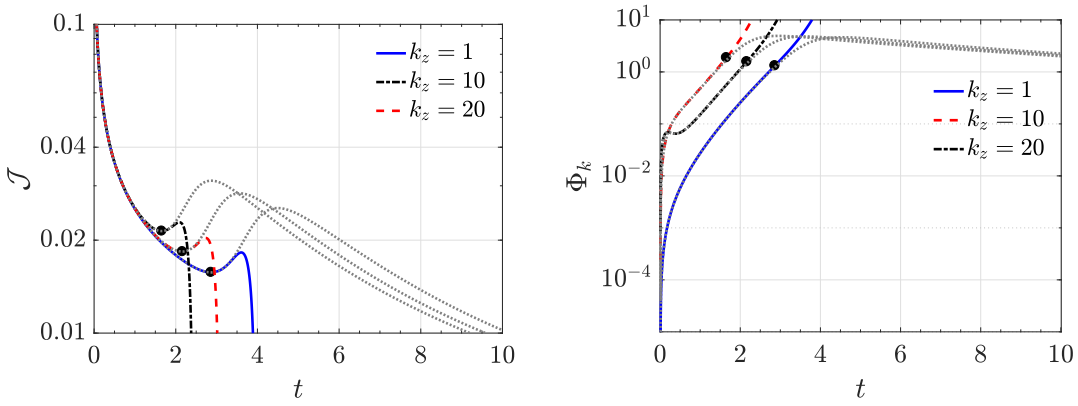

(a) (b)

Figure 3.7: DNS and expansion results when $k_x = 30$, $\gamma = 0$, and $\epsilon = 0.01$. (a) Time evolution of dissolution flux, (b) Corresponding time evolution of amplification. The dotted lines show the corresponding DNS results and the solid dot marks the onset time of convection.

alignment of the concentration gradient with the gravity and the misalignment of the velocity field with the gradient of $\ln \mathcal{K}$, respectively. In the absence of permeability variation, only the concentration-related vorticity component is present. Motivated by spatially periodic flow fields variable (3.9), and assuming vorticity takes the form of $\Omega(z,t) = \sum_{j=1}^{4} i\,\gamma_j' \widehat{\Omega}_j(z,t)$ with index j denoting the expansion order and $\gamma_j' = \left(\mathrm{e}^{ikjx} - \mathrm{e}^{-ikjx}\right)$, the resulting vorticity equation can be expressed as,

$$\widehat{\Omega}(z,t) = \underbrace{k\,(\epsilon\widehat{c}_1 + \epsilon^3\widehat{c}_3^{(1)})\gamma'}_{\widehat{\Omega}_1} + \underbrace{2k(\epsilon^2\widehat{c}_2^{(2)} + \epsilon^4\widehat{c}_4^{(2)})\gamma_2'}_{\widehat{\Omega}_2} + \underbrace{3k\,\epsilon^3\widehat{c}_3^{(3)}\gamma_3'}_{\widehat{\Omega}_3} + \underbrace{4k\,\epsilon^4\widehat{c}_4^{(4)}\gamma_4'}_{\widehat{\Omega}_4} \tag{3.30}$$

It is also instructive to measure the spatially cumulative effect of vorticity production by integrating Eq. 3.30, which yields,

$$\mathcal{I}(t) = \int_0^1 \widehat{\Omega}(z,t)\,dz = \sum_{j=1}^{4} \mathcal{I}_i \tag{3.31}$$

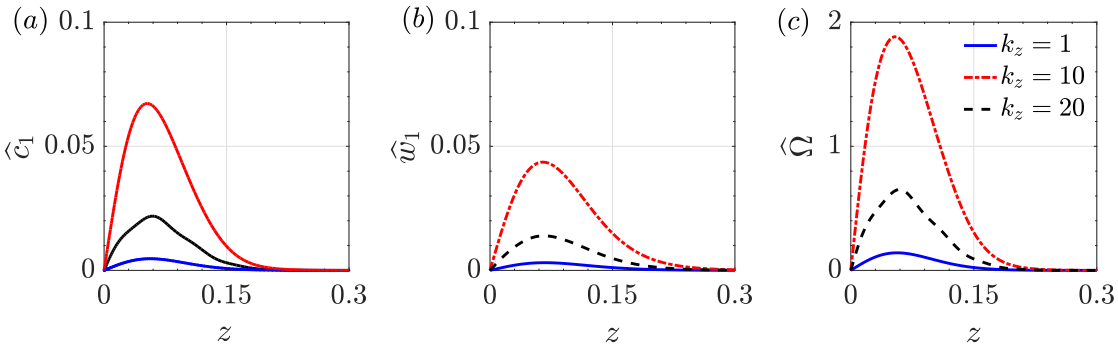

Figure 3.8: Effect of k_z on the spatial variation of (a) concentration, (b) velocity, and (c) vorticity when $k_x = 30$, $\gamma = 0$, and $\epsilon = 0.01$ at $t = 1.65$. The solid dot displays the thickens of the diffusive boundary layer. The perturbation profiles experience a substantial boost when $k_z = 10$.

where $\mathcal{I}_i$ indicates the net vorticity associated with the i^{th} order concentration-related vorticity component.

Figure 3.8 compares the spatial perturbation profiles of concentration, velocity, and vorticity for the examined range of k_z in Fig. 3.10 at $t = 1.65$. In all cases, the perturbation profiles are concentrated within the boundary layer region and decay to zero before reaching the lower boundary $z = 1$. While the shape and location of the peak values of $\widehat{c_1}$ are similar among all cases, $\widehat{c_1}$ has the largest variation near $z = 0$ when $k_z = 10$. Consequently, $\widehat{w_1}$ and $\widehat{\Omega}$ are larger in magnitude according to (3.11) and (3.30) for a fixed k_x, indicating an increase in relative strength of vorticity production compared to $k_z = 1$ and 20.

The effect of k_z on the values of vorticity integrals, $\mathcal{I}_1$, $\mathcal{I}_2$ and $\mathcal{I}$, and amplification, Φ_k are tabulated in table 3.1 at $t = 1.65$ when $k_x = 30$, $\gamma = 0$, and $\epsilon = 0.01$. As expected, $k_z = 10$ has the largest values of $\mathcal{I}$. As a result, the corresponding perturbations are more unstable and lead to an earlier onset time of convection. Table 3.1 further shows that $\mathcal{I}_1$ is an order of magnitude larger than $\mathcal{I}_2$ and therefore is

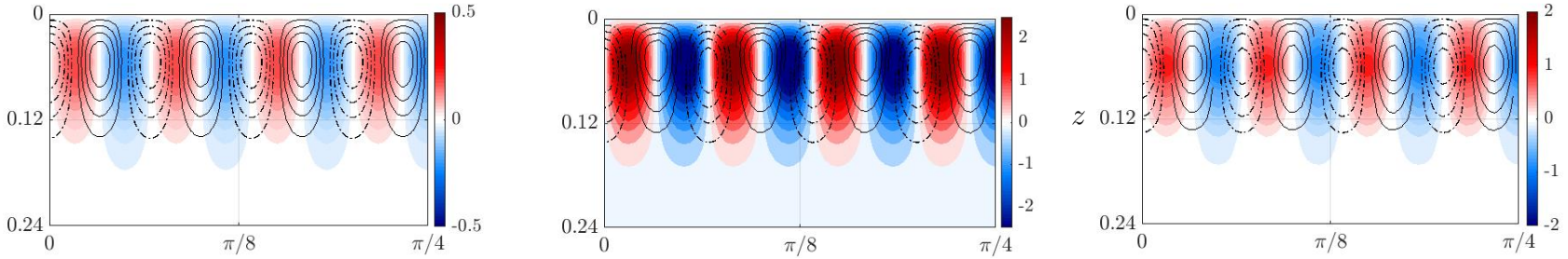

Figure 3.9: Comparison of vorticity contour overlaid with concentration perturbation, $\tilde{c}$, obtained by asymptotic expansion when $k_x = 30$, $\gamma = 0$, and $\epsilon = 0.01$ at $t = 1.65$. (a) $k_z = 1$, (b) $k_z = 10$, and (c) $k_z = 20$. Red and blue indicate positive and negative vorticity pairs. There is a significant shift in the relative strength of vorticity in response to a change in k_z.

k_z	$\mathcal{I}_1$	$\mathcal{I}_2$	$\mathcal{I}$	Φ_k
1	0.014	0.0005	0.014	0.125
10	0.185	0.016	0.191	1.857
20	0.061	0.001	0.061	0.56

Table 3.1: Net vorticity values and amplification obtained by asymptotic expansion when $k_x = 30$, $\gamma = 0$, and $\epsilon = 0.01$ at $t = 1.65$. The values of $\mathcal{I}_3$ and $\mathcal{I}_4$ are negligible for this parameter set and not listed. The values of vorticity integral are correlated with amplification growth.

the primary source of vorticity production $\widehat{\Omega}$.

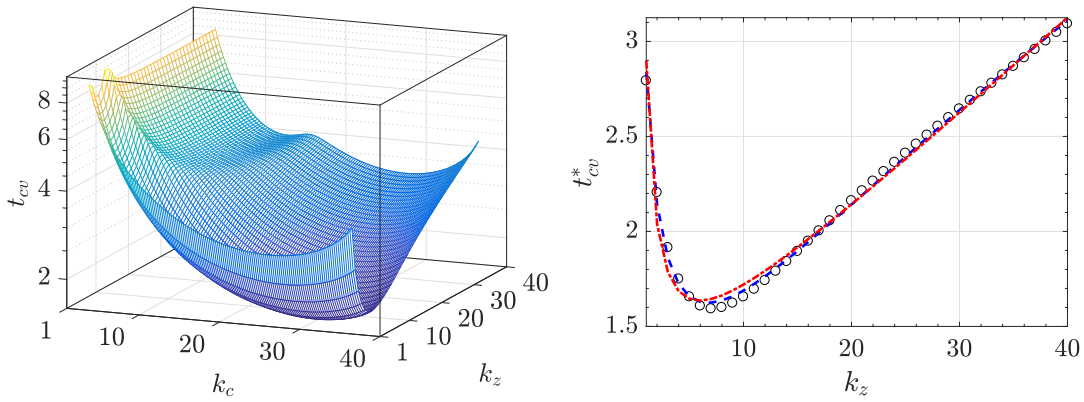

Figure 3.10: Asymptotic expansion results when $\gamma = 0$ and $\epsilon = 0.01$. (a) Onset time of convection, t_{cv}, versus k_x and k_z, (b) t^*_{cv} versus k_z. The dashed line shows relationship (3.32).

To explore the effect of k_z on t_{cv} and t^*_{cv}, we compute the onset time of convection for a wide range of wavenumbers when $\gamma = 0$ and $\epsilon = 0.01$. The variation of t_{cv} as a function of k_x and k_z, as well as the critical onset time of convention vs k_z are plotted in Fig. 3.10(a) and 3.10(b), respectively. As expected, both t_{cv} and t^*_{cv} display a non-monotonic variation as a function of k_z. That is, the onset of time can be either hastened or delayed depending on the porosity structure. For smaller k_z, t^*_{cv} decreases with an increase in k_z where it attains a local minimum and thereafter

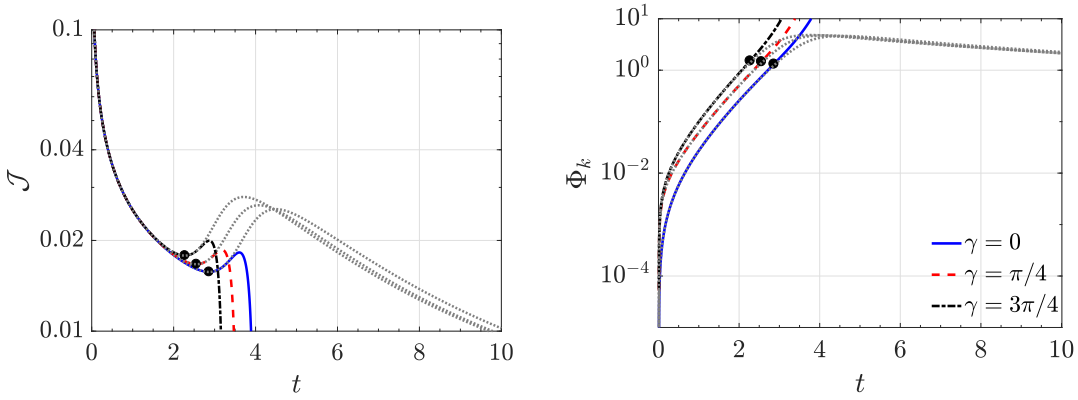

(a) (b)

Figure 3.11: Effect of γ on the time evolutions of (a) flux, (b) the corresponding amplification when $k_x = 30$, $k_z = 1$, and $\epsilon = 0.01$. The dotted lines show the corresponding DNS results. The solid dot marks the onset time of convection, t_{cv}. The threshold of Φ leading to the emergence of convection is attained more quickly when $\gamma = 3\pi/4$.

transitions to a larger value with increasing k_z. This behavior is associated with the magnitude of net vorticity, as shown in Fig. 3.8. We obtain the following fit for t^*_{cv} as a function of k_z using the Levenberg-Marquardt algorithm [69],

$$t^*_{cv} = 0.051k_z + 1.822k_z^{-1} + 1.241 \tag{3.32}$$

The relative error of the nonlinear fit is on the order of 0.1%. We also note that (3.32) is different from (3.27) because the latter corresponds to a single of value of $k_z = 1$, while the former is computed for a widely varying k_z values. Both relationships are obtained for $\gamma = 0$, and $\epsilon = 0.01$.

The effect of porosity phase shift on the temporal evolution of $\mathcal{J}$, computed by asymptotic expansion, is plotted in Fig. 3.11(a) for $k_x = 30$, $k_z = 1$, and $\epsilon = 0.01$. Three different values of the phase shift, $\gamma = 0$, $\pi/4$ and $3\pi/4$, are considered. The

onset time of convection t_{cv} is marked as solid dot in Fig. 3.11(a). t_{cv} occurs more readily when $\gamma = 3\pi/4$ because the amplification required to trigger the convection onset is attained earlier compared to $\gamma = 0$ and $\pi/4$, as show in 3.11(b). This behavior is attributed to a higher perturbation growth which results in a more unstable system and eventually initiates the nonlinear dynamics. Figure 3.11(b) further shows that the slope of Φ_k curve does not change appreciably among various values of γ, although the transition to convection onset requires longer time for $\gamma = 0$ and $\pi/4$, respectively, because they start at a lower energy level.

Figure 3.12 illustrates the spatial profiles of $\widehat{c}_1$, $\widehat{w}_1$, and $\widehat{\Omega}$ when $k_x = 30$, $k_z = 1$, and $\epsilon = 0.01$ at $t = 2.55$. These results are obtained by asymptotic expansion. For all cases, while the perturbation profiles have maximum occurring around same depth z, their corresponding magnitude change appreciably with increasing γ. In the case of $\gamma = 3\pi/4$, the perturbation profiles, $\widehat{c}_1$ and $\widehat{w}_1$, experience a substantial boost compared to $\gamma = 0$. The larger peak value for $\widehat{\Omega}$ indicates an increase in vorticity generation as a result of a comparatively larger magnitude of $\widehat{c}_1$ and, consequently,

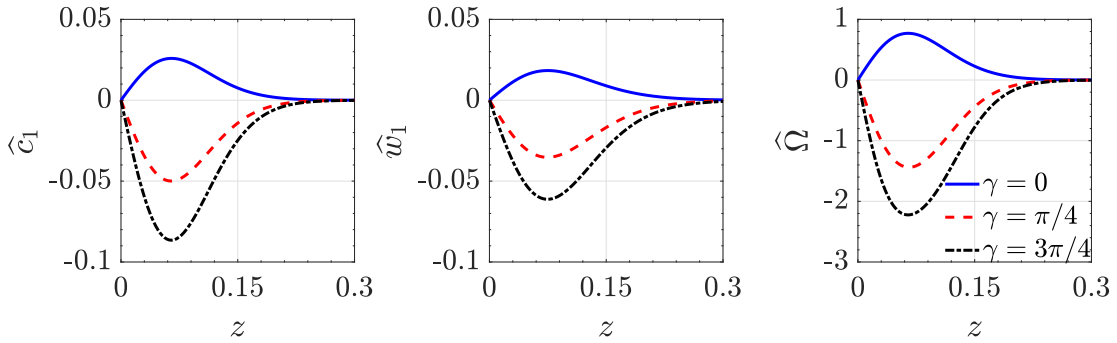

Figure 3.12: Spatial variation of (a) concentration, (b) velocity, and (c) vorticity when $k_x = 30$, $k_z = 1$, and $\epsilon = 0.01$ at $t = 2.55$. In the case of $\gamma = 3\pi/4$, the profiles attain a larger magnitude.

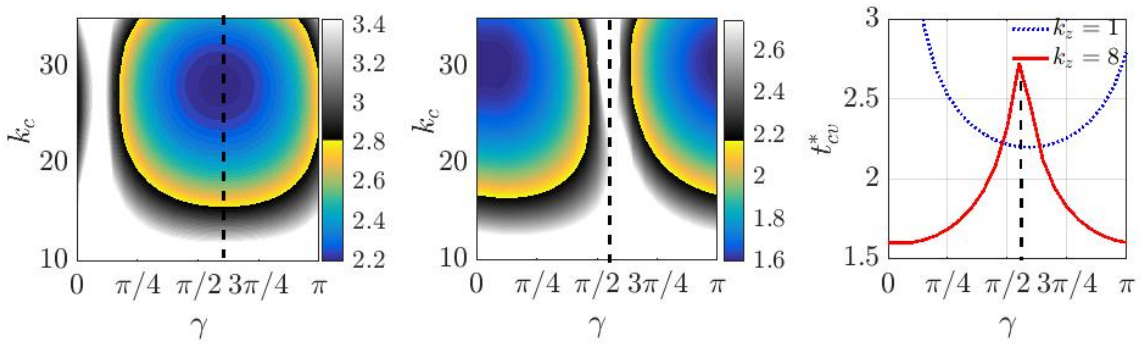

Figure 3.13: Asymptotic expansion results when $\epsilon = 0.01$. (a-b) Onset time convection of in (γ, k_x) plane for $k_z = 1$ and 8, respectively, and (c) Influence of phase shift on the corresponding t^*_{cv}. The vertical dashed line represents the line of symmetry. For $k_z = 1$, the variations of both t_{cv} and t^*_{cv} with respect to γ across the symmetry line is reversed compared to $k_z = 8$.

leads to an increase in total vorticity integral (see table 3.2) when $\gamma = 3\pi/4$. Table 3.2 lists the values of vorticity integrals, $\mathcal{I}_1$, $\mathcal{I}_2$, and $\mathcal{I}$, and the amplification, Φ_k when $k_x = 30$, $\gamma = 0$, $\epsilon = 0.01$, and $t = 2.55$. The values of vorticity integral, as indicated in table 3.2, are correlated with amplification growth. That is, a larger value of $\mathcal{I}$ results in greater perturbation growth for which the convection onset, t_{cv}, occurs sooner. Table 3.2 also shows that $\mathcal{I}_2$ has a comparatively minor effect of the magnitude of net vorticity. A similar event was observed with changing the vertical porosity wavenumber, k_z.

Figure 3.13 (a-b) shows the contour of t_{cv}, obtained by asymptotic expansion,

γ	$\mathcal{I}_1$	$\mathcal{I}_2$	$\mathcal{I}$	Φ_k
0	0.085	0.001	0.086	0.736
$\pi/4$	0.161	0.0125	0.164	1.452
$3\pi/4$	0.262	0.015	0.285	2.711

Table 3.2: Net vorticity values and amplification obtained by asymptotic expansion when $k_x = 30$, $k_z = 1$, and $\epsilon = 0.01$ at $t = 2.55$. The values of $\mathcal{I}_3$ and $\mathcal{I}_4$ are negligible for this parameter set and not listed. The earlier onset of convection results from an increase in the net vorticity.

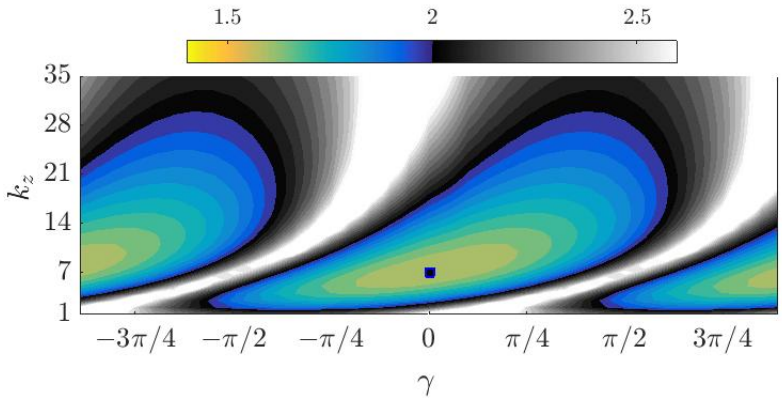

Figure 3.14: Effect of vertical porosity wavenumber and phase shift on the critical time for the onset of convection, t^*_{cv}, based on asymptotic expansion when $\epsilon = 0.01$. Lighter shade indicates transition to lower value of t^*_{cv}, whereas darker shade indicates an increase in t^*_{cv}. The square symbol marks the optimum onset of convection, t^o_{cv}, among the present range of k_z and γ.

in (γ, k_x) plane for two values of vertical wavenumber $k_z = 1$ and 8, respectively, when $\epsilon = 0.01$. For a given k_x, t_{cv} as a function of phase exhibits a nearly symmetric pattern for both values of k_z. While the value of phase shift for which t_{cv} contour becomes symmetric (i.e. line of symmetry) is quantitatively similar for both wavenumbers, the behavior of t_{cv} as a function of phase depends on the value of k_z. For each horizontal wavenumber, t_{cv} develop a local minimum at line of symmetry when $k_z = 1$; that is, t_{cv} increases when γ shifts either to the right or left of the symmetry line. One the other hand, t_{cv} shows an opposite trend when $k_z = 8$, for which it reaches a local maxima at the symmetry line. Similar behavior is observed for the critical onset times of convection, as illustrated in Fig. 3.13 (c). Furthermore, the value of t^*_{cv} is significantly smaller when $k_z = 8$ as a result of a larger perturbation growth, as discussed earlier.

Figure 3.14 shows the influence of the vertical porosity structure on t^*_{cv} ob-

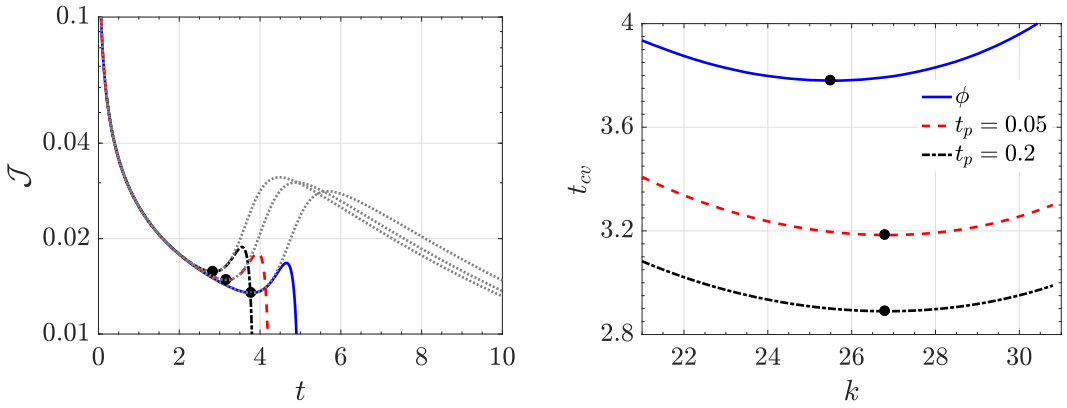

Figure 3.15: Comparison of a continuously perturbed porous system results with an impulsively perturbed system when $\epsilon = 10^{-4}$. Two different value of t_p are considered for impulsively initiated system. (a) Time evolution of dissolution flux for $k_x = 26$. The dotted lines show the corresponding DNS results and the solid dot marks the onset time of convection, t_{cv}. (b) t_{cv} vs k. The solid dot denotes the optimum condition, (t^o_{cv}, k^o) for which the earliest t_{cv}, is reached for the present ϵ value. The onset time of convection is sensitive to the choice of perturbations types.

tained by asymptotic expansion in the plane of k_z and γ. As expected, t^*_{cv} is sensitive to vertical porosity wavenumber and phase shift. Figure 3.14 shows that the local minima of t^*_{cv} occur at intermediate values of k_z where t^*_{cv} increases with a further increase and/or decrease in k_z. The time shift in the critical time for the onset of convection coincides with a shift in its perturbation energy during which it reaches a larger value. Furthermore, the corresponding phase value at the points of minima increases with increasing k_z. The optimum onset of convection, t^o_{cv}, marked with a square symbol in Fig. 3.14, denotes the earliest onset time of convection across the examined range of k_z and γ which corresponds to $(k^o_z, \gamma^o) = (6.95, 0)$.

In the following, we examine whether the two types of perturbation, namely, porosity-based and concentration-based, used to trigger the instability have an influence on the dynamics of convective mixing and dissolution rate. In the latter case,

which represents an impulsively perturbed system, the boundary layer is perturbed at initial time $t = t_p$ according to,

$$c_p(z, t = t_p) = \epsilon\, \xi cos(k_c x) \mathrm{e}^{-\xi^2}, \qquad \xi = z\sqrt{Ra/(4\, t_p)} \tag{3.33}$$

where ϵ and k_c are the initial perturbation magnitude and perturbation wavenumber, respectively. Because of the transient nature of the diffusive boundary layer, the stability characteristic and the subsequent convective transport is sensitive to initial perturbation time, t_p.

Figure 3.15 compares the temporal evolution of dissolution flux, as well as the onset time of convection as a function of perturbation wavenumber for a continuously perturbed system with those of an impulsively initiated perturbed system. These results are obtained by asymptotic expansion. In the case of an impulsively perturbed system, two different values of $t_p = 0.05$ and 0.2 are considered. For a given k_x, as discussed above, the convection onset of a continuously perturbed system depends on the vertical porosity structure. To facilitate the comparison of t_{cv} with traditional perturbation type, we therefore choose the lowest t_{cv} among all values of k_z and γ as the corresponding onset time of convection for k_x. The perturbation type, as shown in Fig. 3.15(a) which plots the time evolution of flux when $k_x = 26$ and $\epsilon = 10^{-4}$, has a noticeable effect on the dissolution rate as well as on the onset of convection. The onset time of convection shifts to a later time in an impulsively perturbed system compared to the other approach. This behavior questions the physical relevance of the predicted convective mixing results in an im-

pulsively perturbed system and it is thus unclear whether the corresponding values represent a realistic estimation of various stage of mixing regimes. Figure 3.15(a) further shows that t_p has a rather dramatic effect on t_{cv} for this type of perturbed system. In particular, t_{cv} is attained more quickly when $t_p = 0.2$, which corresponds to the optimal initial perturbation time for the parameter set considered in Fig. 3.15. On the other hand, a continuously perturbed system is not sensitive to t_p. This highlights another benefit of this class of perturbations in which the counter intuitive notion of an optimal t_p is not of relevance in determining the characteristics of convective mixing.

Figure 3.15(b) compares the variation of t_{cv} as function of k, where k refers to the horizontal perturbation wavenumber in both systems. Similarly, the effect of perturbation type on t_{cv} is found to be significant. The solid dot in Fig. 3.15(b) denotes the optimum condition, (t^o_{cv}, k^o) for which the earliest onset time of convection occurs at k^o when $\epsilon = 10^{-4}$. As expected, while there is a significant difference in t^o_{cv} results between the two perturbed systems, a difference of less extent is also observed for k^o. Overall, while the qualitative features of convection onset obtained by two different perturbation types remain the same, figure 3.15(b) confirms the inherent uncertainty in prediction of various dissolution flux regimes as the result of different perturbation types. More specifically, the results of concentration-based perturbation fail to predict the corresponding values of continuously perturbed system, which is a more physically realistic representation of a porous system.

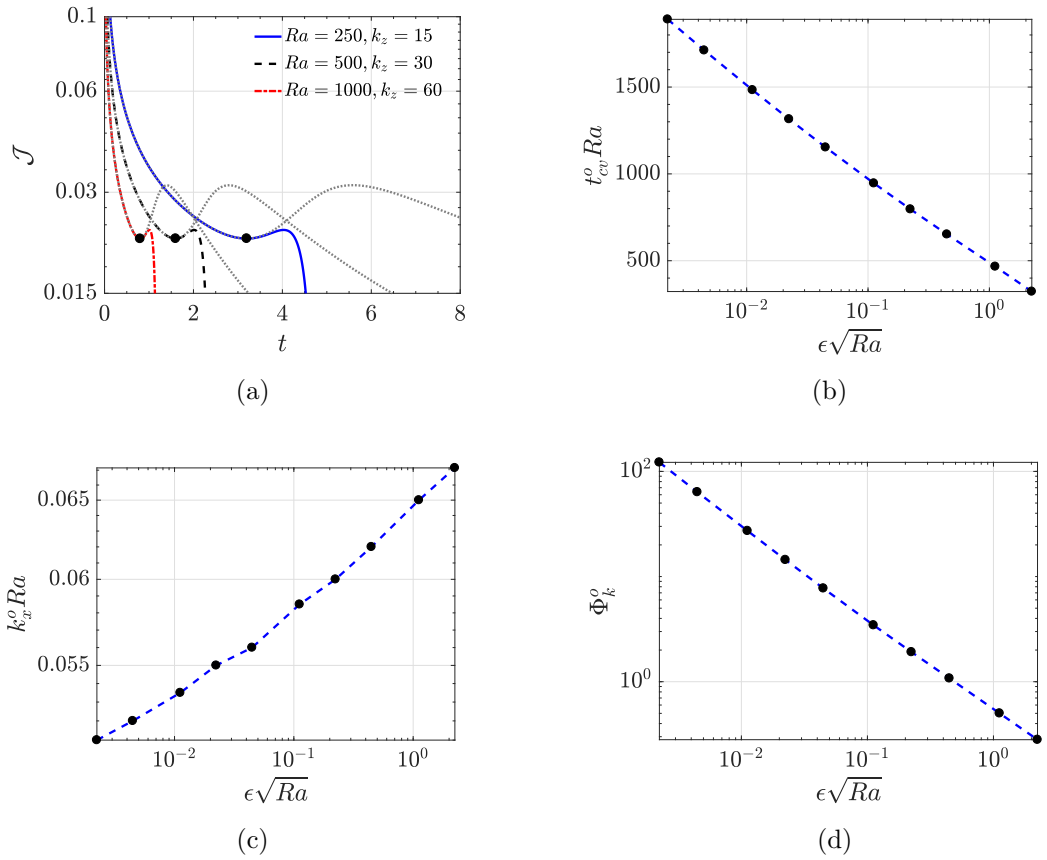

Figure 3.16: Time evolution of dissolution flux for three pairs of Ra and k_z when $\epsilon = 0.01$. The dotted lines represent the corresponding DNS results and solid symbols mark t_{cv}, (b-d) The variation of t^o_{cv}, k^o_x, and Φ^o_k as a function of $\epsilon\sqrt{Ra}$, respectively. The dashed line shows relationships (3.34).

3.3.3 Influence of of Rayleigh number and scaling

In order to characterize the development of convective mixing in a system perturbed continuously by a single disturbance period, it is important to obtain scaling relations that accurately predicts the relevant time scales and the dissolution pattern. In the following, we compute the optimal onset time of convection t^o_{cv} and corresponding wavenumber k^o_x for $250 \leq Ra \leq 1000$ and $10^{-6} \leq \epsilon \leq 0.1$. Figure 3.16 compares the time evolution of dissolution flux for three combinations of $Ra = 250$

and $k_z = 15$, $Ra = 500$ and $k_z = 30$, and $Ra = 1000$ and $k_z = 60$ when $\epsilon = 0.01$. Higher Ra results in a quicker emergence of convection onset t_{cv}. For the current range of Ra, the effect of the domain height, shown in Fig. 3.1, on the convective fingers is negligible at the convection onset. As a result, the Rayleigh number dependence of the problem can be eliminated by a simple rescaling according to $H^* = \bar{\phi}\mathcal{D}/U$ and time $T^* = \bar{\phi}H^*/U$, and the results collapse to a single curve as shown in the inside plot in Fig. 3.16(a). The following scaling relationship are obtained from Fig. 3.16 (b–d),

$$t_{cv}^o Ra = -520.725 \log_{10}(\epsilon\sqrt{Ra}) + 474.552 \tag{3.34a}$$

$$k_x^o Ra = -0.0642(\epsilon\sqrt{Ra})^{-0.804} \tag{3.34b}$$

$$\Phi_k^o = -0.533(\epsilon\sqrt{Ra})^{-0.878} \tag{3.34c}$$

Additionally, the corresponding Sherwood number, a non-dimensional measure of relative effect of convective to diffusive flux, at the optimum onset of convection takes the form of $Sh^o = 12.899(\epsilon\sqrt{Ra})^{0.1122}$.

To illustrate the relevant length and time scales of convection onset in physical systems, relations (3.34a)–(3.34b) can be rewritten in dimensional form as,

$${t_{cv}^*}^o = \frac{\bar{\phi}^2\mathcal{D}}{U^2}\left\{-520.725 \log_{10}(\epsilon\sqrt{Ra}) + 474.552\right\} \tag{3.35a}$$

$$k_x^{*o} = \frac{U}{\bar{\phi}\mathcal{D}}\left\{-0.0642(\epsilon\sqrt{Ra})^{-0.804}\right\} \tag{3.35b}$$

where ${t_{cv}^*}^o$ and k_x^{*o} are the dimensional optimal onset time of convection and hor-

izontal wavenumber, respectively. We use the following parameter values for CO_2 sequestration, reported by Ennis-King & Peterson [26], to estimate the optimal onset time of convection and wavelength of convective plume: $\mu = 5\times10^{-4}$ Pa s, $\mathcal{D} = 10^{-9}$ m^2s^{-1}, $\Delta\rho = 10$ kg m^{-3}, $\phi = 0.2$, $10^{-14} \leq K \leq 10^{-12}$ m^2, and $g = 9.81$ m s^{-2}. Using these parameters for a high-permeability aquifer, $K = 10^{-12}$ m^2, the optimal onset time and wavelength vary between ${t^*_{cv}}^o = 16$ days and $\lambda_x^{*o} = 12.1$ cm when $\epsilon^* = 10^{-2}$, and in the case of $\epsilon^* = 10^{-4}$ the scaling relations gives ${t^*_{cv}}^o = 42$ days and $\lambda_x^{*o} = 14.16$ cm. For a low permeability aquifer, $K = 10^{-14}$ m^2, these parameters vary between ${t^*_{cv}}^o = 335$ years, $\lambda_x^{*o} = 12.1$ m, for $\epsilon^* = 10^{-3}$, and ${t^*_{cv}}^{o*} = 965$ years, $\lambda_x^{*o} = 14.4$ m when $\epsilon^* = 10^{-4}$. Note that in these calculation, $\mathcal{D}$ is taken to be the molecular diffusivity of CO_2, however, in realistic geological settings the convection process can also take place by dispersion as a result of various correlation length scales associated with permeability.

3.4 Conclusions

In this work, we studied a canonical 2D homogeneous system where perturbations arise due to spatial variation of porosity in the porous system using three complementary methodologies. The advantage of this approach is not only the elimination of the required initial shape function and optimal initial perturbation time (a necessary condition for concentration-based method), but it also serves as a more realistic method in which the growth of perturbation is immediate. Using a reduced nonlinear method, we first examined the effect of harmonic variations of porosity

in the transverse and streamwise direction on the onset time of convection and late time behavior. It was found that the choice of perturbation method has a noticeable effect on the onset of convection and the subsequent nonlinear regime, in that the onset time of convection is reached more quickly in an impulsively perturbed system. Scaling relationships for the optimal onset of convection and wavenumber were also developed in terms of aquifer properties and initial perturbation magnitude.

Bibliography

[1] Ague, J. J. Models of permeability contrasts in subduction zone mélange: Implications for gradients in fluid fluxes, Syros and Tinos Islands, Greece. *Chemical Geology 239*, 3 (2007), 217–227.

[2] Bachu, S. Sequestration of CO_2 in geological media: criteria and approach for site selection in response to climate change. *Energy Conversion and Management 41* (2000), 953–970.

[3] Bachu, S. Screening and ranking of sedimentary basins for sequestration of CO_2 in geological media in response to climate change. *Environmental Geology 44*, 3 (2003), 277–289.

[4] Bachu, S. CO_2 storage in geological media: role, means, status and barriers to deployment. *Progress in Energy and Combustion Science 34*, 2 (2008), 254–273.

[5] Backhaus, S., Turitsyn, K., and Ecke, R., E. Convective instability and mass transport of diffusion layers in a Hele-Shaw geometry. *Physical Review Fluids 106* (2011), 104501.

[6] Bando, S., Takemura, F., Nishio, M., Hihara, E., and Akai, M. Viscosity of aqueous NaCl solutions with dissolved CO_2 at (30 to 60)°C and (10 to 20) MPa. *Journal of Chemical & Engineering Data 49*, 5 (2004), 1328–1332.

[7] Barrash, W., and Clemo, T. Hierarchical geostatistics and multifacies systems: Boise hydrogeophysical research site, Boise, Idaho. *Water Resources Research 38*, 10 (2002).

[8] Bear, J. *Dynamics of Fluids in Porous Media*. Dover Publications, 1988.

[9] Ben, Y., Demekhin, E. A., and Chang, H. C. A spectral theory for small-amplitude miscible fingering. *Physics of Fluids 14* (2002), 999–1010.

[10] Benson, S. M., and Cole, D. R. CO_2 sequestration in deep sedimentary formations. *Elements 4*, 5 (2008), 325–331.

[11] Blair, L. M., and Quinn, J. A. The onset of convection in a fluid layer with time-dependent density gradients. *Journal of Fluid Mechanics 36* (1969), 385–400.

[12] Bridge, G., Bouzarovski, S., Bradshaw, M., and Eyre, N. Geographies of energy transition: Space, place and the low-carbon economy. *Energy Policy 53* (2013), 331–340.

[13] Caltagirone, J. P. Stability of a saturated porous layer subject to a sudden rise in surface temperature: Comparison between linear and energy methods. *Quarterly Journal of Mechanics and Applied Mathematics 33* (1980), 47–58.

[14] Chen, C. Y., and Meiburg, E. Miscible porous media displacements in the quarter five-spot configuration. Part 1. The homogeneous case. *Journal of Fluid Mechanics 371* (1998), 233–268.

[15] Cheng, P., Bestehorn, M., and Firoozabadi, A. Effect of permeability anisotropy on buoyancy-driven flow for CO_2 sequestration in saline aquifers. *Water Resources Research 48*, 9 (2012). W09539.

[16] Daniel, D., Riaz, A., and Tchelepi, H. A. Onset of natural convection in layered aquifers. *Journal of Fluid Mechanics* (3 2015), 763–781.

[17] Daniel, D., Tilton, N., and Riaz, A. Optimal perturbations of gravitationally unstable, transient boundary layers in porous media. *Journal of Fluid Mechanics 727* (2013), 456–487.

[18] De Wit, A., and Homsy, G. M. Viscous fingering in periodically heterogeneous porous media. Part I. Formulation and linear instability. *Journal of Chemical Physics 107* (1997), 9609–9618.

[19] De Wit, A., and Homsy, G. M. Viscous fingering in periodically heterogeneous porous media. Part II. Numerical simulations. *Journal of Chemical Physics 107* (1997), 9619–9628.

[20] Delgado, J. M. P. Q. Longitudinal and transverse dispersion in porous media. *Chemical Engineering Research and Design 85*, 9 (2007), 1245–1252.

[21] Doumenc, F., Boeck, T., Guerrier, B., and Rossi, M. Transient Rayleigh–Bénard–Marangoni convection due to evaporation: a linear non-normal stability analysis. *Journal of Fluid Mechanics 648* (2010), 521–539.

[22] Drazin, P., and Reid, W. *Hydrodynamic Stability*. Cambridge University Press, 2004.

[23] Elenius, M. T., and Johannsen, K. On the time scales of nonlinear instability in miscible displacement porous media flow. *Computational Geosciences* (2012), 1–11.

[24] Emami-Meybodi, H., Hassanzadeh, H., Green, C. P., and Ennis-King, J. P. Convective dissolution of CO_2 in saline aquifers: Progress in modeling and experiments. *International Journal of Greenhouse Gas Control 40* (2015), 238–266.

[25] Ennis-King, J., and Paterson, L. Role of convective mixing in the long-term storage of carbon dioxide in deep saline formations. *SPE 84344* (2003), 1–12.

[26] Ennis-King, J. P., and Paterson, L. Role of convective mixing in the long-term storage of carbon dioxide in deep saline formations. *SPE Journal 10* (2005), 349–356.

[27] Ennis-King, J. P., Preston, I., and Paterson, L. Onset of convection in anisotropic porous media subject to a rapid change in boundary conditions. *Physics of Fluids 17* (2005), 84–107.

[28] Farajzadeh, R., Ranganathan, P., Zitha, P. L. J., and Bruining, J. The effect of heterogeneity on the character of density-driven natural convection of CO_2 overlying a brine layer. *Advances in Water Resources 34* (2011), 327–339.

[29] Farrell, B. F., and Ioannou, P. J. Generalized stability theory. Part I: Autonomous operators. *Journal of the Atmospheric Sciences 53*, 14 (1996), 2025–2040.

[30] Farrell, B. F., and Ioannou, P. J. Generalized stability theory. Part II: Nonautonomous operators. *Journal of the Atmospheric Sciences 53*, 14 (1996), 2041–2053.

[31] Fleury, M., and Deschamps, H. Electrical conductivity and viscosity of aqueous nacl solutions with dissolved CO_2. *Journal of Chemical & Engineering Data 53*, 11 (2008), 2505–2509.

[32] Fossen, H. *Structural Geology*. Cambridge University Press, 2016.

[33] Foster, T. D. Stability of a homogeneous fluid cooled uniformly from above. *Physics of Fluids 8* (1965), 1249–1257.

[34] Fu, X., Cueto-Felgueroso, L., and Juanes, R. Pattern formation and coarsening dynamics in three-dimensional convective mixing in porous media. *Philosophical Transactions of the Royal Society A 371*, 2004 (2013), 20120355.

[35] Garcia, J. E. Density of aqueous solutions of CO_2. *Lawrence Berkeley National Laboratory* (2001).

[36] Gaus, I. Role and impact of CO_2–rock interactions during CO_2 storage in sedimentary rocks. *International Journal of Greenhouse Gas Control 4*, 1 (2010), 73–89.

[37] Gelhar, L. W. Stochastic subsurface hydrology from theory to applications. *Water Resources Research 22*, 9S (1986).

[38] Gelhar, L. W., Welty, C., and Rehfeldt, K. R. A critical review of data on field-scale dispersion in aquifers. *Water Resources Research 28*, 7 (1992), 1955–1974.

[39] Ghorbani, Z., Riaz, A., and Daniel, D. Convective mixing in vertically-layered porous media: The linear regime and the onset of convection. *Physics of Fluids 29*, 8 (2017), 084101.

[40] Goldstein, A. W. Stability of a horizontal fluid layer with unsteady heating from below and time-dependent body force. Tech. Rep. R-4, NASA Tech. Rep., 1959.

[41] Gounot, J., and Caltagirone, J. P. Stabilité et convection naturelle au sein d'une couche poreuse non homogène. *International Journal of Heat and Mass Transfer 32* (1989), 1131–1140.

[42] Gresho, P. M., and Sani, R. L. The stability of a fluid layer subjected to a step change in temperature: Transient vs. frozen time analyses. *International Journal of Heat and Mass Transfer 14* (1971), 207–221.

[43] Hassanzadeh, H., Pooladi-Darvish, M., and Keith, D. W. Stability of a fluid in a horizontal saturated porous layer: Effect of non-linear concentration profile, initial, and boundary conditions. *Transport in Porous Media 65* (2006), 193–211.

[44] Hassanzadeh, H., Pooladi-Darvish, M., and Keith, D. W. Scaling behavior of convective mixing, with application to geological storage of CO_2. *AIChE Journal 53*, 5 (2007), 1121–1131.

[45] Hewitt, D. R., Neufeld, J. A., and Lister, J. R. Convective shutdown in a porous medium at high Rayleigh number. *Journal of Fluid Mechanics 719* (2013), 551–586.

[46] Hewitt, D. R., Neufeld, J. A., and Lister, J. R. High Rayleigh number convection in a three-dimensional porous medium. *Journal of Fluid Mechanics 748* (2014), 879–895.

[47] Hidalgo, J. J., and Carrera, J. Effect of dispersion on the onset of convection during CO_2 sequestration. *Journal of Fluid Mechanics 640*, 2009 (2009), 441.

[48] Hilgers, C., and Urai, J. L. Microstructural observations on natural syntectonic fibrous veins: implications for the growth process. *Tectonophysics 352*, 3 (2002), 257–274.

[49] Horton, C., and Rogers Jr, F. Convection currents in a porous medium. *Journal of Applied Physics 16*, 6 (1945), 367–370.

[50] Horváth, D., Tóth, S., and Tóth, Á. Periodic heterogeneity-driven resonance amplification in density fingering. *Physical Review Letters 97* (2006), 194501.

[51] Hu, B. X., Meerschaert, M. M., Barrash, W., Hyndman, D. W., He, C., Li, X., and Guo, L. Examining the influence of heterogeneous porosity fields on conservative solute transport. *Journal of Contaminant Hydrology 108*, 3 (2009), 77–88.

[52] Huppert, H. E., and Neufeld, J. a. The Fluid Mechanics of Carbon Dioxide Sequestration. *Annual Review of Fluid Mechanics 46*, 1 (2014), 255–272.

[53] Jhaveri, B. S., and Homsy, G. M. The onset of convection in fluid layers heated rapidly in a time-dependent manner. *Journal of Fluid Mechanics 114* (1982), 251–260.

[54] Kaviany, M. Onset of thermal convection in a saturated porous medium: experiment and analysis. *International Journal of Heat and Mass Transfer 27* (1984), 2101–2110.

[55] Kim, M. C., and Choi, C. K. The stability of miscible displacement in porous media: Nonmonotonic viscosity profiles. *Physics of Fluids 23* (2011), 084105.

[56] Kneafsey, T. J., and Pruess, K. Laboratory experiments and numerical simulation studies of convectively enhanced carbon dioxide dissolution. *Energy Procedia 4* (2011), 5114–5121.

[57] Lackner, K. S. A guide to CO_2 sequestration. *Science 300*, 5626 (2003), 1677–1678.

[58] Lal, R. Carbon sequestration. *Philosophical Transactions of the Royal Society of London B: Biological Sciences 363*, 1492 (2008), 815–830.

[59] Lapwood, E. Convection of a fluid in a porous medium. In *Mathematical proceedings of the cambridge philosophical society* (1948), vol. 44, Cambridge Univ Press, pp. 508–521.

[60] Lele, S. K. Compact finite differences with spectral-like resolution. *Journal of Computational Physics 103* (1992), 16.

[61] Lick, W. The instability of a fluid layer with time-dependent heating. *Journal of Fluid Mechanics 21* (1965), 565–576.

[62] Lindeberg, E., and Bergmo, P. The long-term fate of CO_2 injected into an aquifer. In *Greenhous Gas Control Technologies*, vol. 1. Elsevier, 2003, pp. 489–495.

[63] MacMinn, C., Szulczewski, M., and Juanes, R. CO_2 migration in saline aquifers. Part 2. capillary and solubility trapping. *Journal of Fluid Mechanics 688* (2011), 321–351.

[64] Manickam, O., and Homsy, G. Fingering instabilities in vertical miscible displacement flows in porous media. *Journal of Fluid Mechanics 288* (1995), 75–102.

[65] McKibbin, R. Heat transfer in a vertically-layered porous medium heated from below. *Transport in Porous Media 1* (1986), 361–370.

[66] McKibbin, R., and O'Sullivan, M. J. Onset of convection in a layered porous medium heated from below. *Journal of Fluid Mechanics 96* (1980), 375–393.

[67] Metz, B., Davidson, O., De Coninck, H., Loos, M., and Meyer, L. IPCC special report on carbon dioxide capture and storage. Tech. rep., Intergovernmental Panel on Climate Change, Geneva (Switzerland). Working Group III, 2005.

[68] Meybodi, H. E., and Hassanzadeh, H. Mixing induced by buoyancy-driven flows in porous media. *AIChE Journal 59*, 4 (2013), 1378–1389.

[69] Moré, J. J. The levenberg-marquardt algorithm: implementation and theory. In *Numerical analysis*. Springer, 1978, pp. 105–116.

[70] Neufeld, J. A., Hesse, M., A., Riaz, A., Hallworth, M., A., Tchelepi, H. A., and Huppert, H. E. Convective dissolution of carbon dioxide in saline aquifers. *Geophysical Research Letters 37* (2010), L22404.

[71] Nield, D. A. Convective heat transfer in porous media with columnar structure. *Transport in Porous Media 2* (1987), 177–185.

[72] Nield, D. A., and Bejan, A. *Convection in porous media*. Springer Science & Business Media, 2006.

[73] Nield, D. A., and Kuznetsov, A. V. The effect of combined vertical and horizontal heterogeneity on the onset of convection in a bidisperse porous medium. *International Journal of Heat and Mass Transfer 50* (2007), 3329–3339.

[74] Orr, F. M. CO_2 capture and storage: are we ready? *Energy & Environmental Science 2*, 5 (2009), 449–458.

[75] Orr, F. M. Onshore geologic storage of CO_2. *Science 325* (2009), 1656–1658.

[76] Pau, G. S. H., Bell, J. B., Pruess, K., Almgren, A. S., Lijewski, M. J., and Zhang, K. High-resolution simulation and characterization of density-driven flow in CO_2 storage in saline aquifers. *Advances in Water Resources 33* (2010), 443–455.

[77] Peyret, R. *Spectral Methods for Incompressible Viscous Flows*. Springer-Verlag, New York, 2002.

[78] Phillips, O. M. *Geological fluid dynamics: Sub-surface flow and reactions*. Cambridge University Press, 2009.

[79] Prasad, A., and Simmons, C. T. Unstable density-driven flow in heterogeneous porous media: A stochastic study of the Elder [1967b] "short heater" problem. *Water Resources Research 39* (2003), 4–21.

[80] Ranganathan, P., Farajzadeh, R., Bruining, H., and Zitha, P. L. J. Numerical simulation of natural convection in heterogeneous porous media for CO_2 geological storage. *Transport in Porous Media 95* (2012), 25–54.

[81] Rapaka, S., Chen, S., Pawar, R. J., Stauffer, P. H., and Zhang, D. Non-modal growth of perturbations in density-driven convection in porous media. *Journal of Fluid Mechanics 609* (2008), 285–303.

[82] Rapaka, S., Pawar, R. J., Stauffer, P. H., Zhang, D., and Chen, S. Onset of convection over a transient base-state in anisotropic and layered porous media. *Journal of Fluid Mechanics 641* (2009), 227–244.

[83] Rees, D. A. S., Selim, A., and Ennis-King, J. P. The instability of unsteady boundary layers in porous media. In *Emerging Topics in Heat and Mass Transfer in Porous Media*. Springer, 2008, pp. 85–110.

[84] Rees, D. A. S., and Tyvand, P. A. Onset of convection in a porous layer with continuous periodic horizontal stratification. Part I. Two-dimensional convection. *Transport in Porous Media 77* (2009), 187–205.

[85] Riaz, A., and Cinar, Y. Carbon dioxide sequestration in saline formations: Part IReview of the modeling of solubility trapping. *Journal of Petroleum Science and Engineering 124* (2014), 367–380.

[86] Riaz, A., Hesse, M., Tchelepi, A., and Orr, F. M. Onset of convection in a gravitationally unstable diffusive boundary layer in porous media. *Journal of Fluid Mechanics 548* (2006), 87–111.

[87] Riaz, A., and Tchelepi, H. A. Linear stability analysis of immiscible two-phase flow in porous media with capillary dispersion and density variation. *Physics Of Fluids 16*, 12 (2004), 4727–4737.

[88] Robinson, J. L. Theoretical analysis of convective instability of a growing horizontal thermal boundary layer. *Physics of Fluids 19* (1976), 778–791.

[89] Ruith, M., and Meiburg, E. Miscible rectilinear displacements with gravity override. Part 1. homogeneous porous medium. *Journal of Fluid Mechanics 420* (2000), 225–257.

[90] Schincariol, R. A., Schwartz, F. W., and Mendoza, C. A. Instabilities in variable density flows: Stability and sensitivity analyses for homogeneous and heterogeneous media. *Water Resources Research 33* (1997), 31–41.

[91] Schmid, P. J. Nonmodal stability theory. *Annual Review of Fluid Mechanics 39* (2007), 129–162.

[92] Schmid, P. J., and Henningson, D. S. *Stability and Transition in Shear Flows*. Springer, 2001.

[93] Selim, A., and Rees, D. The stability of a developing thermal front in a porous medium. I Linear theory. *Journal of Porous Media 10* (2007), 1–15.

[94] Simmons, C. T., Fenstemaker, T. R., and Sharp, J. M. Variable-density groundwater flow and solute transport in heterogeneous porous media: Approaches, resolutions and future challenges. *Journal of Contaminant Hydrology 52* (2001), 245–275.

[95] Slim, A., and Ramakrishnan, T. Onset and cessation of time-dependent, dissolution-driven convection in porous media. *Physics of Fluids 22* (2010), 124103.

[96] Slim, A. C., Bandi, M. M., Miller, J. C., and Mahadevan, L. Dissolution-driven convection in a Hele-Shaw cell. *Physics of Fluids 25* (2013), 024101.

[97] Spycher, N., and Pruess, K. A phase-partitioning model for CO_2–brine mixtures at elevated temperatures and pressures: Application to CO_2-enhanced geothermal systems. *Transport in Porous Media 82* (2010), 173–196.

[98] Szulczewski, M., Hesse, M., and Juanes, R. Carbon dioxide dissolution in structural and stratigraphic traps. *Journal of Fluid Mechanics 736* (2013), 287–315.

[99] Tan, C., and Homsy, G. Simulation of nonlinear viscous fingering in miscible displacement. *Physics of Fluids 31* (1988), 1330–1338.

[100] Tan, C. T., and Homsy, G. M. Viscous fingering with permeability heterogeneity. *Physics of Fluids 4* (1992), 1099–1101.

[101] Tarek, A. *Reservoir engineering handbook*. Gulf Professional Publishing, 2006.

[102] Tchelepi, H. A., and Orr, F. M. Interaction of viscous fingering, permeability heterogeneity, and gravity segregation in 3 dimensions. *SPE Reservoir Engineering 9* (1994), 266–271.

[103] Theofilis, V. Global Linear Instability. *Annual Review of Fluid Mechanics 43*, 1 (2011), 319–352.

[104] Thomas, D. C., and Benson, S. M. *Carbon Dioxide Capture for Storage in Deep Geologic Formations-Results from the CO_2 Capture Project: Vol 1-Capture and Separation of Carbon Dioxide from Combustion, Vol 2-Geologic Storage of Carbon Dioxide with Monitoring and Verification*. Elsevier, 2005.

[105] Tiab, D., and Donaldson, E. C. *Petrophysics: theory and practice of measuring reservoir rock and fluid transport properties*. Gulf professional publishing, 2015.

[106] Tilton, N., Daniel, D., and Riaz, A. The initial transient period of gravitationally unstable diffusive boundary layers developing in porous media. *Physics of Fluids 25* (2013), 092107.

[107] Tilton, N., and Riaz, A. Nonlinear stability of gravitationally unstable, transient, diffusive boundary layers in porous media. *Journal of Fluid Mechanics 745* (4 2014), 251–278.

[108] Vreme, A., Nadal, F., Pouligny, B., Jeandet, P., Liger-Belair, G., and Meunier, P. Gravitational instability due to the dissolution of carbon dioxide in a Hele-Shaw cell. *Physical Review Fluids 1*, 6 (2016), 064301.

[109] Ward, T., Jensen, O., Power, H., and Riley, D. High-rayleigh-number convection of a reactive solute in a porous medium. *Journal of Fluid Mechanics 760* (2014), 95–126.

[110] Weir, G. J., White, S. P., and Kissling, W. M. Reservoir storage and containment of greenhouse gases. *Transport in Porous Media 23*, 1 (1996), 37–60.

[111] Wessel-Berg, D. On a linear stability problem related to underground CO_2 storage. *SIAM Journal on Applied Mathematics 70*, 4 (2009), 1219–1238.

[112] Xu, X., Chen, S., and Zhang, D. Convective stability analysis of the long-term storage of carbon dioxide in deep saline aquifers. *Advances in Water Resources 29* (2006), 397–407.